

COMPARISON OF CONE MODEL AND MEASURED DYNAMIC IMPEDANCE  
FUNCTIONS OF SHALLOW FOUNDATIONS

By

PATRICK WILLIAM DUNN

A DISSERTATION PRESENTED TO THE GRADUATE SCHOOL  
OF THE UNIVERSITY OF FLORIDA IN PARTIAL FULFILLMENT  
OF THE REQUIREMENTS FOR THE DEGREE OF  
DOCTOR OF PHILOSOPHY

UNIVERSITY OF FLORIDA

2010

© 2010 Patrick William Dunn

To Mom and Dad, thank you for your love, support, and inspiration.

## ACKNOWLEDGMENTS

I thank my advisor for his guidance and patience during my studies over the years. I would like to thank my committee for their assistance with this project. Financial backing from the U. S. National Science Foundation is greatly appreciated. I thank my parents who have always been supportive throughout my life. Appreciation is due to my uncle and aunt for their continued encouragement. My friends and the rest of my family are also due a great deal of gratitude as well for their moral support.

# TABLE OF CONTENTS

	<u>page</u>
ACKNOWLEDGMENTS .....	4
LIST OF TABLES .....	7
LIST OF FIGURES .....	8
ABSTRACT .....	14
CHAPTER	
1 INTRODUCTION .....	15
1.1 Problem Statement.....	15
1.2 Hypothesis .....	17
1.3 Objectives .....	17
1.4 Scope.....	17
1.5 Organization of Dissertation.....	18
2 FOUNDATION IMPEDANCE FUNCTIONS .....	20
2.1 Definition.....	20
2.2 Computation .....	22
2.3 Measurement.....	26
3 CONE MODEL PREDICTIONS .....	40
3.1 Wolf and Deeks (2004).....	40
3.2 Wong and Luco (1978).....	42
3.3 Mita and Luco (1989).....	44
3.4 Wong and Luco (1985).....	45
3.5 Apsel and Luco (1987) .....	48
3.6 Nii (1987).....	48
3.7 Crouse, et al. (1990).....	51
4 SITE CHARACTERIZATION .....	99
4.1 Site Investigation .....	99
4.1.1 Traditional Investigation .....	99
4.1.2 Seismic Investigation.....	100
4.2 Foundation Selection and Construction.....	101
4.3 Shakers.....	103

5	MEASURED IMPEDANCE FUNCTIONS.....	110
5.1	Footing 5.....	110
5.1.1	Vertical Loading.....	110
5.1.2	Horizontal Loading.....	111
5.2	Footing 6.....	115
5.2.1	Vertical loading.....	115
5.2.2	Horizontal Loading.....	117
6	IMPEDANCE FUNCTION COMPARISON AND ASSESSMENT .....	158
6.1	Cone Model Development.....	158
6.1.1	Soil Profile.....	158
6.1.2	CONAN Model .....	159
6.2	Cone Model and Measured Impedance Function Comparison.....	163
6.2.1	Footing 5.....	163
6.2.2	Footing 6.....	166
6.3	Assessment .....	170
6.3.1	Measurement Error.....	170
6.3.2	Prediction Parameters.....	171
6.3.3	Model Assumptions.....	172
7	CLOSURE .....	189
7.1	Summary of Findings .....	189
7.2	Conclusions.....	190
7.3	Recommendations.....	191
	LIST OF REFERENCES.....	192
	BIOGRAPHICAL SKETCH .....	195

## LIST OF TABLES

<u>Table</u>		<u>page</u>
3-1	Parameters for Eight Wong and Luco (1985) Comparisons.....	54
3-2	Soil Profile for Apsel and Luco (1987) Model.....	55
3-3	Model Footings of Nii (1987).....	56
6-1	Free Field Soil Properties for Footing 5 and Footing 6. ....	174
6-2	CONAN Input File for Footing 5 Vertical Model. ....	175
6-3	CONAN Input File for Footing 6 Horizontal and Rotational Model.....	176

## LIST OF FIGURES

<u>Figure</u>	<u>page</u>
2-1 Foundation / Soil Diagram.....	35
2-2 Foundation Free Body Diagram.....	36
2-3 Cone Diagrams.....	37
2-4 Reflected and Refracted Wave Diagram.....	38
2-5 Embedded Stacked Disks.....	39
3-1 Vertical Impedance Functions for Model 1 .....	57
3-2 Horizontal Impedance Functions for Model 1 .....	58
3-3 Rocking Impedance Functions for Model 1.....	59
3-4 Torsion Impedance Functions for Model 1.....	60
3-5 Vertical Impedance Functions for Model 4 Length/Width=4.....	61
3-6 Torsion Impedance Functions for Model 4 Length/Width=4.....	62
3-7 Horizontal Impedance Functions in Long Direction for Model 4 Length/Width=4.....	63
3-8 Rocking Impedance Functions About Short Axis. for Model 4 Length/Width=4.....	64
3-9 Horizontal Impedance Functions in Short Direction for Model 4 Length/Width=4 .....	65
3-10 Rocking Impedance Functions About Long Axis for Model 4: Length/Width=4.....	66
3-11 Vertical Impedance Functions for Model 3 Embedded .....	67
3-12 Horizontal Impedance Functions for Model 3 Embedded.....	68
3-13 Rocking Impedance Functions for Model 3 Embedded .....	69
3-14 Torsional Impedance Functions for Model 3 Embedded.....	70
3-15 Coupled Impedance Functions for Model 3 Embedded .....	71
3-16 Vertical Impedance Functions for Model 1: Basis Model .....	72
3-17 Horizontal Impedance Functions for Model 1: Basis Model.....	73
3-18 Rocking Impedance Functions for Model 1: Basis Model .....	74

3-19	Torsional Impedance Functions for Model 1: Basis Model.....	75
3-20	Vertical Impedance Functions for Model 4: ¼ Layer Thickness.....	76
3-21	Horizontal Impedance Functions for Model 4: ¼ Layer Thickness .....	77
3-22	Rocking Impedance Functions for Model 4: ¼ Layer Thickness.....	78
3-23	Torsional Impedance Functions for Model 4: ¼ Layer Thickness .....	79
3-24	Vertical Impedance Functions for Model 6: Higher Vs Contrast.....	80
3-25	Horizontal Impedance Functions for Model 6: Higher Vs Contrast.....	81
3-26	Rocking Impedance Functions for Model 6: Higher Vs Contrast .....	82
3-27	Torsional Impedance Functions for Model 6: Higher Vs Contrast.....	83
3-28	Vertical Impedance Functions for Model 8: Poisson’s Ratio=0.45.....	84
3-29	Horizontal Impedance Functions for Model 8: Poisson’s Ratio=0.45.....	85
3-30	Rocking Impedance Functions for Model 8: Poisson’s Ratio=0.45 .....	86
3-31	Torsional Impedance Functions for Model 8: Poisson’s Ratio=0.45 .....	87
3-32	Horizontal Impedance Functions for Layered Model.....	88
3-33	Rocking Impedance Functions for Layered Model. ....	89
3-34	Coupled Impedance Functions for Layered Model .....	90
3-35	Vertical Impedance Functions for Circular.....	91
3-36	Vertical Impedance Functions for Circular.....	92
3-37	Vertical Impedance Functions for Rectangular .....	93
3-38	Vertical Impedance Functions for Rectangular .....	94
3-39	Vertical Impedance Functions for Surface, L/W=2 Model Footing.....	95
3-40	Vertical Impedance Functions for Station 6 .....	96
3-41	Horizontal Impedance Functions for Station 6 .....	97
3-42	Rocking Impedance Functions for Station 6.....	98
4-1	Seismic, SPT, and profile.....	105

4-2	Footing 5 .....	106
4-3	Footing 6 .....	107
4-4	Reinforcement of Footing 6 .....	107
4-5	ANCO Model MK-12 .....	108
4-6	NSF NEES “Thumper” mobile shaker .....	108
4-7	NSF NEES “T-Rex” mobile shaker .....	109
5-1	Vertical Experiment for Footing 5 with ANCO shaker .....	121
5-2	ANCO vertical results for Footing 5 .....	121
5-3	ANCO vertical results for Footing 5 .....	122
5-4	Horizontal Experiment for Footing 5 with Model 400 Electro-Seis shaker .....	123
5-5	Electro-Seis horizontal loading results for Footing 5 at elevation 1 ft .....	124
5-6	Electro-Seis horizontal loading results for Footing 5 at elevation 2 ft .....	125
5-7	Electro-Seis horizontal loading results for Footing 5 at elevation 3 ft .....	126
5-8	Electro-Seis horizontal loading results for Footing 5 at elevation 4 ft .....	127
5-9	Electro-Seis horizontal loading results for the one-degree-of-freedom analyses of Footing 5 at elevation 1 ft .....	128
5-10	Electro-Seis horizontal loading results for the one-degree-of-freedom analyses of Footing 5 at elevation 2 ft .....	129
5-11	Electro-Seis horizontal loading results for the one-degree-of-freedom analyses of Footing 5 at elevation 3 ft .....	130
5-12	Electro-Seis horizontal loading results for the one-degree-of-freedom analyses of Footing 5 at elevation 4 ft .....	131
5-13	Electro-Seis horizontal loading results for the non-equal coupling two-degree-of-freedom analyses of Footing 5 at elevations 1 ft and 2 ft .....	132
5-14	Electro-Seis horizontal loading results for the non-equal coupling two-degree-of-freedom analyses of Footing 5 at elevations 1 ft and 3 ft .....	133
5-15	Electro-Seis horizontal loading results for the non-equal coupling two-degree-of-freedom analyses of Footing 5 at elevations 1 ft and 4 ft .....	134

5-16	Electro-Seis horizontal loading results for the non-equal coupling two-degree-of-freedom analyses of Footing 5 at elevations 2 ft and 3 ft .....	135
5-17	Electro-Seis horizontal loading results for the non-equal coupling two-degree-of-freedom analyses of Footing 5 at elevations 2 ft and 4 ft .....	136
5-18	Electro-Seis horizontal loading results for the non-equal coupling two-degree-of-freedom analyses of Footing 5 at elevations 3 ft and 4 ft .....	137
5-19	Electro-Seis horizontal loading results for the equal coupling two-degree-of-freedom analyses of Footing 5 at elevations 1 ft and 2 ft .....	138
5-20	Electro-Seis horizontal loading results for the equal coupling two-degree-of-freedom analyses of Footing 5 at elevations 1 ft and 3 ft .....	139
5-21	Electro-Seis horizontal loading results for the equal coupling two-degree-of-freedom analyses of Footing 5 at elevations 1 ft and 4 ft .....	140
5-22	Electro-Seis horizontal loading results for the equal coupling two-degree-of-freedom analyses of Footing 5 at elevations 2 ft and 3 ft .....	141
5-23	Electro-Seis horizontal loading results for the equal coupling two-degree-of-freedom analyses of Footing 5 at elevations 2 ft and 4 ft .....	142
5-24	Electro-Seis horizontal loading results for the equal coupling two-degree-of-freedom analyses of Footing 5 at elevations 3 ft and 4 ft .....	143
5-25	Electro-Seis horizontal loading results for the one-degree-of-freedom at 4 ft, independent coupling two-degree-of-freedom at 2 ft and 4 ft, the equal coupling two-degree-of-freedom analyses of Footing 5 at elevations 2 ft and 4 ft .....	144
5-26	Vertical Experiment with Thumper shaker .....	145
5-27	Vertical Experiment with Thumper shaker .....	145
5-28	Thumper vertical results for Footing 6 .....	146
5-29	Thumper vertical results for Footing 6 .....	146
5-30	Vertical Experiment with T-Rex shaker .....	147
5-31	Vertical Experiment with T-Rex shaker .....	147
5-32	T-Rex vertical results for Footing 6 .....	148
5-33	T-Rex vertical results for Footing 6 .....	148
5-34	Horizontal Experiment for Footing 6 with Model MK-12 ANCO shaker mounted flush .....	149

5-35	Horizontal Experiment for Footing 6 with Model MK-12 ANCO shaker on stand. ....	150
5-36	ANCO horizontal loading results for Footing 6 flush mounting.....	151
5-37	ANCO horizontal loading results for Footing 6 elevated mounting.....	152
5-38	ANCO horizontal loading results for the one-degree-of-freedom analyses of Footing 6 flush mounting.....	153
5-39	ANCO horizontal loading results for the one-degree-of-freedom analyses of Footing 6 elevated mounting.....	154
5-40	ANCO horizontal loading results for the non-equal coupling two-degree-of-freedom analyses of Footing 6 .....	155
5-41	ANCO horizontal loading results for the equal coupling two-degree-of-freedom analyses of Footing 6 .....	156
5-42	ANCO horizontal loading results for one-degree-of-freedom at flushed and elevated positions, independent coupling two-degree-of-freedom, and equal coupling two-degree-of-freedom analyses of Footing 6 .....	157
6-1	ANCO vertical comparison for Footing 5 .....	177
6-2	Electro-Seis horizontal comparison for the one-degree-of-freedom at 4 ft, independent coupling two-degree-of-freedom at 2 ft and 4 ft, the equal coupling two-degree-of-freedom analyses of Footing 5 at elevations 2 ft and 4 ft .....	178
6-3	Electro-Seis horizontal comparison for the one-degree-of-freedom at 4 ft, independent coupling two-degree-of-freedom at 2 ft and 4 ft, the equal coupling two-degree-of-freedom analyses of Footing 5 at elevations 2 ft and 4 ft .....	179
6-4	Electro-Seis horizontal comparison for the one-degree-of-freedom at 4 ft, independent coupling two-degree-of-freedom at 2 ft and 4 ft, the equal coupling two-degree-of-freedom analyses of Footing 5 at elevations 2 ft and 4 ft .....	180
6-5	Thumper and T-Rex vertical comparison for Footing 6 .....	181
6-6	ANCO horizontal comparison for the one-degree-of-freedom flush mount, independent coupling two-degree-of-freedom, the equal coupling two-degree-of-freedom analyses of Footing 6.....	182
6-7	ANCO horizontal comparison for the one-degree-of-freedom flush mount, independent coupling two-degree-of-freedom, the equal coupling two-degree-of-freedom analyses of Footing 6.....	183

6-8	ANCO horizontal comparison for the one-degree-of-freedom flush mount, independent coupling two-degree-of-freedom, the equal coupling two-degree-of-freedom analyses of Footing 6.....	184
6-9	Footing 5 Vertical and 1-DoF Error Band.....	185
6-10	Footing 5 2-DoF Error Band.....	186
6-11	Footing 6 Vertical and 1-DoF Error Band.....	187
6-12	Footing 6 2-DoF Error Band.....	188

Abstract of Dissertation Presented to the Graduate School  
of the University of Florida in Partial Fulfillment of the  
Requirements for the Degree of Doctor of Philosophy

COMPARISON OF CONE MODEL AND MEASURED DYNAMIC IMPEDANCE  
FUNCTIONS OF SHALLOW FOUNDATIONS

By

Patrick William Dunn

May 2010

Chair: Dennis R. Hiltunen  
Major: Civil Engineering

Developments in seismic testing methods and increased electronic recording capabilities have reached a level that allows computation and verification of dynamic impedance function predictions for shallow foundations. Prior to these developments very little data was available for verification of impedance functions thus field design capabilities with respect to dynamic foundation response remains impractical. This study draws a positive relationship between cone models and multiple impedance function prediction techniques. Cone models are then utilized to compare to the limited data available from previous field studies. Next, field data from an experiment designed for impedance function measurement is discussed. For the experiment two square and embedded shallow foundations have been dynamically loaded at the National Geotechnical Experiment Site (NGES) on the campus of Texas A&M University (TAMU) via four dynamic loading devices implemented in several configurations. The dynamic load and vibration responses of the foundations were measured via appropriate electronic instrumentation. Utilizing appropriate equations of motion and system parameters, and the measured load and vibration responses, dynamic impedance functions were backcalculated for the vertical, horizontal sliding, and rocking modes of vibration. Cone model predictions were compared to the backcalculated impedance functions with promising results.

## CHAPTER 1 INTRODUCTION

### **1.1 Problem Statement**

Recent decades of research have produced significant advancements in both laboratory and in situ characterization of geotechnical sites, and in methodologies for the prediction of dynamic foundation behavior. Improvements have yet to be fully realized even though these methods are the starting points for virtually all calculations of dynamic foundation response, from sensitive instrument bases to earthquake shaking analyses. Multiple numerical models for predicting dynamic foundation responses based upon elastodynamic theories are now available which seem to exhibit agreement with each other. Coupled with greatly enhanced geophysical testing capabilities which yield excellent soil characterization, dynamic footing response predictions may offer the available accuracy for response predictions and possibly foundation design.

For example, the cone models presented by Wolf and Deeks (2004) recommend a strength of materials approach for predicting shallow foundation responses to dynamic loading. The method, documented by Wolf and Deeks, is similar to bar and beam theories commonly applied in structural engineering and is based on one dimensional truncated cone modeling techniques. Cone modeling assumes excitation of a foundation creates wave propagation in the form of a vertical cone that increases in radius with respect to depth. From this assumption, fundamental principles of wave propagation are accounted for and a single solution is produced. Though some accuracy is sacrificed with cone models when compared to three dimensional elastodynamic methods, this loss is offset by reductions in theoretical complexity which leads to ease of use. The simplified cone solutions can be applied to a wide range of site conditions and foundation configurations making them more practical for dynamic foundation design.

Foundation excitation and soil-structure interaction can be estimated for a wide range of layer configurations, frequencies, embedment depths and scales using cone modeling.

There are, however, shortcomings in the field of dynamic footing responses. The most critical being there are no substantial test results based on full size models or typical design shapes applied in practice and found in field construction. It is impossible to determine whether these theories and methods are applicable to actual construction and design situations without realistic, controlled results being analyzed.

Though the few available studies appear to indicate agreement between theory and observed results, the available research is extremely limited in scope for various reasons. For example, some small scale laboratory based tests were reported by Nii (1985). However, these foundations were only a few centimeters in size, and tests were run with model foundations on a model half space constructed of various atypical materials (e.g. acrylic resin and silicone rubber). In addition to material concerns, the model half space had finite dimensions which may alter foundation response.

Fry (1963) conducted realistic full-scale tests but these studies lack adequate geophysical surveys to characterize the soil conditions. In these experiments seismic properties of the site are sparse and the accuracy of the data could be questioned. More thorough geophysical testing with present testing techniques would ensure more accuracy in any model. That accuracy would most likely carry over to foundation response predictions. The same improved capabilities applied to measuring time data used for geotechnical surveys can be applied to observing the excitation experienced by a foundation. Thus the accuracy of measurements during testing is increased making any study potentially more effective. Both the model and any full scale experiments benefit from the refined technology reducing reliance on previous, less accurate studies.

Foundations of realistic scales, properties, embedment depths and shapes need to be constructed and tested to confirm current theories of dynamic foundation response. Performing tests under well characterized and controlled conditions could confirm theories and methodologies that, until now, are assumed to be accurate and useful.

## **1.2 Hypothesis**

Strength of materials based cone models can be used to accurately predict the response of an in situ shallow foundation excited by a dynamic load.

## **1.3 Objectives**

The primary objective of this research is to assess the ability of the simplified strength of materials based cone models for predicting shallow footing responses to dynamic loading accurately. Specific objectives of this research include the following:

- Determine reliable techniques for dynamically loading in situ shallow foundations of typical scales, embedments and shapes in vertical and coupled horizontal-rocking modes.
- Determine reliable techniques for measuring foundation responses during excitation and back compute the dynamic impedance functions of the corresponding measurements.
- Predict dynamic responses of measured in situ shallow foundation excitation using cone modeling with comprehensive geotechnical characterization of the site and footing specifications.
- Conduct detailed comparison of cone model predictions versus measured shallow foundation responses via dynamic impedance functions.

## **1.4 Scope**

Two shallow foundations were dynamically loaded at the National Geotechnical Experiment Site (NGES) on the Texas A&M University (TAMU) Riverside Campus in Bryan Texas. The primary advantages and subsequent reasoning for testing this site begin with previous geotechnical investigations already completed. Data from these tests saved a great deal of time as well as funding and provided valuable information which was not only used in the

study but also allowed for greater effectiveness during the experimental design stage. More importantly the completed investigation contained seismic data from crosshole testing and surface wave analysis. The seismic data gave an especially valuable insight into the site during experimental design. Another advantage was found in footings that were already constructed. While some were destroyed during prior testing, at least one was still capable of being tested in the required manner.

Footings tested were loaded dynamically by at least two different shakers. Each shaker had advantages that were exploited to produce reliable displacements in multiple directions and modes. Prior to shaking, footings were instrumented in order to monitor their displacements.

Data pertaining to both the force of the shakers and motion of the footing were collected simultaneously. Collected data was then processed to yield impedance function values and compared to predicted values. Measurement techniques were also noted during experimentation and studied for effectiveness.

### **1.5 Organization of Dissertation**

An overview of the following chapters follows. Chapter two provides the methodology behind dynamic foundation modeling and a discussion of steps taken to measure foundation response and calculate impedance function values from those responses. Coinciding with and supporting the discussion of technique and measurement is the literature review.

Chapter three presents the physical characteristics of the site and any foundations subjected to testing. Among the information of interest discussed are traditional soil testing, seismic testing, foundation physical characteristics, and foundation selection and construction.

Chapter four demonstrates the relationship between cone modeling and other impedance function prediction methods. With this relationship established, the cone model is selected to represent predicted impedance function values in a comparison against measured values. These

comparisons further support the relationship between predicted and measured values, thus leading to the conclusion that the tests performed at the NGES site are pertinent to the study of cone modeling with respect to prediction of dynamic impedance functions.

## CHAPTER 2 FOUNDATION IMPEDANCE FUNCTIONS

### 2.1 Definition

Dynamic foundation displacement predictions typically focus on impedance functions, also referred to as impedances. These impedances are used to create a model of the soil by representing the soil on or in which the foundation rests as an equivalent system of springs and dampers. Impedances are determined for each type of movement in all directions. For example, to predict the reaction of a foundation excited in the vertical mode, a spring and damping coefficient are calculated which represent the resistance produced by the soil in the vertical direction. Similar calculations can produce impedance values in all three primary directions. Impedances can also be calculated that describe the rotational soil reaction on the foundation about all three axis as well.

The response of a footing with respect to dynamic loading can be modeled starting with a soil, foundation system. A foundation rests on or is embedded in a soil half-space or multi layered soil system as illustrated in the diagram of Figure 2-1. The foundation is excited and results in a displacement. An incomplete list of factors that determine impedances include soil properties such as stiffness and layer thickness as well as foundation parameters such as size, shape and rigidity. Perhaps the most important factor accounted for during foundation response investigation is the frequency of the load. Impedance values can vary substantially with regards to the frequency of the excitation force and thus need to be measured or calculated for any frequency of interest.

To predict the foundation's response to an excitation force, a free body diagram such as the one in Figure 2-2 is developed containing typical necessary information regarding the foundation. Dynamic loads are depicted as forces acting at appropriate locations on the footing.

The soil is accounted for by assuming that any pressure between the footing and the soil can be represented by a reaction force acting at a particular point on the footing. That point's location is dictated by the pressure distribution of the soil on the foundation. For example an upward vertical force through the footing centroid is assumed to represent pressure on the bottom of the footing during downward vertical dynamic loading on the top of the center of the footing. Once the free body diagram is complete, dynamic equilibrium can be expressed using Newton's second law (Equation 2-1), as demonstrated in the Gazetas (1991).

$$P_z(t) + m\ddot{u}_z(t) = F_z(t) \quad (2-1)$$

In the case of vertical excitation through the center of gravity there are two forces. The components  $F_z(t)$  and  $P_z(t)$  represent the dynamic load and soil pressure force respectively with the  $z$  subscript indicating the vertical direction. The acceleration of the mass in the vertical direction is accounted for in the equation by the component  $m\ddot{u}_z(t)$ .

While the dynamic load and the acceleration of mass are fairly simple to comprehend and qualify, the soil force requires further investigation. The interaction between the foundation and soil is estimated to have a linear relationship to small strain foundation displacement presented in Equation 2-2.

$$P_z(t) = K_z \cdot u_z(t) \quad (2-2)$$

The variable,  $K_z$ , is typically known as the dynamic vertical impedance and is expressed in units of force per length. Substitution of equation two into equation one allows for solution of the differential equation for the dynamic displacement, provided that an adequate quantification of  $K_z$  is available. Dynamic impedance is a complex number, and further analysis allows  $K_z$  to be represented by a spring and dashpot model leading to Equation 2-3 where  $\overline{\mathbf{K}}_z$  is the dynamic stiffness. Dynamic stiffness accounts for both the soil's stiffness as well as inertia properties.

Material and geometric damping are accounted for by  $C_z$  known as the dashpot coefficient. It also turns out that for soil-foundation systems, the dynamic stiffness and dashpot coefficients are dependent on the excitation force frequency.

$$K_z = \overline{K}_z + i\omega C_z \quad (2-3)$$

Multiple notation conventions are instituted when studying dynamic impedance functions and often depend on the author. The convention presented to this point is that of the Gazetas (1991) text. Another example of notation for discussing cone modeling is presented in Wolf and Deeks (2004). They present dynamic impedance in a complex form and using dimensionless coefficients in Equation 2-4 where  $S(a_0)$  is the frequency dependent dynamic impedance,  $k(a_0)$  is dimensionless dynamic stiffness, and  $c(a_0)$  is the dimensionless damping coefficient. The term  $a_0$  is dimensionless frequency and can be calculated using Equation 2-5 where  $r_0$  is a length of the foundation and  $c_{s1}$  is the shear wave velocity of the first layer of soil. The  $K$  in equation 4 is a coefficient that assigns a dimension of force per length to the dynamic impedance and is typically some value depending on foundation system characteristics such as width or the underlying soil shear modulus. It is typically referred to as the static stiffness.

$$S(a_0) = K[k(a_0) + i a_0 c(a_0)] \quad (2-4)$$

$$a_0 = \frac{\omega r_0}{c_{s1}} \quad (2-5)$$

## 2.2 Computation

Methods for determining impedance functions vary in approach and scope of effectiveness. For example certain methods may be appropriate for calculating impedance functions when dealing with a surface footing on a half space, while other methods would be necessary to produce impedances for a layered embedded system. To develop an understanding of cone

models, techniques are most conveniently organized into analytical and numeric solutions assuming elastodynamic soil behavior and approximate solutions which determine impedances based on simplified models.

Initial impedance function methods focused on analytical solutions. Multiple response prediction approaches have been developed beginning in the thirties when Reissner (1990) proposed predictions for a simple circular surface footing on a linearly elastic isotropic half space. Advances continued with research covering the effects of damping (Bycroft [1990]) and finite layer depths. Dynamic finite element methods dealing with embedment in layered systems were first developed for strip and circular footings, and required a shallow rigid layer as a boundary (Waas (1972); Kausel (1974); Luco (1976) Lysmer et al. (1975). This was followed by more analytical and semi-analytical multi-layered solutions which included rectangular footing shapes, but were unable to account for embedment (Luco [1976]; Gazetas and Roesset [1976, 1979]). Next, analytical and numerical methods were combined in an effort to exploit the strengths of both (Kausel [1981]; Lysmer [1981]; Tassoulas [1981]). Today, better finite element and boundary element methods are available for 3D solutions of embedded footings in layered soil deposits. Though generally effective, the analytical and numerical methods require considerable unique preparation to each set of conditions to generate solutions. Hence a great deal of time and funding may be consumed in order to apply the above theories to an individual project (Gazetas [1991]).

Approximate solutions provide relief from the detailed input and execution of analytical and numerical methods and also provide clarity of the problem that rigorous methods do not allow (Roesset [Foreword]). However, some aspects can not be accounted for with approximate methods, such as soil separation from the foundation, and thus are ideal for simplification by an

approximate solution. Though accuracy is sacrificed, in many cases this may be acceptable if the use of simpler models saves time as well as other resources and still provides a reliable safe result (Gazetas [1991]). The approximate methods include the half-space analogs of Richart, Hall, and Woods (1970), the work of Novak and his colleagues that appears in the computer programs PILAY, PILAY2, and DYNA5, the table and chart solutions of Gazetas (1991), and the cone models described by Wolf and Deeks (2004). Cone models are likely the most advanced of the approximate methods for application in engineering practice. Wolf and Deeks (2004) provide a detailed description of the implementation of cone models to foundation vibration problems. A summary of the methodology is provided in the following paragraphs.

To analyze the vibrations of a foundation on the surface of or embedded in a layered half-space with cone models, an approach using conical bars and beams, called cones, is developed. The complicated exact formulation of three-dimensional elastodynamics is replaced by the simple one-dimensional description of the theory of the strength of materials, postulating the deformation behavior ('plane sections remain plane').

The half-space with linear elastic behavior and hysteretic material damping can consist of any number of horizontal layers either overlying a half-space or fixed at its base. Besides cylindrical foundations, axi-symmetric configurations of arbitrary embedment shape can be processed, with the wall and base of the embedded foundation assumed to be rigid. The dynamic-stiffness coefficients describing the interaction force-displacement relationship and the effective foundation input motion for vertically propagating S- and P-waves in seismic excitation are calculated for all frequencies.

Only approximations of the one-dimensional strength-of-materials approach based on wave propagation in cones apply. No other assumptions are made. For each degree of freedom

only one type of body wave exists: for the horizontal and torsional motions S-waves propagating with the shear-wave velocity; and for the vertical and rocking motions P-waves propagating with the dilatational-wave velocity.

Two building blocks are required to construct the procedure to analyze the vibrations of a foundation in a layered half-space. The first addresses the outward wave propagation occurring from a disk embedded in a full-space modeled as a double cone. 2- 3 illustrates the sectional property of these initial cones increases in the direction of wave propagation, modeling the spreading of the disturbance in the medium.

The cones are thus radiating. The opening angle of the cone is determined by equating the static-stiffness coefficient of the truncated semi-infinite cone to that of a disk on a half-space determined using the three-dimensional theory of elasticity. The opening angle depends only on Poisson's ratio (and the degree of freedom). In the case of nearly- incompressible and compressible material (Poisson's ratio larger than 1/3), the wave velocity is limited to twice the shear-wave velocity and a trapped mass and mass moment of inertia are introduced for the vertical and rocking degrees of freedom, respectively.

The second building block addresses the wave mechanism generated at a material discontinuity corresponding to an interface between two layers. When the incident wave propagating in the initial cone (described in the first building block) encounters a discontinuity, a reflected wave and a refracted wave, each propagating in its own cone, are created. The cone diagram presented in Figure 2-4 illustrates both reflected and refracted waves.

Enforcement of compatibility of displacement and equilibrium of the interface permits the reflected and refracted waves to be expressed as a function of the incident wave. The reflection coefficient, defined as the ratio of the reflected wave to the incident wave, depends on the

frequency and on the properties of the two materials present at the interface, in particular their impedances.

The reflected and refracted waves generated at an interface will also encounter material discontinuities as incident waves at a later stage, yielding additional reflections and refractions. By tracking the reflections and refractions sequentially, the superimposed wave pattern can be established for a layered site up to a certain stage. The termination criterion addresses the number of cone segments in which the waves have propagated and the magnitude of the created waves.

The embedded foundation is modeled with a stack of disks in that part of the soil which will be excavated as illustrated in Figure 2-5. This leads to a primary dynamic system with redundants acting on the embedded disks. As in the force method of structural analysis, the dynamic flexibility of the free field with respect to the displacements of the disks caused by the redundants is established addressing the wave pattern in the layered half-space. Inversion of this relationship, enforcement of the rigid-body motion of the foundation (considering the free-field motion of the seismic waves, if present) and excavation of the trapped material yield the dynamic-stiffness coefficients of the embedded foundation and the effective foundation input motion.

Wolf and Deeks (2004) provide a complete MATLAB implementation of the method, together with a comprehensive description of the workings of each function. These can be used along with the built-in facilities of MATLAB, such as the fast Fourier transformation, to perform all necessary analyses in the MATLAB environment.

### **2.3 Measurement**

There are a very small number of studies documented in the literature in which dynamic impedance functions for shallow foundations have been determined in situ at sites in which the

soil conditions and properties are well characterized. These studies include Crouse, et al. (1990); De Barros and Luco (1995); Luco, Trifunac, and Wong (1988); Luco and Wong (1990); and Wong, Trifunac, and Luco (1988).

Crouse, et al. (1990) report experimental impedance functions for two small concrete foundations supported by soil and in real field conditions. Both foundations were utilized to support earthquake accelerograph stations. One foundation (Cholame 1E) was located in central California, and consisted of a 10-cm (4-in.) thick, 1.27-m (50-in.) square slab resting on corner piers and embedded in a moderately stiff alluvial deposit. The other foundation (Station 6) was a 15-cm (6-in.) thick, 1.22-m x 1.14-m (48-in. x 45-in.) nearly square slab, embedded 7.6 cm (3 in.) in a softer deposit in southern California. Shear wave velocity profiles were determined for each site via in situ SASW tests, and reported in detail by Crouse, et al. (1990). The soils at both sites were assumed by Crouse, et al. to have a unit weight of  $17,300 \text{ N/m}^3$  ( $110 \text{ lb/ft}^3$ ), a Poisson's ratio of  $1/3$ , and a material damping ratio of 0.015.

To determine impedance functions, forced harmonic vibration tests were performed on the foundations. Harmonic forces were induced with a small (156 N, 35 lb) eccentric-mass vibration shaker bolted to the foundation surface. The measured response was determined via triaxial accelerometers mounted at each corner of the foundation. The impedance functions were then determined from the induced force and measured response via appropriate equations of motion for the dynamic system. The impedance functions are presented for the vertical, horizontal, and rocking modes of vibration and for frequencies from 10 to 60 Hz.

De Barros and Luco (1995) describe testing a one quarter scale model of a nuclear containment facility constructed in Hualin, Taiwan. Detailed procedures and appropriate equations of motion for impedance function determination are provided then, predicted and

measured impedances from the test are compared. The model was cylindrical and had a height of 16.13 m with a base of diameter 10.82 m. The base was 3.00 m thick and rested on a layer of concrete 0.15 m thick. The mass of the base and thin layer of concrete was 695,000 kg. The containment shell was reinforced concrete of wall thickness 0.30 m, outer diameter of 10.52 m, and a height of 11.63 m. The estimated mass of the shell was 264,000-kg. The roof was a cylindrical slab of diameter 13.28 m with thickness of 1.50 m and a mass of 505,000-kg. In the center was a 2.20 by 2.20 m hole. Four beams with dimensions 0.60 m by 0.30 m supported the roof. The thin slab underneath the base rested on soil 5.15 m below grade. The surrounding soil was banked with the toe 1.50-m from the base. DeBarros and Luco (1995) provide a table of soil properties relevant to the study of impedance functions. Crosshole testing provided shear wave velocities for the site. The soil directly below the base is reported as having a unit weight of  $23,740 \text{ N/m}^3$ , Poisson's ratio of 0.47, and a damping ratio of 0.02.

Horizontal dynamic loading was performed by an eccentric mass shaker on the model's base and top in both the North-South direction and the East-West direction. The horizontal force frequency varied from 2 to 20 Hz and the shaker force exerted relied on the frequency. Vertical dynamic loads were imparted on the base with frequencies ranging from 2 to 25 Hz. A discussion of foundation response recording methods was not available.

DeBarros and Luco (1995) present methodology for calculating impedance functions from measured data. Calculations of appropriate forces and displacements for determining impedances are introduced. Impedances determined from measured responses were then normalized to represent a test conducted with a dynamic force of 9806 N at all frequencies. The measured impedances were compared to those submitted by volunteers who made predictions based on reported soil characteristics of the site and design aspects of the containment model.

Luco, Trifunac, and Wong (1988) demonstrate that it is possible to separate the effects of a structure during dynamic loading from the response of a foundation during dynamic testing thereby being able to produce impedance functions from measure responses. The Millikan Library Building on the California Institute of Technology campus was loaded dynamically and the responses of the structure and the foundation were monitored. The library is a nine-story reinforced concrete building at a height of 43.9 m above grade with a basement slab 4.3 m below grade. The footprint of the building is generally 21 m by 23 m and the building structure has a mass of 10.7 million kg. The foundation consists of a 9.75 m wide pad 1.22 m deep running East-West through the middle of the footprint and two 3 m wide by 0.61 m deep footings running under the exterior columns parallel to the central footing the full length of the building. The exterior beams are connected to the central pad by stepped beams. The central pad's interface is 7 m below grade. The total mass of the foundation is 0.14 million kg. Soil conditions are reported as a medium to dense sand mixed with gravel from grade to a depth of 275 m.

An eccentric-mass shaker was attached to the roof and a velocity transducer monitored the response of the structure at the roof while three velocity transducers monitored the foundation. Tests were conducted in both the North-South direction and East-West direction. The force imparted on the roof was dependent on the frequency at which the shaker was performing. Luco, Trifunac, and Wong (1988) then analyze the data from both the structure and foundation to calculate impedance functions which accurately model the soil. Impedance functions for frequencies from 0.8 to 2.5 Hz were produced in the horizontal and rocking modes.

Wong, Trifunac, and Luco (1988) compare measured and predicted impedance functions for the Millikan library. The tests and data recorded in Luco, Trifunac, and Wong (1988) were

used to produce impedance functions and were compared to predicted values. Impedance functions comparisons are presented for frequencies ranging from 0.8 to 2.5 Hz.

Luco and Wong (1990) report displacements during dynamic loading for a model of a nuclear containment structure in Lotung, Taiwan and compare them to various displacement predictions for a 98,000 N dynamic force. The model consisted of an elastic structure with an external diameter of 10.50 m and a wall thickness of 0.30 m. The height was 14.33 m. The top of the structure was a rigid disc of diameter 9.9 m and thickness of 1.35 m. The structure's mass was 598,000 kg. It rested on a base that was 1.06 m thick and had a diameter of 10.80 m with a mass of 234,000 kg. The base and structure combination was embedded a total of 4.72 m. Soil conditions at the site required for impedance function predictions were cited but not reported.

Dynamic forces were applied to the roof of the structure by a shaker covering various frequency ranges and force magnitudes. The structure and foundation were monitored by accelerometers and converted to displacements. Displacements were determined from measurements and results normalized to correspond to a dynamic force of 98,000 N. A comparison between measured displacements and predicted displacements is presented ranging from 1 to 30 Hz.

For the vertical mode of vibration, a single-degree-of-freedom model of rigid body motion is reasonable, and determination of an impedance function is elementary with computational tools that easily handle the mathematics of complex numbers, e.g., Mathcad, Matlab. Equation 2-6 presents the equation for single-degree-of-freedom vertical impedance,  $S_v$ , and is simply defined as the force imparted on the soil by the foundation,  $F_v$ , divided by the vertical displacement of the foundation,  $U_v$ .

$$S_v = \frac{F_s}{U_v} \tag{2-6}$$

The soil force,  $F_s$ , is a function of the applied vertical force and the inertia of the foundation due to vertical movement as presented in Equation 2-7.  $F_T$  is the vertical force applied to the foundation,  $M_0$  is the mass of the foundation and  $U_v$  is the maximum vertical displacement of the foundation, and  $\omega$  is the angular frequency of the system.

$$F_s = F_T + \omega^2 M_0 \bar{U}_v \quad (2-7)$$

For horizontal or moment loading contained within a single plane, the horizontal sliding and rocking modes are often coupled, and a two-degree-of-freedom dynamic model of rigid body motion is required. In general, these equations involve four impedances, namely, horizontal, rocking, the coupling of rocking with horizontal sliding, and the coupling of horizontal sliding with rocking, to describe the horizontal displacement and rotation response of the foundation. Initially, this strategy is problematic since only two independent responses can be measured (e.g., horizontal displacement and rotation), yet four unknown impedances are to be determined. As a remedy, it is possible to assume that the cross-coupling impedances are negligible, thus allowing the horizontal sliding and rocking impedances to be computed from the two measurements (similar to vertical mode discussed above) as presented in Equation 2-8 and Equation 2-9.

$$S_h = \frac{F_s}{U_h} \quad (2-8)$$

$$S_r = \frac{M_s}{\Phi_b} \quad (2-9)$$

In this case,  $U_h$  is the maximum horizontal displacement of the foundation bottom interface with the soil. The horizontal soil force, represented by  $F_s$ , is similar to the vertical soil force because of footing inertia. Calculation of  $F_s$  becomes more complicated as it is necessary to account for changes in sliding force due to rotation of the foundation and the translation of any

structure attached to the footing. Thus Equation 2-10 represents the sliding force used to calculate horizontal impedance.

$$F_s = F_T + \omega^2 (M_0 \bar{U}_b - M_0 b_2 \bar{\Phi}_b) + \omega^2 \{1\}^T [M] \{\bar{U}\} \quad (2-10)$$

The horizontal force imparted on the foundation is  $F_T$ . The second term accounts for foundation motion where  $\omega$  is still the angular frequency of the system,  $M_0$  remains foundation mass,  $\bar{U}_b$  is the total motion of the instrumentation measuring horizontal motion,  $b_2$  is the distance from the instrumentation to the center of gravity of the foundation,  $\bar{\Phi}_b$  is the maximum rotation of the foundation. The third term accounts for structural effects on the foundation. To calculate structural effects on the foundation, the structure is separated into individual points each with mass properties. This separation is performed because the frame may not be considered rigid. Each point is treated as a point that will move a unique magnitude and thus, impart a force on the foundation. The angular frequency  $\omega$ , matrix of point masses  $[M]$  and their corresponding maximum displacements  $\{\bar{U}\}$  make up this term. The matrix  $\{1\}$  is an identity matrix to allow the multiplication of  $[M]$  and  $\{\bar{U}\}$ .

The rocking impedance of Equation 9 is the measure of the moment produced by the soil per amount of rotation. The rotation of the foundation is represented by  $\bar{\Phi}_b$ . The Rocking moment,  $M_s$ , is defined in Equation 11.

$$M_s = (H_F + h_0)F_T + \omega^2 M_0 b_1 \bar{U}_b + \omega^2 (I_0 - M_0 b_1 b_2) \bar{\Phi}_b + \omega^2 (\{h\}^T + h_0 \{1\}^T) [M] \{\bar{U}\} \quad (2-11)$$

The rocking moment is calculated around the foundation soil interface at the horizontal center of the footing. Many variables used to calculate the horizontal sliding force and the rocking moments are shared. Those that are not shared include the height of the force acting on the frame which is represented by  $H_F$ , thickness of the foundation,  $h_0$ , the distance from the

center of gravity of the foundation to its bottom,  $b_1$ , the mass moment of inertia about the axis that the foundation is rotating,  $I_0$ . As with dynamic horizontal force calculations, dynamic moment calculations require the influence of the structure. The structure is separated into point masses with corresponding elevations and moments which, along with displacements and angular frequency, are used to calculate the dynamic effect of the frame on the foundation. The only unmentioned variable to this point is  $\{h\}$  which is a matrix representing the height of the corresponding point masses.

Alternatively, the foundation response can be predicted via a two-degree-of-freedom system. This requires measurements from two independent loading configurations. By combining the results of the two experiments, the four measured response (i.e., two displacements and two rotations) can be used to determine the four unknown impedances as follows in Equation 2-12 through Equation 2-15.

$$S_h = \frac{\overline{\Phi}_{b2}F_{s1} - \overline{\Phi}_{b1}F_{s2}}{U_{0y1}\overline{\Phi}_{b2} - U_{0y2}\overline{\Phi}_{b1}} \quad (2-12)$$

$$S_r = \frac{U_{0y2}M_{s1} - U_{0y1}M_{s2}}{U_{0y2}\overline{\Phi}_{b1} - U_{0y1}\overline{\Phi}_{b2}} \quad (2-13)$$

$$S_{rh} = \frac{\overline{\Phi}_{b2}M_{s1} - \overline{\Phi}_{b1}M_{s2}}{U_{0y1}\overline{\Phi}_{b2} - U_{0y2}\overline{\Phi}_{b1}} \quad (2-14)$$

$$S_{hr} = \frac{U_{0y2}F_{s1} - U_{0y1}F_{s2}}{U_{0y2}\overline{\Phi}_{b1} - U_{0y1}\overline{\Phi}_{b2}} \quad (2-15)$$

The impedances are horizontal,  $S_h$ , rocking,  $S_r$ , and two coupling terms,  $S_{rh}$  and  $S_{hr}$ . Impedances are calculated using the same inputs and responses used to calculate uncoupled impedances. Subscripts 1 and 2 designate from which configuration variables are measured or calculated. Variables include the force imparted on the foundation,  $F_s$ , the moment applied to the

foundation,  $M_s$ , the rotation of the foundation,  $\bar{\Phi}_b$ , and the displacement of the foundations center of gravity,  $U_{0y}$ , calculated in Equation 16.

$$U_{0y} = \bar{U}_b - \bar{\Phi}_b b_2 \quad (2-16)$$

Of course, this strategy assumes that the impedances appropriately describe the foundation-soil interaction for each experiment configuration. An executable program (CONAN) is also provided, along with complete details of its use.

To define the coupling terms via the method above, it is assumed that  $S_{rh}$  and  $S_{hr}$  are independent of each other. Another approach assumes that  $S_{rh}$  and  $S_{hr}$  are equal and overdetermined. Hence, a least squares solution can be used to calculate the four impedances.

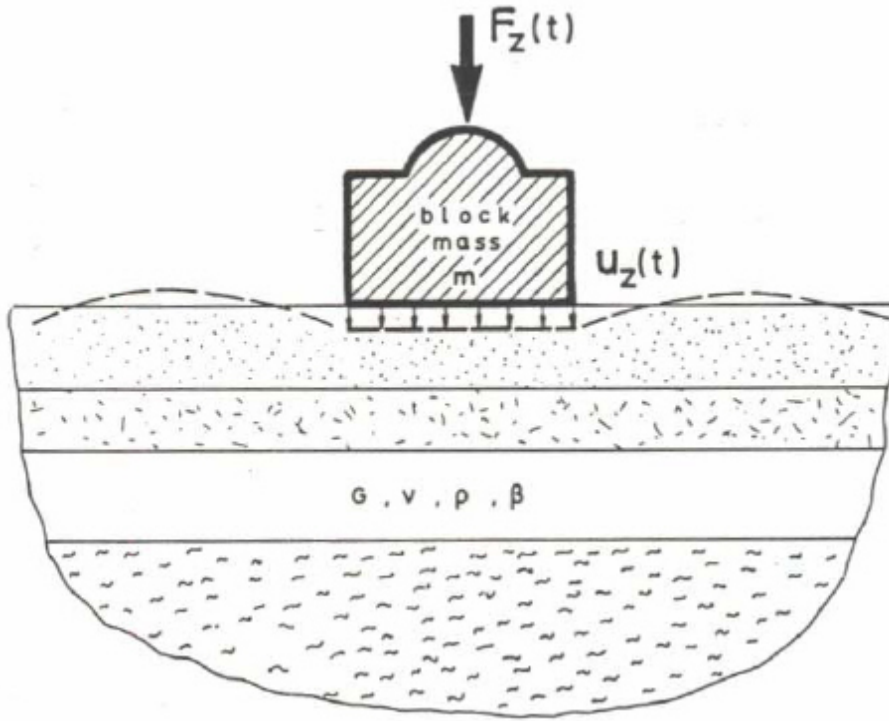


Figure 2-1. Foundation / Soil Diagram. (Gazetas [1991])

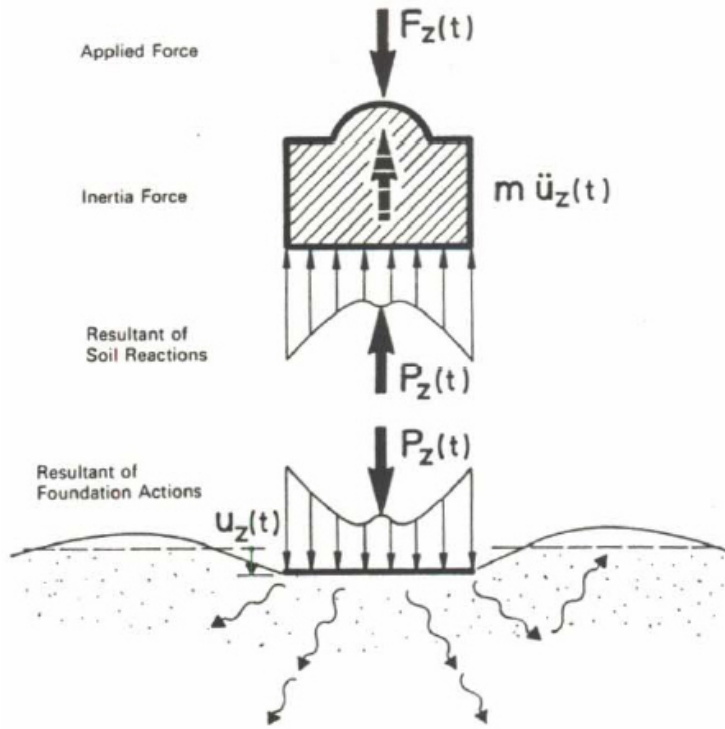


Figure 2-2. Foundation Free Body Diagram. (Gazetas [1991])

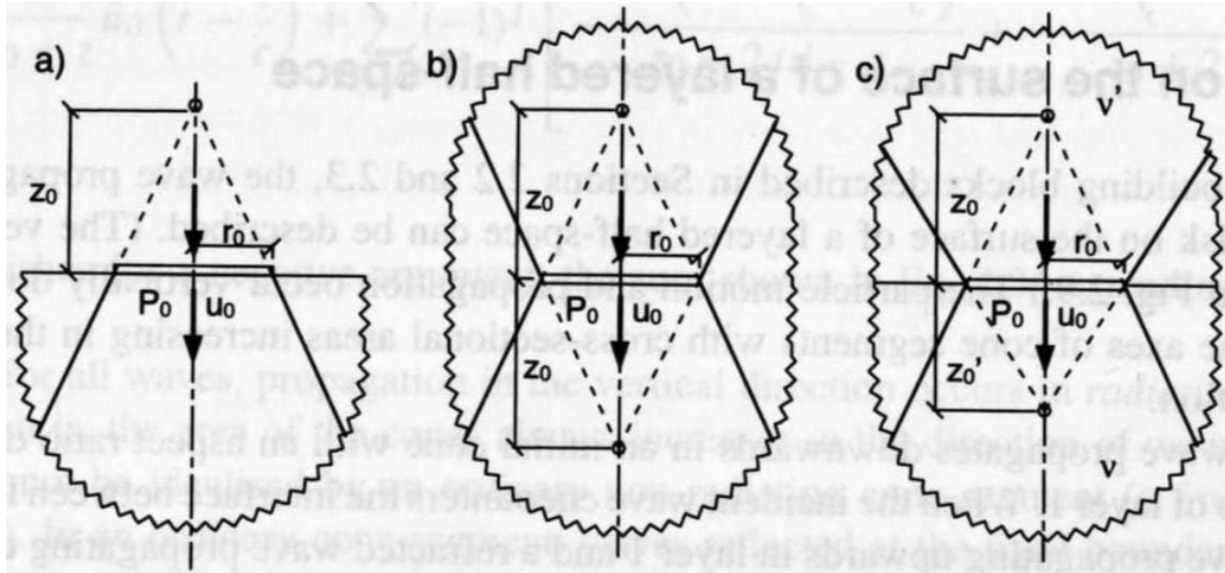


Figure 2-3. Cone Diagrams. (Wolf and Deeks [2004])

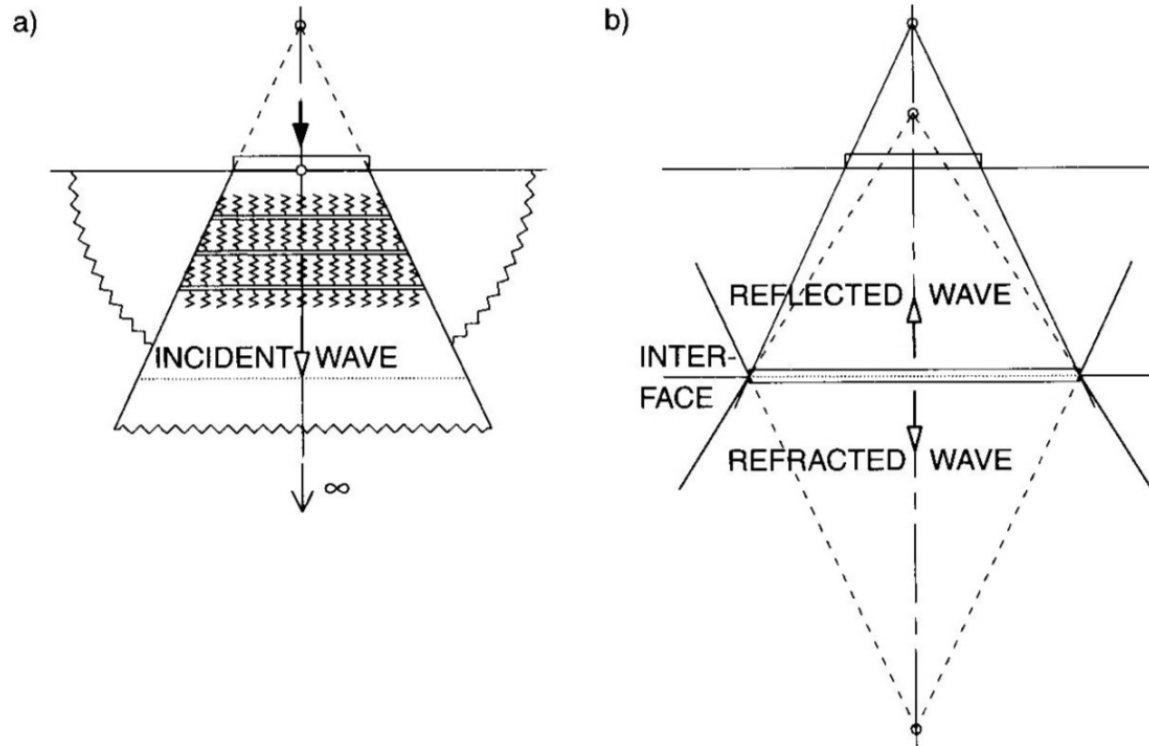


Figure 2-4. Reflected and Refracted Wave Diagram. (Wolf and Deeks [2004])

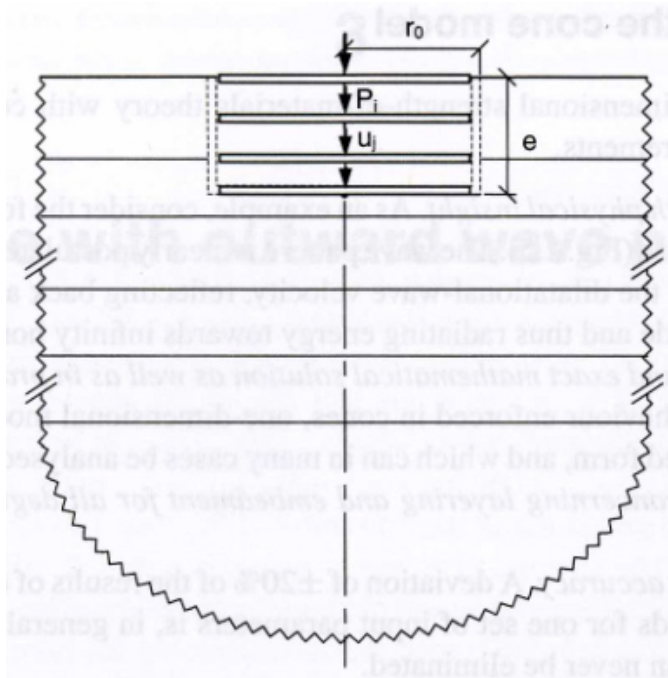


Figure 2-5. Embedded Stacked Disks. (Wolf and Deeks [2004])

## CHAPTER 3 CONE MODEL PREDICTIONS

Many dynamic impedance function prediction methods are available. Precise numerical methods tend to be extremely cumbersome often rendering them unpractical for widespread use. Cone models on the other hand are relatively simple when compared to other methods potentially making them highly effective for typical design scenarios. The following chapter first demonstrates similarities between predicted impedance functions produced via numerical methods and those produced by cone modeling. Cone model solutions for square and rectangular footings on the surface of and embedded in both homogeneous and layered profiles are compared with theoretical solutions of Wong and Luco (1978, 1985), Mita and Luco (1989), and Apsel and Luco (1987) available in the literature. Next cone model solutions for surface and embedded round, square, and rectangular footings are compared with actual measured behavior. While the database is limited, the well-documented work of Nii (1987) for small-scale foundations, and Crouse, et al. (1990) for footings of actual size, provide useful measured foundation behavior to compare with cone model predictions. These evaluations will further demonstrate that sufficient engineering accuracy can be obtained via the strength-of-materials based analyses of cone models.

### **3.1 Wolf and Deeks (2004)**

To analyze the vibrations of a foundation on the surface of or embedded in a layered half-space, Wolf and Deeks (2004) have presented an approach using conical bars and beams, called cones. With these models, the complicated, exact formulation of three-dimensional elastodynamics is replaced by simple one-dimensional description of the theory of strength of materials, postulating the deformation behavior (plane sections remain plane). A half-space with linear elastic behavior and hysteretic material damping can consist of any number of horizontal

layers either overlying a half-space or fixed at its base. Besides cylindrical foundations, axi-symmetric configurations of arbitrary embedment shape can be processed, with the wall and base of the embedded foundation assumed to be rigid. Dynamic-stiffness coefficients describing the interaction force-displacement relationship are calculated for all frequencies. Only approximations of the one-dimensional strength-of-materials approach based on wave propagation in cones apply, and no other assumptions are made. For each degree of freedom, only one type of body wave exists: for the horizontal and torsional motions, S-waves propagating with the shear-wave velocity; and for the vertical and rocking motions, P-waves propagating with the dilatational-wave velocity. The corresponding displacements can be formulated directly in closed form as a function of the depth of the site, without any spatial Fourier transformation into the wave number domain.

Wolf and Deeks (2004) have presented extensive evaluation of their methodology. In these evaluations, cone model predictions are compared with results from rigorous, three-dimensional, elastodynamic solutions, usually the thin-layer finite element method. The evaluations are presented for axi-symmetric foundations, for all degrees of freedom, and for dimensionless frequencies typically up to six. The half-space materials are assumed to be linear elastic with hysteretic material damping. Embedded foundations are assumed to be in full contact with surrounding soil. The specific cases examined are as follows:

- Both surface and embedded cylindrical foundations on/in a homogeneous half-space.
- Both surface and embedded cylindrical foundations on/in a homogeneous layer fixed at its base.
- Cylindrical foundations on the surface of a layered half-space.
- Cylindrical foundations embedded in a layered half-space.

- A cylindrical foundation embedded in an incompressible, layered half-space.
- A hemi-ellipsoid embedded in a homogeneous half-space.
- A sphere embedded in a homogeneous full-space.

For all of these cases, the deviations in impedance functions between cone model predictions and the rigorous solutions are within the range  $\pm 20\%$ . Wolf and Deeks (2004) conclude that this is sufficient engineering accuracy.

### **3.2 Wong and Luco (1978)**

While the extensive evaluation results presented by Wolf and Deeks (2004) are convincing, it is also fair to observe that most real shallow foundations are not axi-symmetric. In fact, the majority of real shallow foundations are probably rectangular in shape. Hence, the first evaluation presented herein is to assess the ability of cone models to determine impedance functions for non-axi-symmetric foundations, in this case rectangular.

Wong and Luco (1978) have presented a detailed tabulation of numerical values for the impedance functions for a massless, rigid, rectangular foundation perfectly bonded to the surface of a viscoelastic, homogeneous half-space. Impedance functions are provided in normalized form for four aspect ratios, namely length/width=1, 2, 3, and 4, and for dimensionless frequencies up to 10. The computations have been performed for two values of Poisson's ratio,  $\nu=0.33$  and  $0.45$ , and for three values of hysteretic damping ratio,  $\xi=0, 0.02, \text{ and } 0.05$ .

Five specific rectangular foundation models were constructed to compare cone model predictions with the tabulated results of Wong and Luco (1978). Models 1-4 consisted of foundations with aspect ratios of 1, 2, 3, and 4, respectively, and a Poisson's ratio of  $\nu=0.33$ . Model 5 was a rectangular foundation with an aspect ratio of 4, and a Poisson's ratio of  $\nu=0.45$ .

All models were constructed using a foundation width of 2 m, a shear wave velocity of 125 m/s, a mass density of 1600 kg/m<sup>3</sup>, and a hysteretic damping ratio,  $\xi=0.05$ .

For each of the five models, cone model impedance functions for vertical, horizontal, rocking, and torsional degrees of freedom were calculated using the CONAN executable program provided by Wolf and Deeks (2004). Please note that the cone models assume that the coupling impedance of a surface foundation is zero. Indeed, the coupling impedances tabulated by Wong and Luco (1978) are small in comparison to the other degrees of freedom. Also, since the cone model impedances are calculated for circular disk (axi-symmetric) foundations, each of the five rectangular foundations were converted to an equivalent disk for CONAN computations. The equivalency was based upon contact area for translational modes (vertical, horizontal), and moment of inertia for rotational modes (rocking, torsion).

By way of example, Figure 3-1 to Figure 3-10 present impedance function comparisons for Models 1 and 4, respectively. Each figure displays impedance functions for a degree of freedom as computed by CONAN. In each figure, impedance functions are expressed by three graphs and are compared with the corresponding Wong and Luco (1978) data. Real (stiffness) and imaginary (damping) components are represented in Graphs A and B respectively. Graph C plots the magnitude of the impedance function in dimensional form versus frequency. Impedance function magnitude is simply the vector summation of the real and imaginary components. It is observed that for all cases of imaginary components and magnitude presented, the  $\pm 20\%$  engineering accuracy documented by Wolf and Deeks (2004) is maintained for these foundations on the surface of a homogeneous half-space. Many of the real components also demonstrate agreement within this accuracy while those that do not are of comparable magnitude as well as trend. While it may not be surprising that results for a square shape are very similar to

an axi-symmetric solution (Figure 3-1 through Figure 3-4), it is also evident that the cone model solutions are in good agreement for a rectangular footing with an aspect ratio as large as four (Figure 3-5 through Figure 3-10). It should also be noted that the comparison results for the remaining Models 2, 3, and 5 not shown herein are of equal or better quality.

### **3.3 Mita and Luco (1989)**

To explore the influence of foundation embedment, Mita and Luco (1989) have presented a detailed tabulation of numerical values for the impedance functions of a massless, rigid, square foundation embedded in and perfectly welded to a viscoelastic, homogeneous half-space. Impedance functions for horizontal, coupling, rocking, vertical, and torsional degrees of freedom are provided in normalized form for embedment to half-width ratios up to 1.5, and for dimensionless frequencies up to three. The computations have been performed for three values of Poisson's ratio,  $\nu=0.25, 0.33$  and  $0.4$ . All computations assumed hysteretic damping ratios of  $0.001$  for shear waves, and  $0.0005$  for compression waves. The numerical results were calculated using a hybrid approach described by Mita and Luco (1987). Five specific square foundation models were constructed to compare cone model predictions with the tabulated results of Mita and Luco (1989). Models 1-3 consisted of foundations with embedment to half-width ratios of  $0, 0.5,$  and  $1.5,$  respectively, and a Poisson's ratio of  $\nu=0.33$ . Model 4 was a square foundation with an embedment to half-width ratio of  $1.5,$  and a Poisson's ratio of  $\nu=0.25,$  while Model 4 was a square foundation with an embedment to half-width ratio of  $1.5,$  and a Poisson's ratio of  $\nu=0.4$ . All models were constructed using a foundation width of  $2$  m, a shear wave velocity of  $125$  m/s, a mass density of  $1600$  kg/m<sup>3</sup>, and hysteretic damping ratios as noted above for the Mita and Luco (1989) results. As with the comparisons presented above, cone models for these square footings were based upon equivalent circular disks.

By way of example, Figure 3-11 through Figure 15 present impedance function comparisons for Model 3, a case with maximum embedment. In each figure, impedance functions for each degree of freedom and as computed by CONAN are compared with the corresponding Mita and Luco (1989) data. As in the previous sections, plotted in each figure are the real and imaginary components represented in Graphs A and B respectively and, in Graph C, the magnitude of the impedance function in dimensional form versus frequency. It is observed that for all cases presented, with the exception of Figure 3-15 A, the  $\pm 20\%$  engineering accuracy documented by Wolf and Deeks (2004) is also maintained for these square foundations embedded in a homogeneous half-space. Though a segment of the plot in Figure 3-15 A does not fall within the desired engineering accuracy, the graph demonstrates a magnitude and trend that is comparable between CONAN and Mita and Luco (1989). It should also be noted that the comparison results for the remaining Models 1, 2, 4, and 5 not shown herein are of equal or better quality.

### **3.4 Wong and Luco (1985)**

To explore the influence of soil layering, Wong and Luco (1985) have presented a detailed tabulation of normalized horizontal, coupling, rocking, vertical, and torsional impedance functions for a rigid, massless, square foundation resting on two types of layered viscoelastic soil models. The first soil model consists of a uniform layer over a uniform half-space, while the second model consists of a layer with linearly varying properties over a uniform half-space. The impedance functions have been calculated based upon an extension to the case of layered media of the approach proposed by Wong and Luco (1976). The approach computes a numerical solution of an integral equation involving the Green's functions for a layered medium. The rigid, square foundation is assumed to be perfectly bonded to the surface of the layered half-space.

The impedance function results are presented for two Poisson's ratio combinations: 1)  $\nu_1=0.33$  for the layer, and  $\nu_2=0.33$  for the half-space, and 2)  $\nu_1=0.45$  for the layer, and  $\nu_2=0.33$  for the half-space. Three values for the contrast in shear wave velocity between layer and half-space are provided, namely  $V_{s1}/V_{s2}=0.3, 0.6, \text{ and } 0.8$ . The density ratio between the half-space and the layer is fixed at  $\rho_2/\rho_1=1.13$ , and the material damping constants are fixed at 0.03 and 0.05 for the half-space and layer, respectively.

In each of the tables, the real and imaginary parts of the normalized impedance functions are presented for 21 dimensionless frequencies ranging from 0.1 to 5.0, and for five values for the ratio of layer thickness (H) to foundation half-width (a):  $H/a=0.5, 1, 2, 3, \text{ and } 4$ .

Eight specific square foundation models were constructed to compare cone model predictions with the tabulated results of Wong and Luco (1985). For simplicity, all eight models consisted of a uniform layer over a half-space. In addition, all cone models were assigned a fixed density ratio of 1.13, and fixed material damping values of 0.03 and 0.05, as noted above for the Wong and Luco (1985) results. As with the comparisons presented above, cone models for these square footings were based upon equivalent circular disks. Additional parameters for the eight models are shown in Table 3-1.

Model 1 was chosen as a basis model with the parameters indicated. For Models 2-8, the parameters shown in Table 3-1 are those that are different from Model 1, while all other parameters remain the same. Models 2 and 3 briefly examine the issue of scale, since the Wong and Luco (1985) results are presented in dimensionless format. Model 2 has a foundation half the size of Model 1, while Model 3 has increased the shear wave velocity of the layer by a factor of two. Models 4 and 5 address the influence of layer thickness, Models 6 and 7 the influence of stiffness contrast, and Model 8 the influence of Poisson's ratio. While these eight models

certainly do not exhaust the full range of possibilities presented by the Wong and Luco (1985) data, these models explore the ranges in principal parameters.

By way of example, Figure 3-16 to Figure 3-31 present impedance function comparisons for Models 1, 4, 6, and 8, respectively. Results for the remaining Models 2, 3, 5, and 7 are also discussed below. In each figure, impedance functions for each degree of freedom and as computed by CONAN are compared with the corresponding Wong and Luco (1985) data. As in the previous sections, plotted in each graph is both real and imaginary components as well as the magnitude of the impedance function in dimensional form versus frequency. It is observed that for the vast majority of cases presented, the  $\pm 20\%$  engineering accuracy documented by Wolf and Deeks (2004) is also maintained for these square foundations on the surface of a layered half-space. The only notable exceptions for magnitude are possibly the rocking mode in Model 4, and the vertical mode in Model 8. As for the accuracy of the components of the impedance functions, there are exceptions that tend to exist at higher frequencies but plots between CONAN and Wong and Luco (1985) are similar in trends and order of magnitude. It should also be noted that the remaining Models 2, 3, 5, and 7 that are not presented herein, display equal if not better comparisons than shown in Figure 3-16 to Figure 3-31. The results for Models 2 and 3 indicate that scale is not a factor in these comparisons. Indeed, while the impedance function magnitudes change with scale, the comparisons between cone model and Wong and Luco (1985) are identical to those shown in Figure 3-1 to Figure 3-4. Also, the results for Models 5 and 7 are better than for Models 4 and 6, respectively. This is to be expected since Model 5 has a much thicker layer than either Models 1 or 4, and Model 7 has a lower stiffness contrast than either Models 1 or 6.

### **3.5 Apsel and Luco (1987)**

To evaluate the combined influence of layering and foundation embedment, Apsel and Luco (1987) present impedance functions for a cylindrical foundation embedded in a multi-layered soil profile. The foundation model was 24.4 m (80 ft) in diameter, embedded 5.5 m (18 ft) below the ground surface, and was assumed to be in full contact with the surrounding soil. The characteristics of the soil model are shown below in Table 3-2. The impedance functions are presented for horizontal, rocking, and coupled horizontal-rocking degrees of freedom for dimensionless frequencies up to 6, and were computed via an integral equation approach described in detail by Apsel and Luco (1987). Based upon these parameters, cone model impedance functions were computed via CONAN for comparison with the Apsel and Luco (1987) results, and the comparison is presented in Figure 3-32 to Figure 3-34. As in the previous sections, plotted in each figure are three graphs representing real and imaginary components and the magnitude of the impedance function in dimensional form versus frequency. It is observed that the results are generally in good agreement. In fact, the comparison appears very good for the horizontal mode. The cone model appears to slightly over predict the impedances in the higher frequency range for rocking. The coupling impedances are under predicted by CONAN for all frequencies investigated, though the trends and shape of the impedance versus frequency relationship are in good agreement with the exception of stiffness. Stiffness seems to be somewhat lower for CONAN than for Apsel and Luco (1987) though the shape and trend of the curves seem similar.

### **3.6 Nii (1987)**

While all of the impedance function solutions presented above are based upon theoretical models, Nii (1987) reported experimental results for vertical dynamic impedance of small-scale footings attached to or embedded in a model half-space. The half-space was constructed of room

temperature vulcanizing silicone rubber, and was cast in a steel tank 1.7 m long, 1.4 m wide, and 0.4 m high. The mechanical properties of the half-space are reported as follows:

- $V_s = 11.3 \text{ m/s}$
- $V_r = 10.8 \text{ m/s}$
- $V_p = 1000 \text{ m/s}$
- $\nu \approx 0.5$
- Damping ratio ( $\xi$ ) = 0.031
- $\rho = 0.98 \text{ g/cm}^3$

The model footings were constructed of acrylic resin, with dimensions as shown in Table 3-3. Nii (1987) reports that even though the acrylic footings were smooth, the surface of the half-space rubber was slightly adhesive, and the footings and half-space behaved as though they were bonded. The circular and rectangular footings were forced into vertical vibration via a mechanical shaker. The experiments were conducted at frequencies where the effects of reflected waves from the boundaries of the model half-space were negligible or diminished (Nii [1987]), and results of the experiments are reported for dimensionless frequencies up to 8.

Vertical impedances were computed with cone models for five of the experiment footings shown in Table 3-3: two circular footings, one surface and one embedded, and three rectangular footings with aspect ratios of 1, 1.5, and 2. Since the cone model impedances are calculated for circular disk (axi-symmetric) foundations, cone models for the rectangular footings were based upon equivalent circular disks, in this case based upon contact area for the vertical mode of vibration.

Cone model vertical impedance solutions are compared with the experimental results of Nii (1987) in Figure 3-35 to Figure 3-39 for each of the five footings considered. Each figure

plots real and imaginary components of the impedance function as well as its magnitude in dimensional form versus frequency. Impedance function magnitude is simply the vector summation of the real and imaginary components. It is observed that agreement between cone model predictions and the Nii (1987) experimental results is quite good at low frequencies for all five cases. There is a consistent under-prediction of the magnitude at higher frequencies for all five cases. Evaluation of the real (stiffness) and imaginary (damping) components of the impedance functions also reveals a consistent pattern for all five cases: the real component is over-predicted, while the imaginary component is under-predicted, with a net under-prediction of the overall magnitude as noted in the figures. However, the  $\pm 20\%$  engineering accuracy for magnitude documented by Wolf and Deeks (2004) appears to be maintained, except for maybe the embedded, circular footing (Figure 3-36 C). Real and imaginary components of Luco and Mita (1987) deviate from Nii (1987) and CONAN values at higher frequencies but still produce nearly matching magnitudes. Also shown in figures 3-35, 3-37 and 3-39 are cases that impedance functions from the literature that were determined via more rigorous, three-dimensional, elastodynamic solution techniques. The solution for the surface case (Figure 3-35) was obtained from Luco and Mita (1987). The two solutions for the rectangular footings (Figure 3-37 and Figure 3-39) were obtained from Wong and Luco (1978). Solutions for the two remaining cases (circular, fully embedded and rectangular, surface, length/width = 1.5) were not readily available for Poisson's ratio near 0.5. First, it is noted that the three impedance functions (experimental, rigorous, and cone) are in good accord for the three cases presented (circular, square, and rectangular). This is encouraging. On the other hand, as one might expect, there is closer agreement between the "rigorous" impedance function solutions from the literature and the experimental results, than between the "approximate" cone model solutions and the experimental

results. However, it is interesting to note that the relative agreement between impedances for all three cases presented is very similar. This might suggest that the “error” in the cone model impedances is not due to approximating a square or rectangular footing with an equivalent disk.

### **3.7 Crouse, et al. (1990)**

While comparison with the experimental results of Nii (1987) is encouraging, Nii’s experiments employed small-scale laboratory tests using foundation and support materials that were not concrete and soil. It is likely that the bond between foundation and support material in these experiments is more ideal than between concrete and soil, and thus more closely matched the conditions assumed in the theoretical models. It is widely recognized that intimate bond is typically not realized in real, full-scale geotechnical foundation conditions, particularly for embedded foundations along the foundation sidewall/soil interface. Further, these experiments were conducted using a support material that is likely very homogenous compared to soil, and represents the simplest case to model.

Crouse, et al. (1990) report experimental impedance functions for two small concrete foundations supported by soil and in real field conditions. Both foundations were utilized to support earthquake accelerograph stations. One foundation (Cholame 1E) was located in central California, and consisted of a 10-cm (4-in.) thick, 1.27-m (50-in.) square slab resting on corner piers and embedded in a moderately stiff alluvial deposit. The other foundation (Station 6) was a 15-cm (6-in.) thick, 1.22-m x 1.14-m (48-in. x 45-in.) nearly square slab, embedded 7.6 cm (3 in.) in a softer deposit in southern California. Shear wave velocity profiles were determined for each site via in situ SASW tests, and reported in detail by Crouse, et al. (1990). The soils at both sites were assumed by Crouse, et al. to have a unit weight of  $17,300 \text{ N/m}^3$  ( $110 \text{ lb/ft}^3$ ), a Poisson’s ratio of  $1/3$ , and a material damping ratio of 0.015.

To determine impedance functions, forced harmonic vibration tests were performed on the foundations. Harmonic forces were induced with a small (156 N, 35 lb) eccentric-mass vibration shaker bolted to the foundation surface. The measured response was determined via triaxial accelerometers mounted at each corner of the foundation. The impedance functions were then determined from the induced force and measured response via appropriate equations of motion for the dynamic system. The impedance functions are presented for the vertical, horizontal, and rocking modes of vibration and for frequencies from 10 to 60 Hz.

Using the foundation and soil support physical characteristics and properties as input, impedance functions were computed with cone models for the Station 6 foundation. Since the cone model impedances are calculated for circular disk (axi-symmetric) foundations, the actual square foundation was converted to an equivalent disk for cone model computations. The equivalency was based upon contact area for translational modes (vertical, horizontal), and moment of inertia for rotational modes (rocking). Cholame 1E was not investigated for this study since the corner piers supporting the concrete slab produce a more complex foundation system than is likely appropriate for the cone model approach.

Cone model impedance solutions are compared with the experimental results of Crouse, et al. (1990) in Figure 3-40 to Figure 3-42. Each graph plots real and imaginary components along with the magnitude of the impedance function in dimensional form versus frequency. Impedance function magnitude is simply the vector summation of the real and imaginary components. The three sets of data for each of the Crouse, et al. impedance functions correspond to the three different shaker eccentricities used during the experiments. The induced load increases with increasing frequency for an eccentric-mass shaker, thus the eccentricity was lowered from an

initial setting in two increments as frequency increased to prevent significant nonlinear response of the dynamic system.

While agreement between cone model predictions and experiment results are not as good as with the Nii (1987) experiments, it is observed that the agreement is credible and encouraging. The impedances are all of similar magnitude, and the trends are similar for the vertical and horizontal modes. There is a disparity in shape for the rocking mode. Unlike the simple homogeneous foundation support system in the Nii (1987) experiments, the soil profile at Station 6 is non-homogeneous and multi-layered, yet the cone model predictions appear reasonable. Perhaps the most notable disparity for Station 6 is that the cone models generally over-predict the impedance magnitude, which is opposite the findings presented above for the Nii (1987) experiments. Over-prediction for Station 6 could be due to many contributing factors. Both ideal bond between foundation and soil, and efficient radiation of energy from the vibrating foundation through the supporting soil would create a larger predicted impedance magnitude. Neither of these can be expected from a real geotechnical foundation system. Despite these encouraging results, it is probably fair to conclude that the  $\pm 20\%$  engineering accuracy documented by Wolf and Deeks (2004) is not maintained for these comparisons with measured foundation behavior. Obviously, a much larger database of comparisons is desired before more definitive conclusions can be drawn.

Table 3-1. Parameters for Eight Wong and Luco (1985) Comparisons

Model no.	Parameters*	Comment
1	$V_{s1}/V_{s2} = 0.6$ , $\nu_1 = 0.33$ , $H/a = 2$ $a = 2$ m, $V_{s1} = 125$ m/s, $\rho_1 = 1600$ kg/m <sup>3</sup>	Basis model
2	$a = 1$ m	Influence of scale: 1/2 footing size
3	$V_{s1} = 250$ m/s	Influence of scale: 2x shear wave velocity
4	$H/a = 0.5$	Influence of layer thickness: 1/4 layer thickness
5	$H/a = 4$	Influence of layer thickness: 2x layer thickness
6	$V_{s1}/V_{s2} = 0.3$	Influence of stiffness contrast: higher
7	$V_{s1}/V_{s2} = 0.8$	Influence of stiffness contrast: lower
8	$\nu_1 = 0.45$	Influence of Poisson's ratio: higher

Note: For Models 2-8, the parameters shown are those that are different from the parameters for the Basis Model 1.

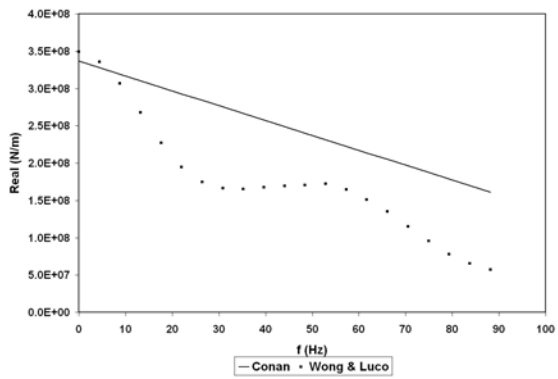
Table 3-2. Soil Profile for Apsel and Luco (1987) Model

Layer no.	Layer thickness (m)	Unit weight (kN/m <sup>3</sup> )	Wave velocity (m/s)		Material damping ratio	
			S	P	S	P
1	1.8	20.89	192.0	384.0	0.01	0.005
2	3.7	20.89	338.3	676.7	0.01	0.005
3	4.3	20.89	420.6	841.2	0.01	0.005
4	10.4	20.89	487.7	975.4	0.01	0.005
5	82.3	20.89	609.6	1219.2	0.01	0.005
6	16.2	20.89	762.0	1524.0	0.01	0.005
7	∞	20.89	944.9	1889.8	0.01	0.005

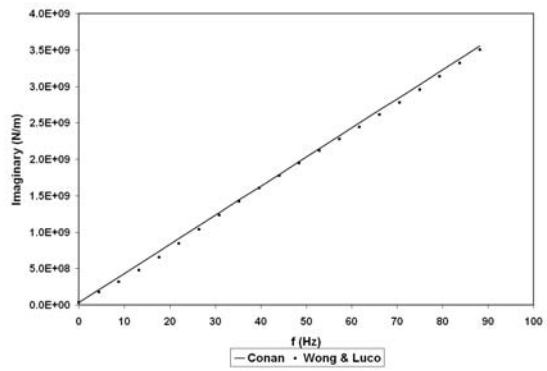
Table 3-3. Model Footings of Nii (1987)

Shape					
Circular			Rectangular on surface		
Location	Radius (cm)	Thickness (cm)	Length/Width	½ Width (cm)	Thickness (cm)
Surface	1*, 2, 3, & 4	1	1	1*, 2, 3, & 4	1
Fully embedded	2*	2	1.5	1*, 2, & 3	1
			2	1* & 2	1

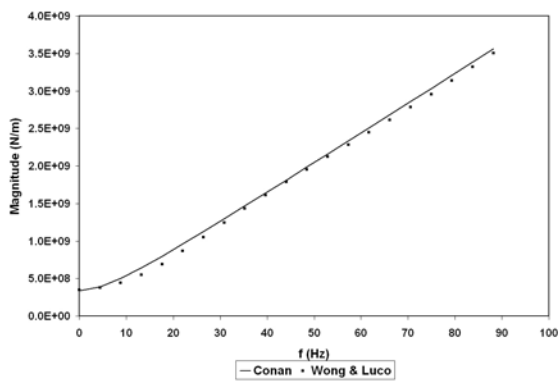
Note: Analyzed via cone model herein.



A

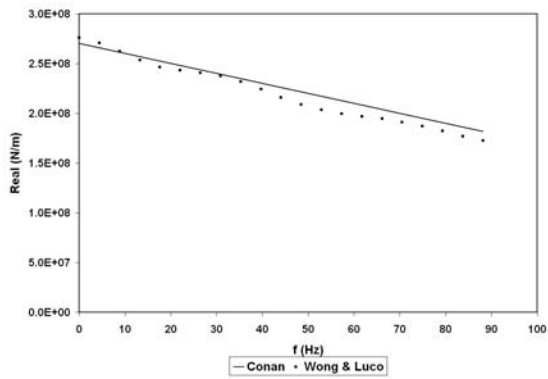


B

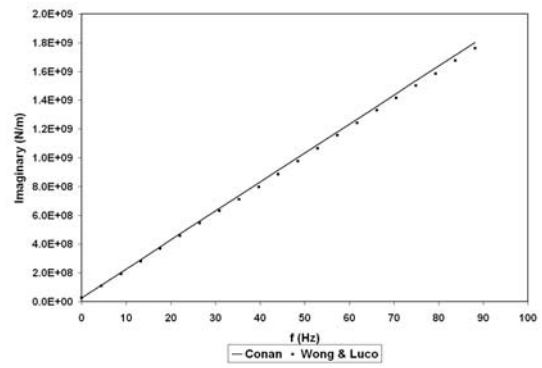


C

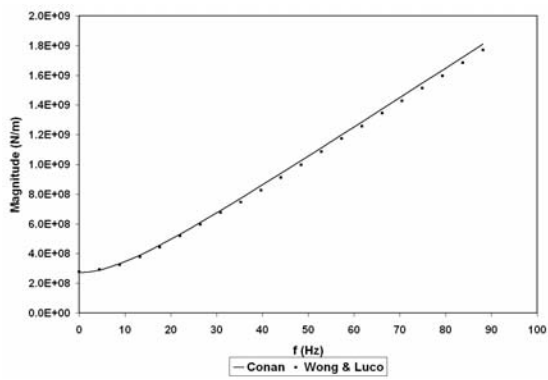
Figure 3-1. Vertical Impedance Functions for Model 1, Wong and Luco (1978). A) Real. B) Imaginary. C) Magnitude.



A

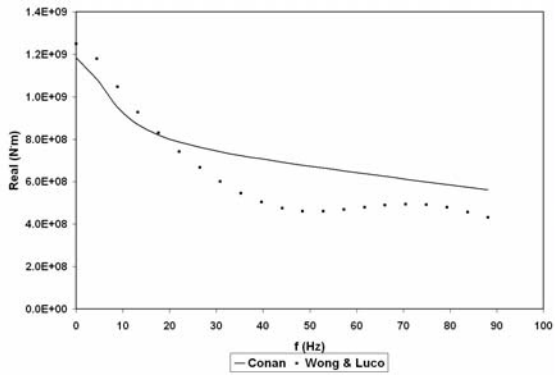


B

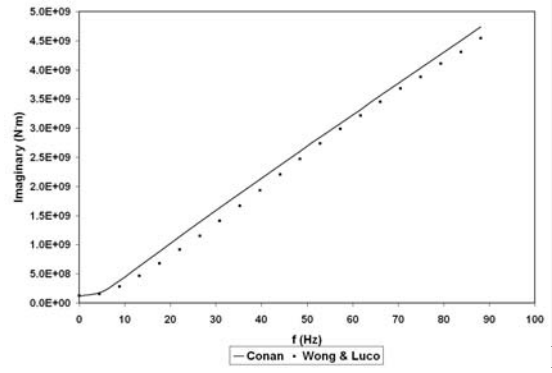


C

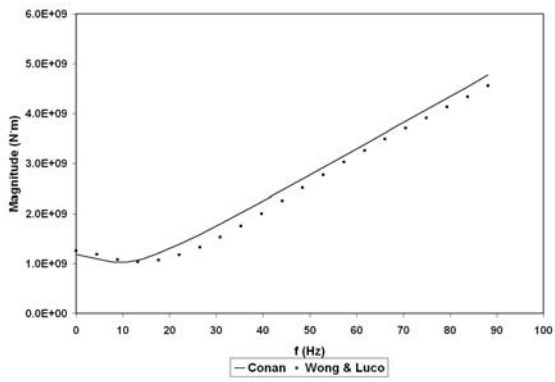
Figure 3-2. Horizontal Impedance Functions for Model 1, Wong and Luco (1978). A) Real. B) Imaginary. C) Magnitude.



A

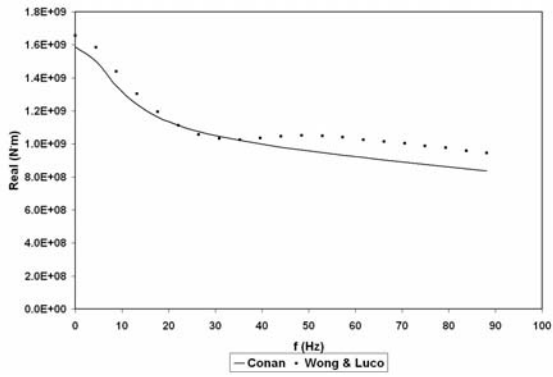


B

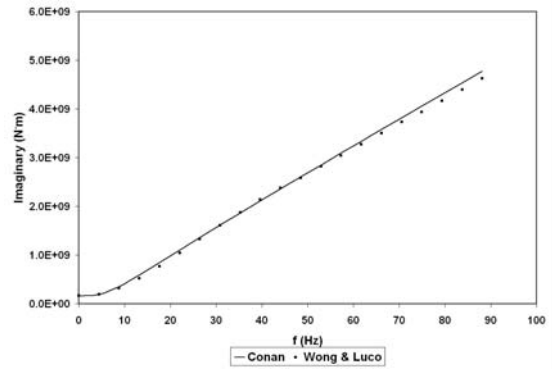


C

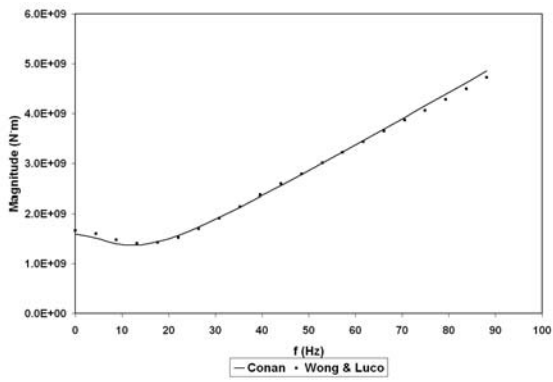
Figure 3-3. Rocking Impedance Functions for Model 1, Wong and Luco (1978). A) Real. B) Imaginary. C) Magnitude.



A

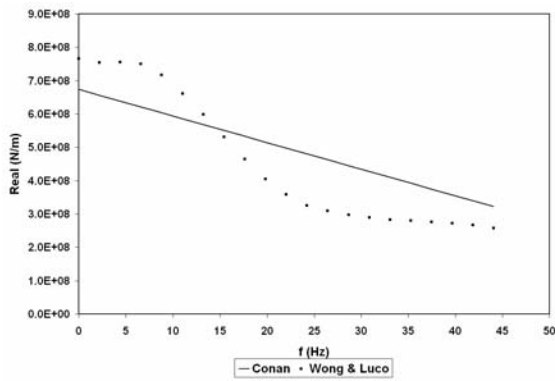


B

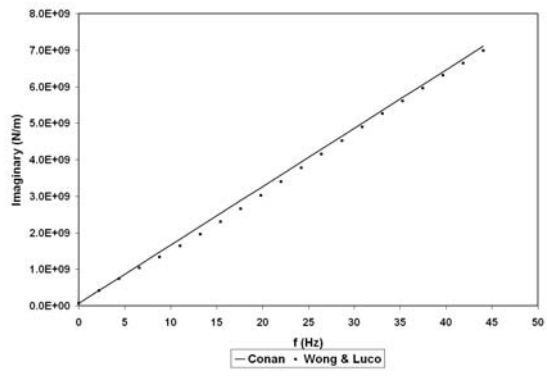


C

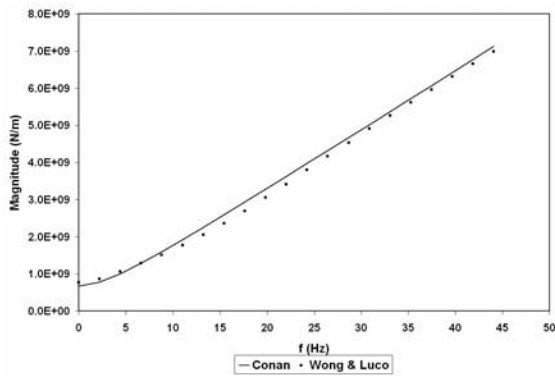
Figure 3-4. Torsion Impedance Functions for Model 1, Wong and Luco (1978). A) Real. B) Imaginary. C) Magnitude.



A

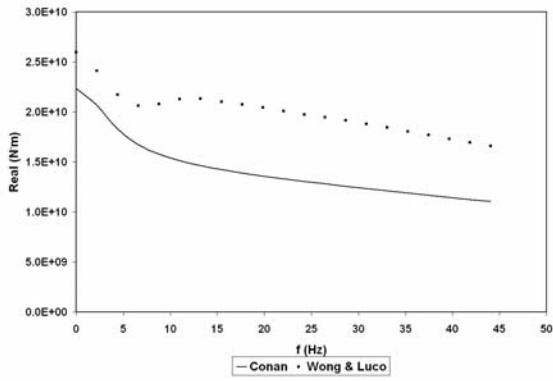


B

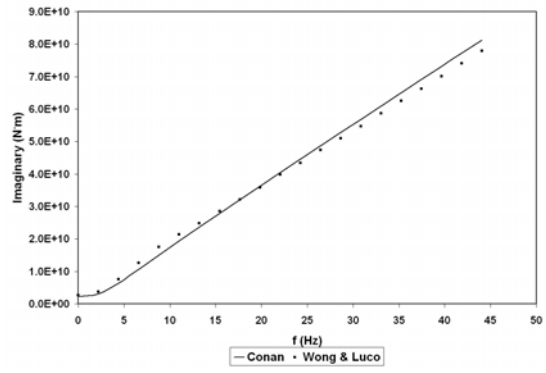


C

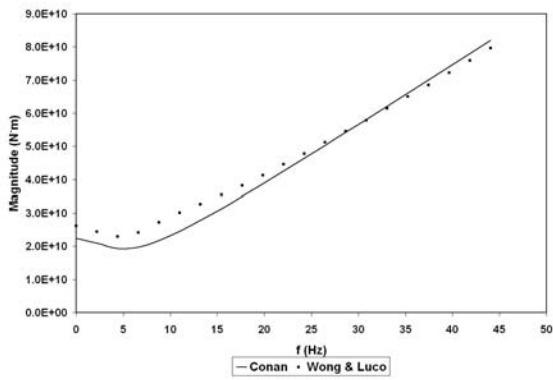
Figure 3-5. Vertical Impedance Functions for Model 4 Length/Width=4, Wong and Luco (1978).  
 A) Real. B) Imaginary. C) Magnitude.



A

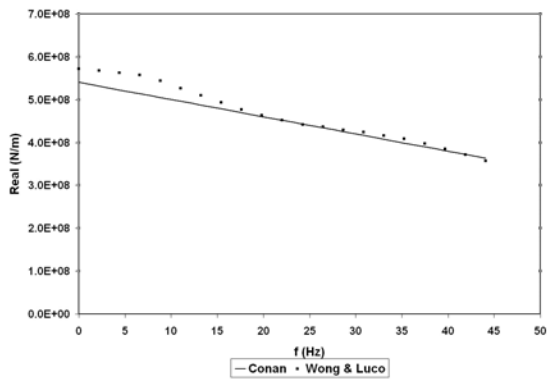


B

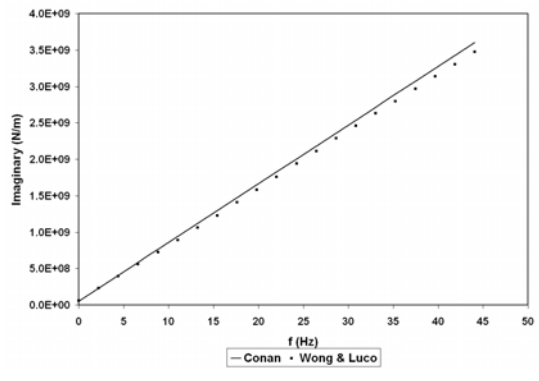


C

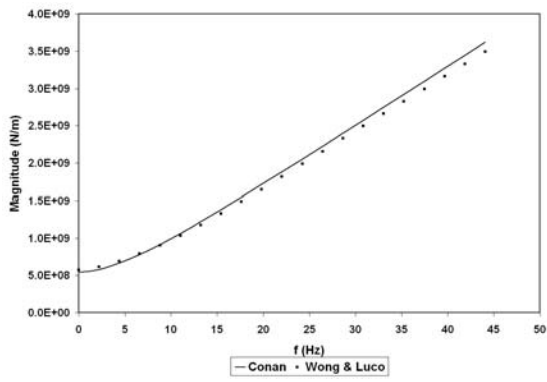
Figure 3-6. Torsion Impedance Functions for Model 4 Length/Width=4, Wong and Luco (1978).  
 A) Real. B) Imaginary. C) Magnitude.



A

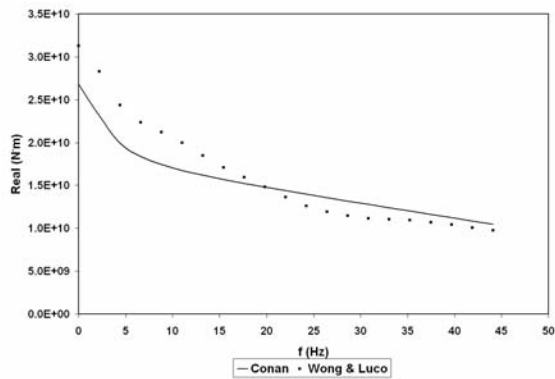


B

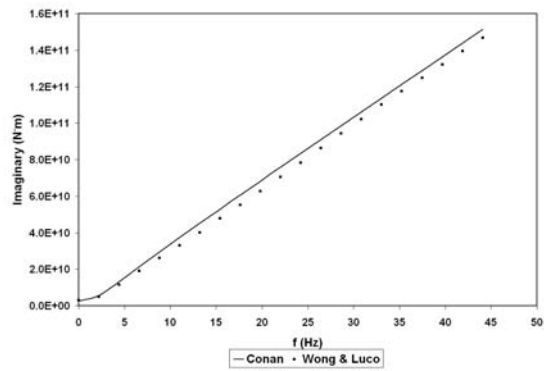


C

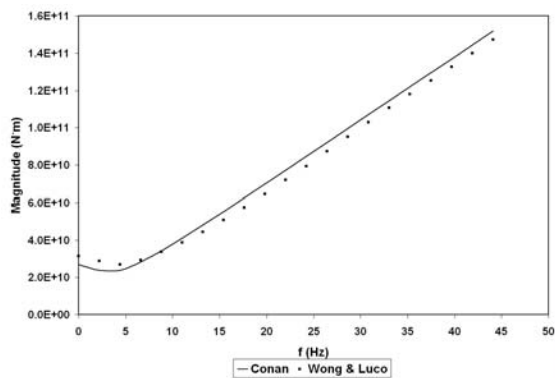
Figure 3-7. Horizontal Impedance Functions in Long Direction for Model 4 Length/Width=4, Wong and Luco (1978). A) Real. B) Imaginary. C) Magnitude.



A

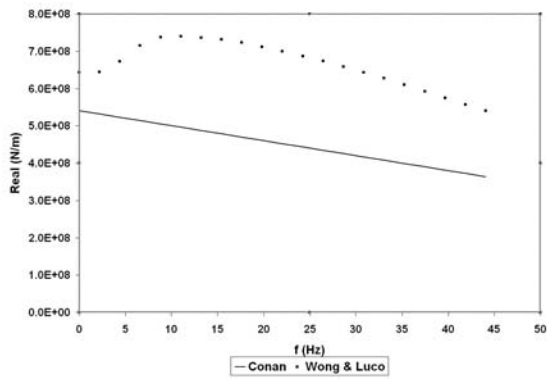


B

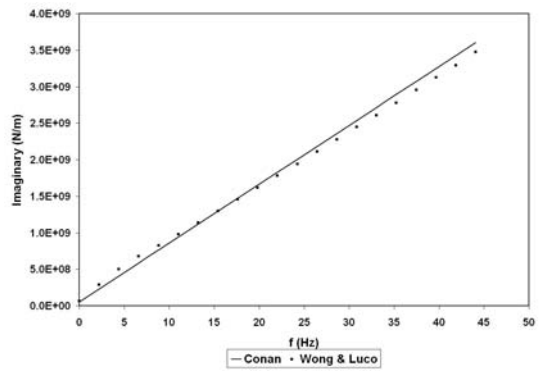


C

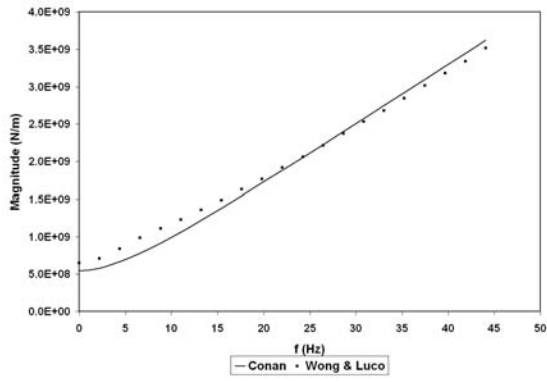
Figure 3-8. Rocking Impedance Functions About Short Axis. for Model 4 Length/Width=4, Wong and Luco (1978). A) Real. B) Imaginary. C) Magnitude.



A

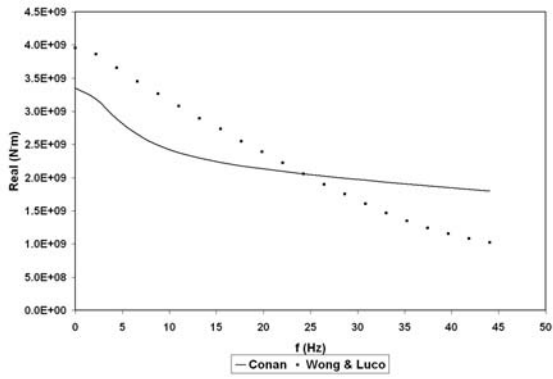


B

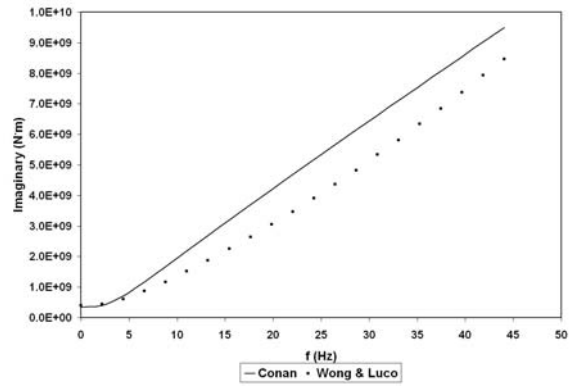


C

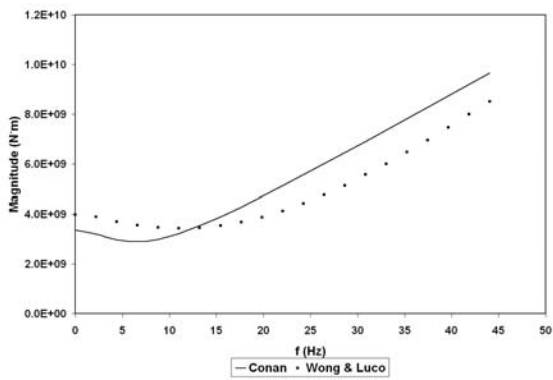
Figure 3-9. Horizontal Impedance Functions in Short Direction for Model 4 Length/Width=4, Wong and Luco (1978). A) Real. B) Imaginary. C) Magnitude.



A

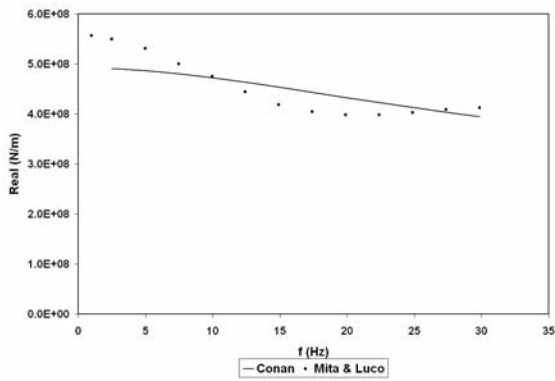


B

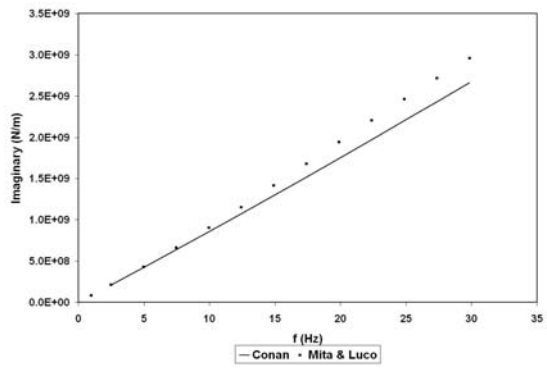


C

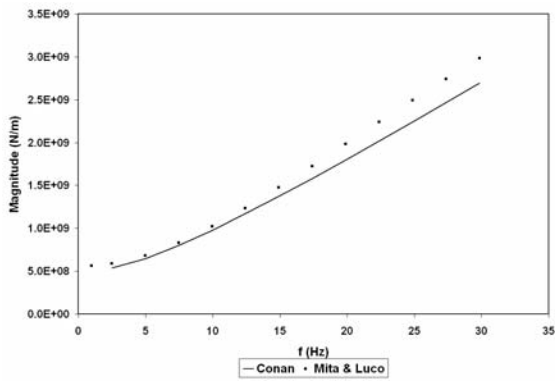
Figure 3-10. Rocking Impedance Functions About Long Axis for Model 4: Length/Width=4, Wong and Luco (1978). A) Real. B) Imaginary. C) Magnitude.



A

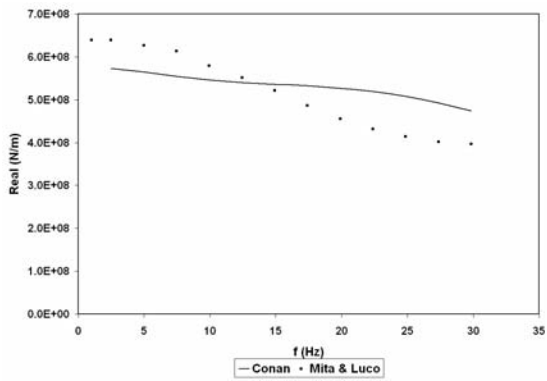


B

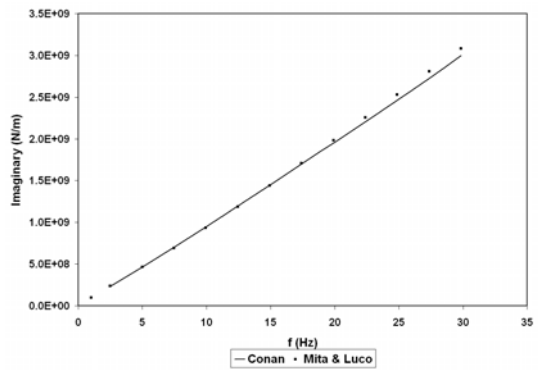


C

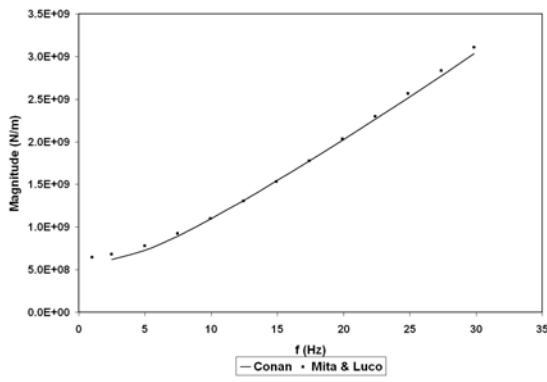
Figure 3-11. Vertical Impedance Functions for Model 3 Embedded, Mita and Luco (1989). A) Real. B) Imaginary. C) Magnitude.



A

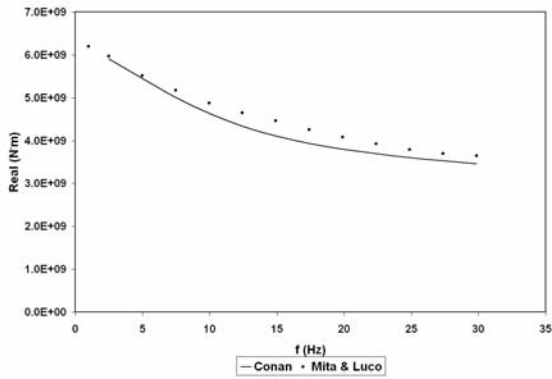


B

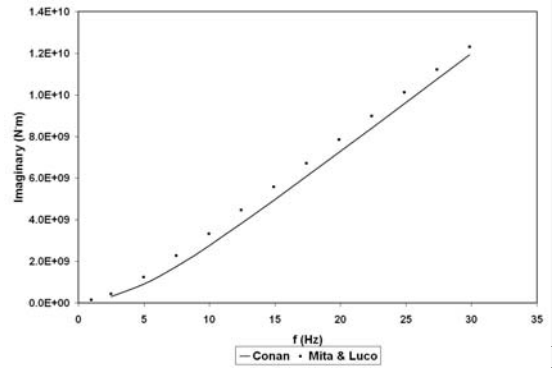


C

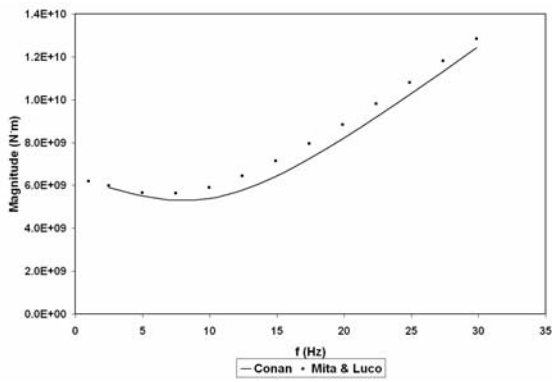
Figure 3-12. Horizontal Impedance Functions for Model 3 Embedded, Mita and Luco (1989). A) Real. B) Imaginary. C) Magnitude.



A

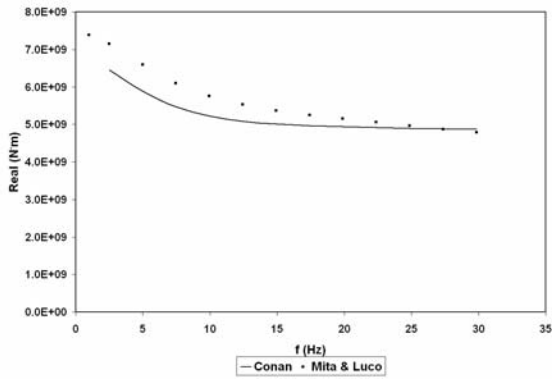


B

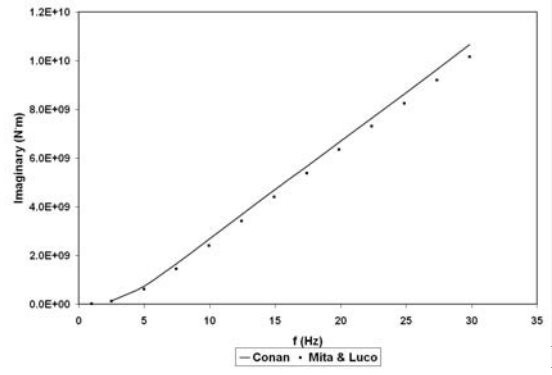


C

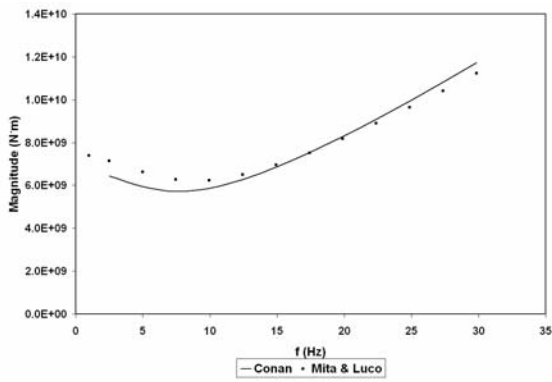
Figure 3-13. Rocking Impedance Functions for Model 3 Embedded, Mita and Luco (1989). A) Real. B) Imaginary. C) Magnitude.



A

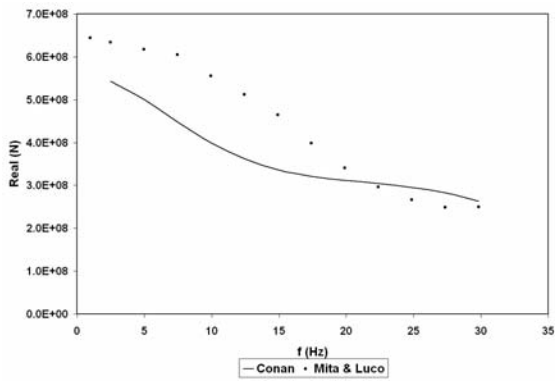


B

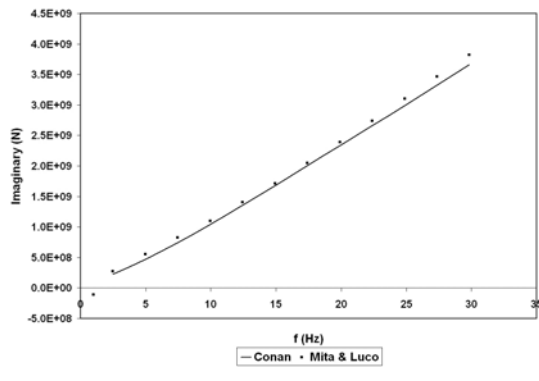


C

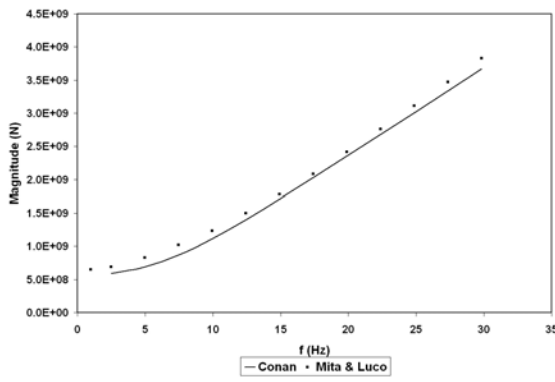
Figure 3-14. Torsional Impedance Functions for Model 3 Embedded, Mita and Luco (1989). A) Real. B) Imaginary. C) Magnitude.



A

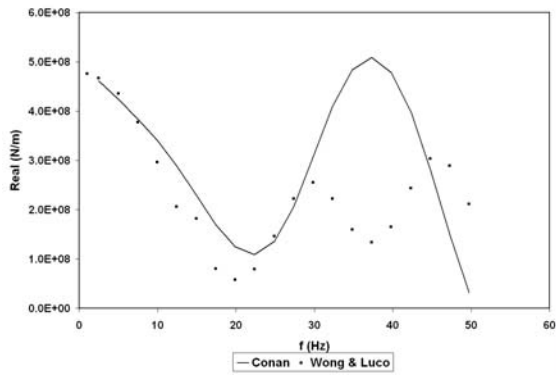


B

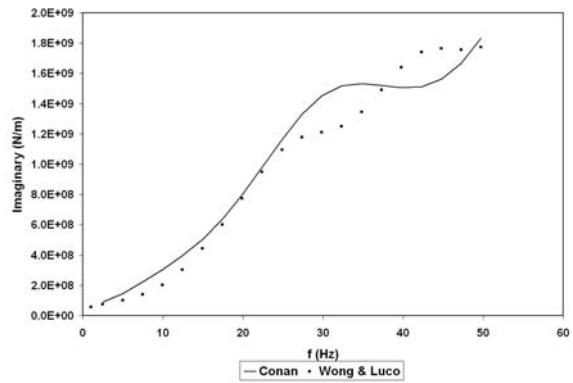


C

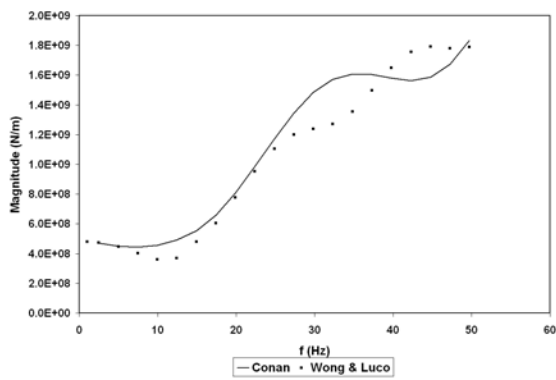
Figure 3-15. Coupled Impedance Functions for Model 3 Embedded, Mita and Luco (1989). A) Real. B) Imaginary. C) Magnitude.



A

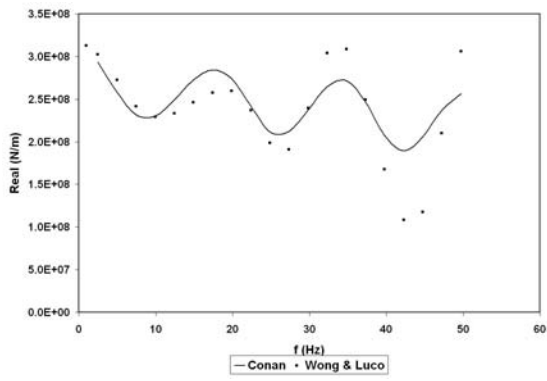


B

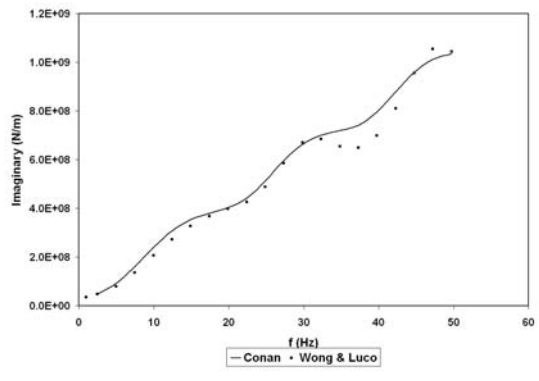


C

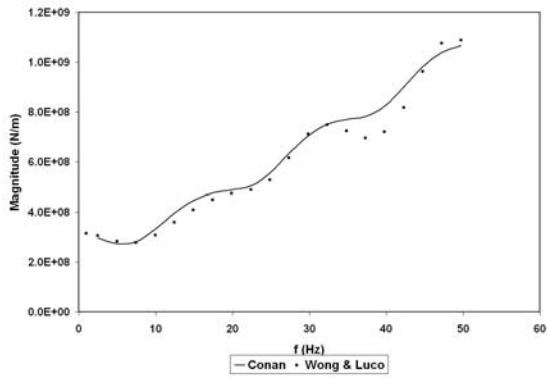
Figure 3-16. Vertical Impedance Functions for Model 1: Basis Model, Wong and Luco (1985).  
 A) Real. B) Imaginary. C) Magnitude.



A

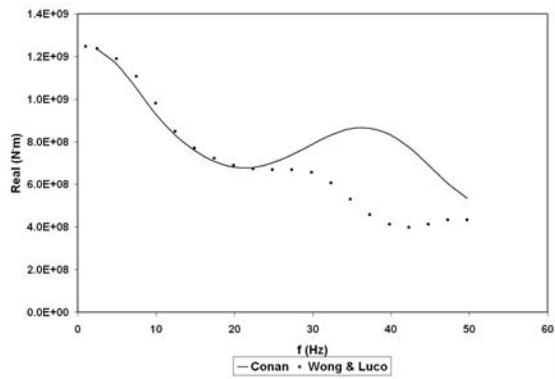


B

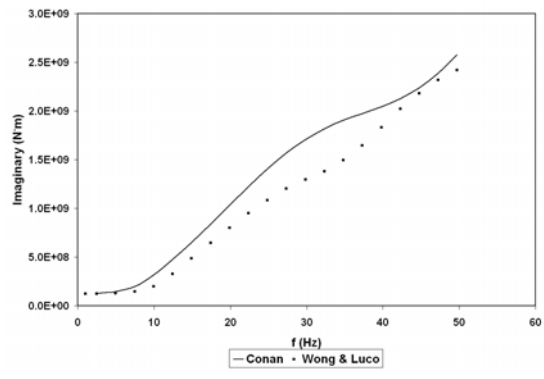


C

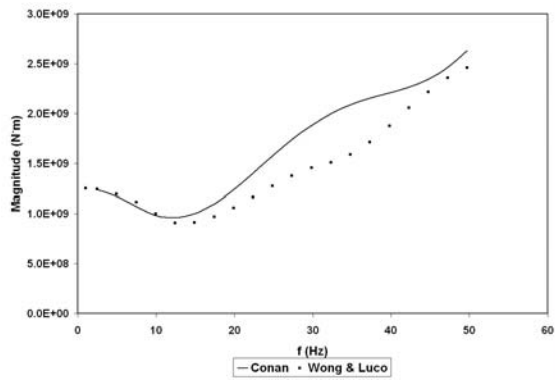
Figure 3-17. Horizontal Impedance Functions for Model 1: Basis Model, Wong and Luco (1985).  
 A) Real. B) Imaginary. C) Magnitude.



A

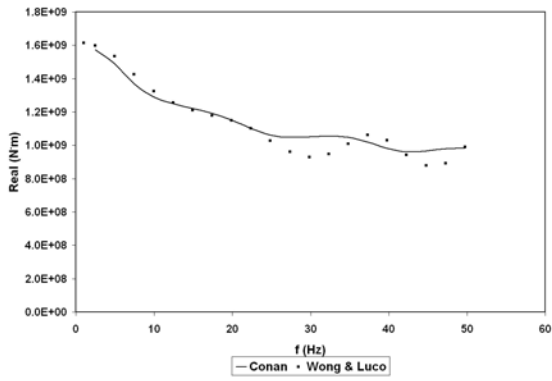


B

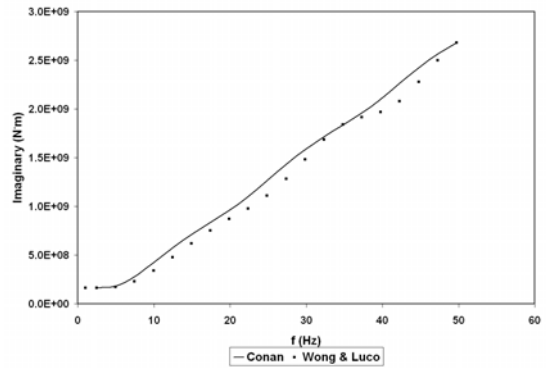


C

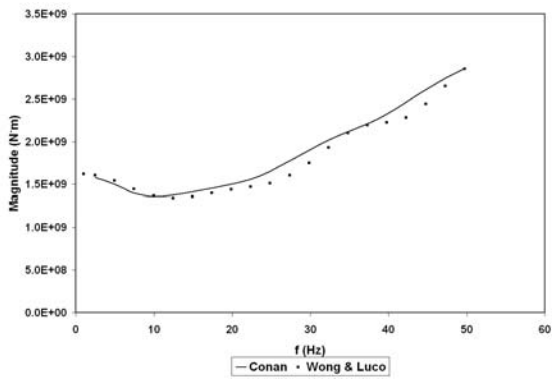
Figure 3-18. Rocking Impedance Functions for Model 1: Basis Model, Wong and Luco (1985).  
 A) Real. B) Imaginary. C) Magnitude.



A

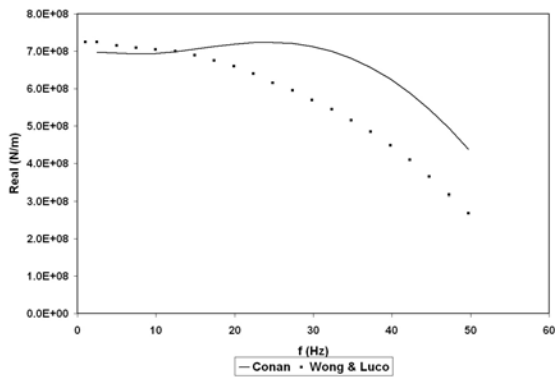


B

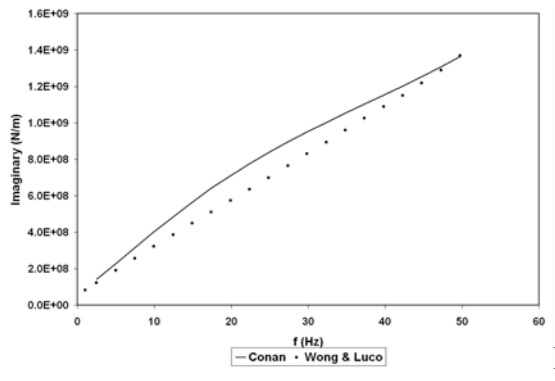


C

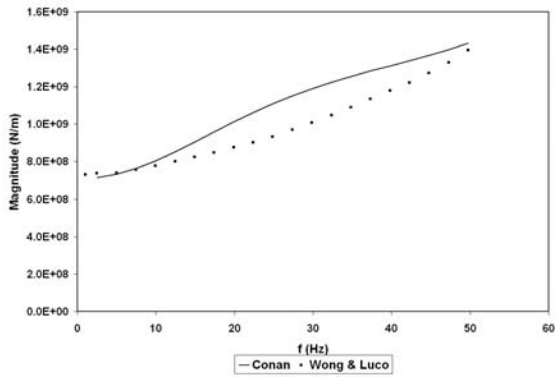
Figure 3-19. Torsional Impedance Functions for Model 1: Basis Model, Wong and Luco (1985).  
 A) Real. B) Imaginary. C) Magnitude.



A

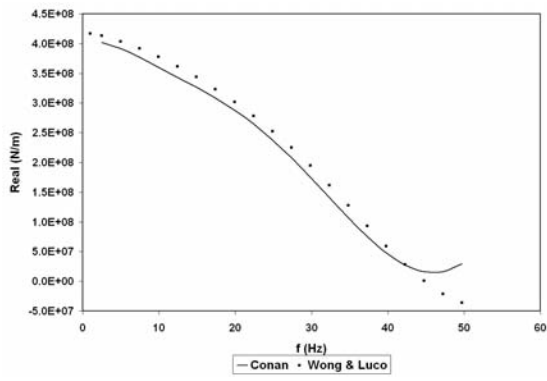


B

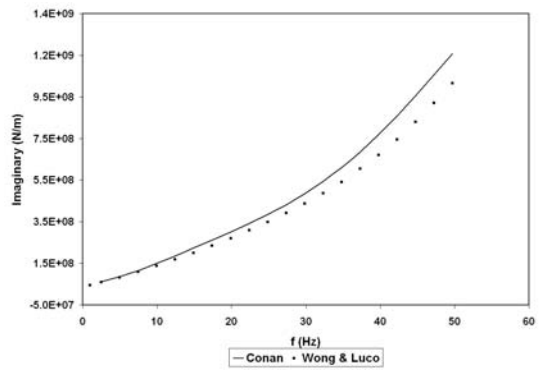


C

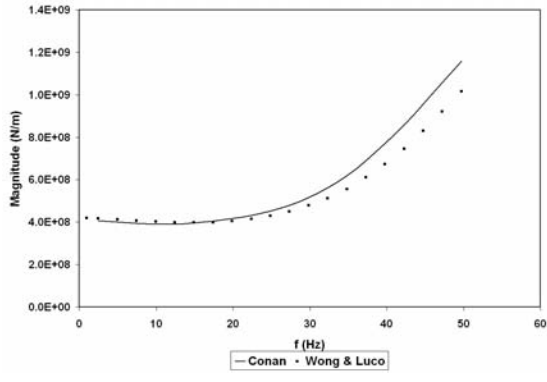
Figure 3-20. Vertical Impedance Functions for Model 4:  $\frac{1}{4}$  Layer Thickness, Wong and Luco (1985). A) Real. B) Imaginary. C) Magnitude.



A

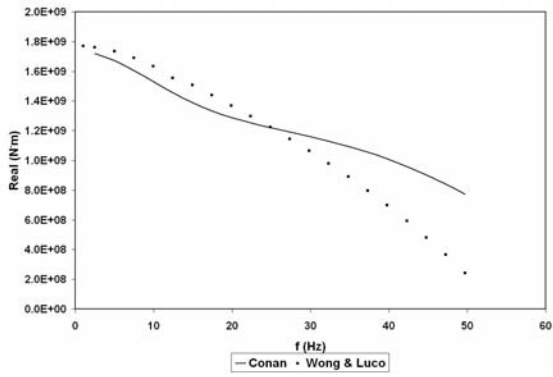


B

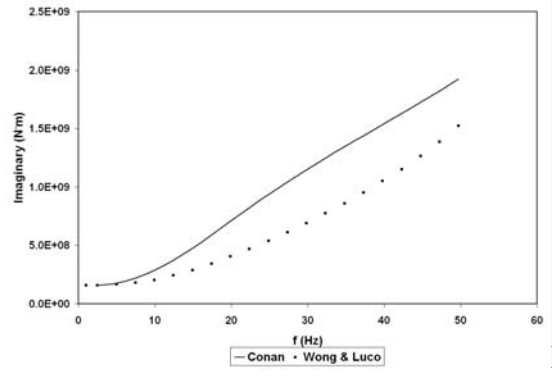


C

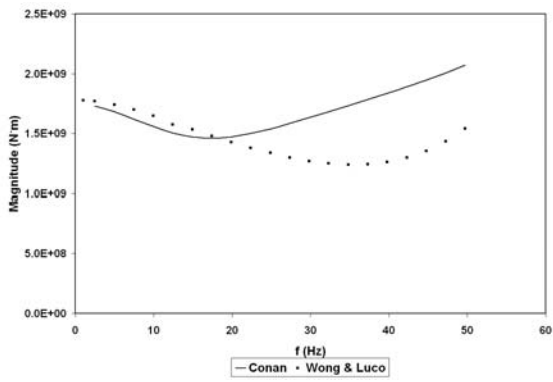
Figure 3-21. Horizontal Impedance Functions for Model 4:  $\frac{1}{4}$  Layer Thickness, Wong and Luco (1985). A) Real. B) Imaginary. C) Magnitude.



A

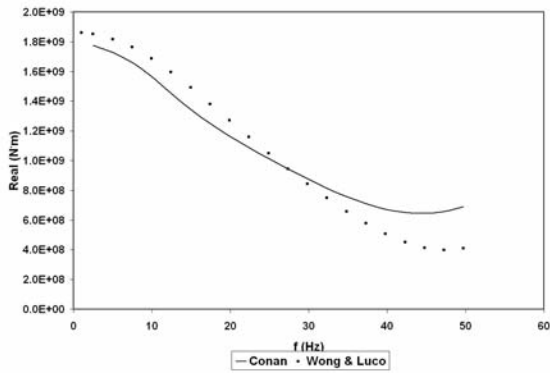


B

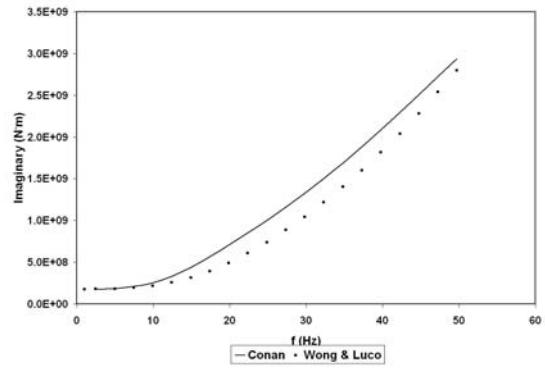


C

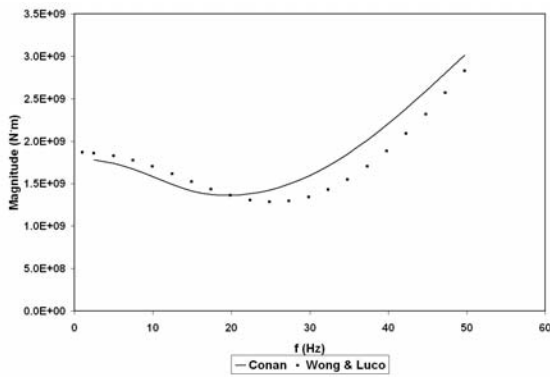
Figure 3-22. Rocking Impedance Functions for Model 4:  $\frac{1}{4}$  Layer Thickness, Wong and Luco (1985). A) Real. B) Imaginary. C) Magnitude.



A

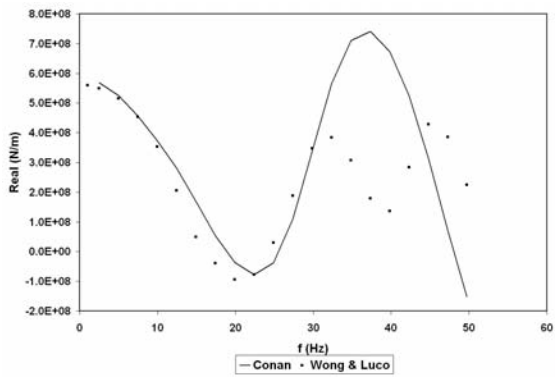


B

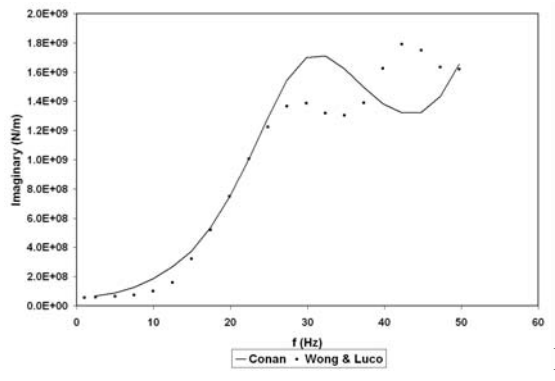


C

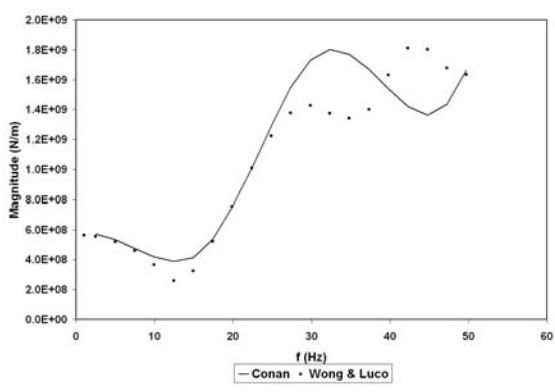
Figure 3-23. Torsional Impedance Functions for Model 4:  $\frac{1}{4}$  Layer Thickness, Wong and Luco (1985). A) Real. B) Imaginary. C) Magnitude.



A

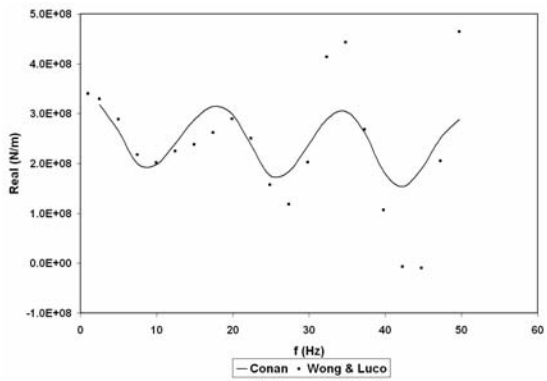


B

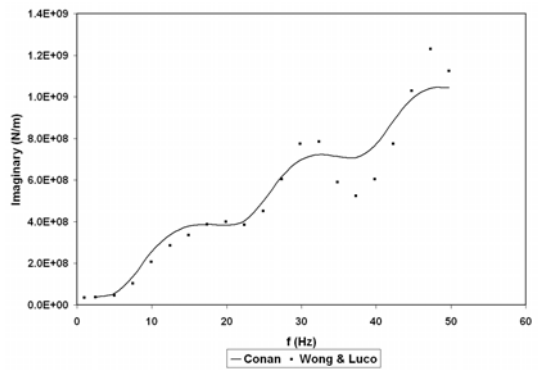


C

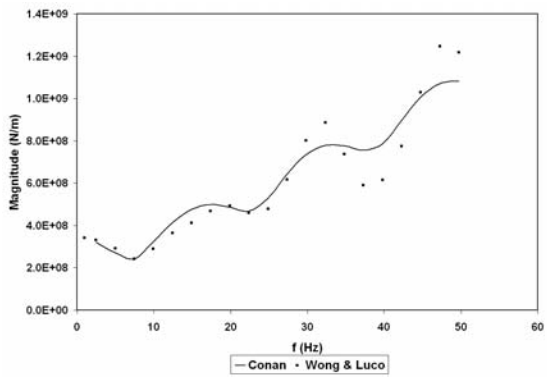
Figure 3-24. Vertical Impedance Functions for Model 6: Higher Vs Contrast, Wong and Luco (1985). A) Real. B) Imaginary. C) Magnitude.



A

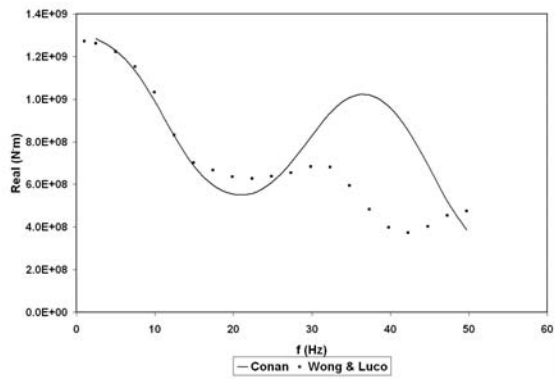


B

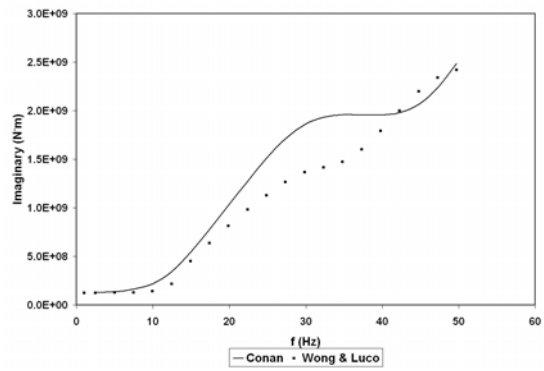


C

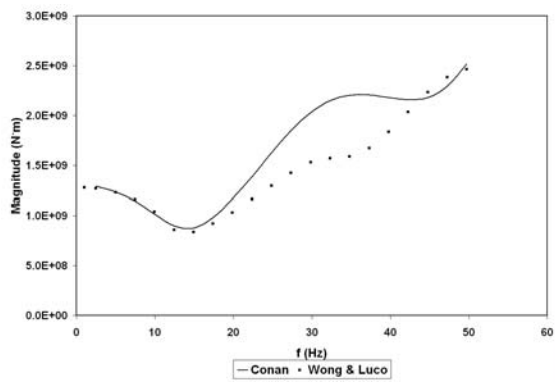
Figure 3-25. Horizontal Impedance Functions for Model 6: Higher Vs Contrast, Wong and Luco (1985). A) Real. B) Imaginary. C) Magnitude.



A

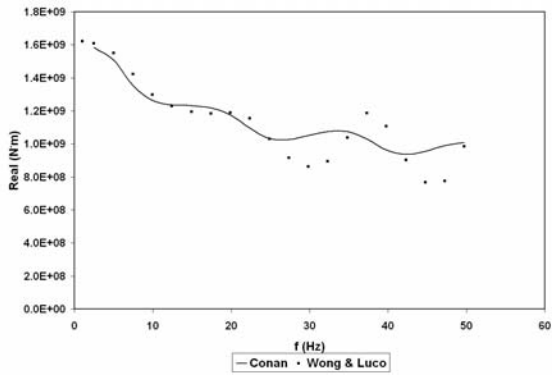


B

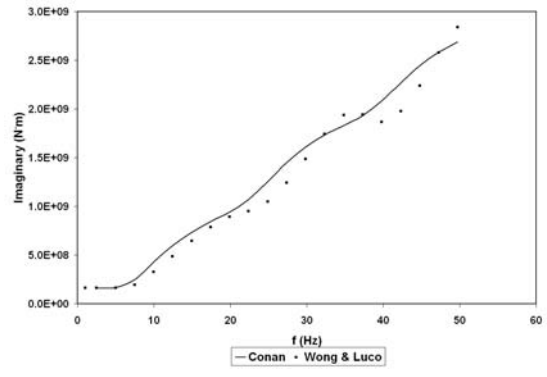


C

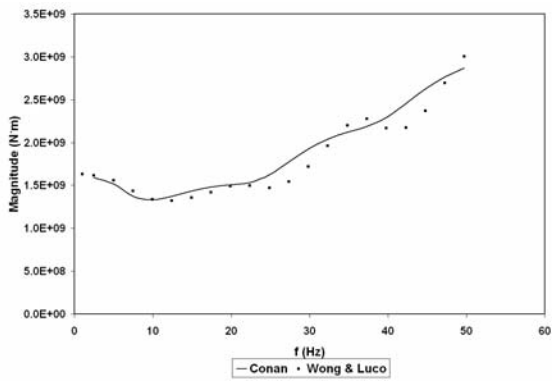
Figure 3-26. Rocking Impedance Functions for Model 6: Higher Vs Contrast, Wong and Luco (1985). A) Real. B) Imaginary. C) Magnitude.



A

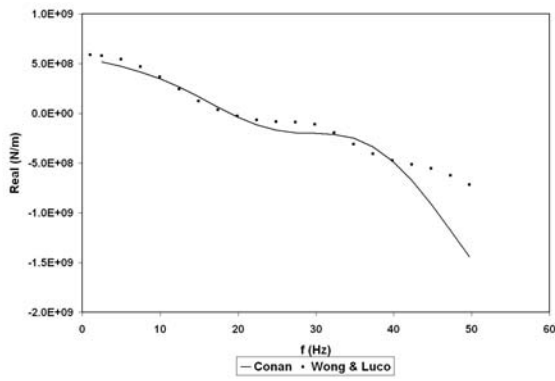


B

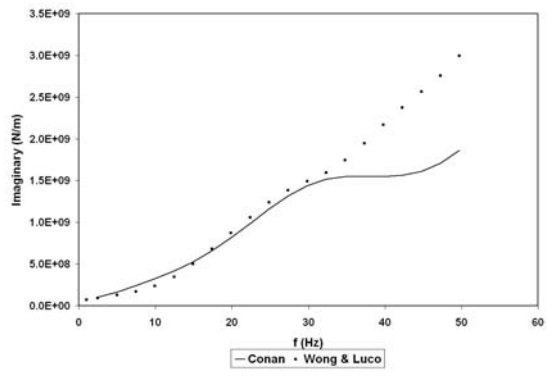


C

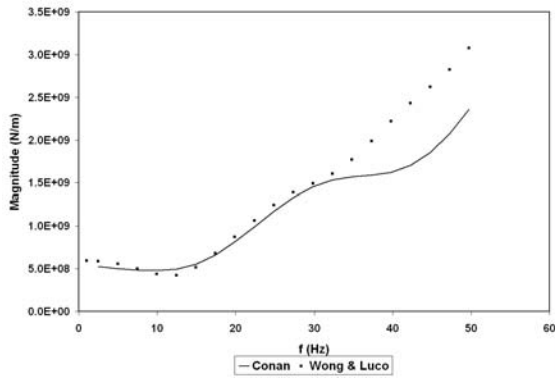
Figure 3-27. Torsional Impedance Functions for Model 6: Higher Vs Contrast, Wong and Luco (1985). A) Real. B) Imaginary. C) Magnitude.



A

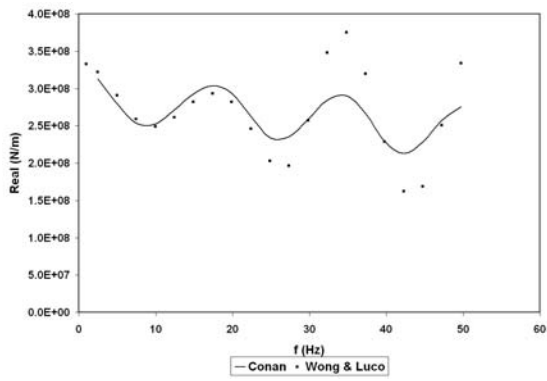


B

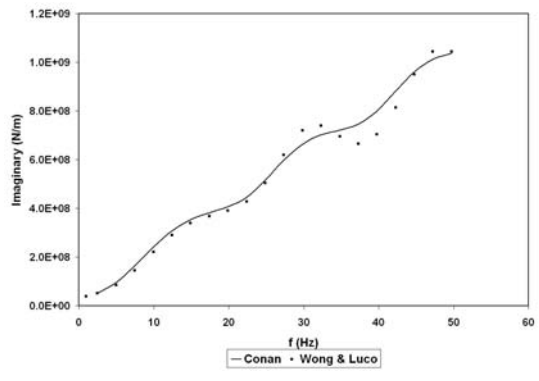


C

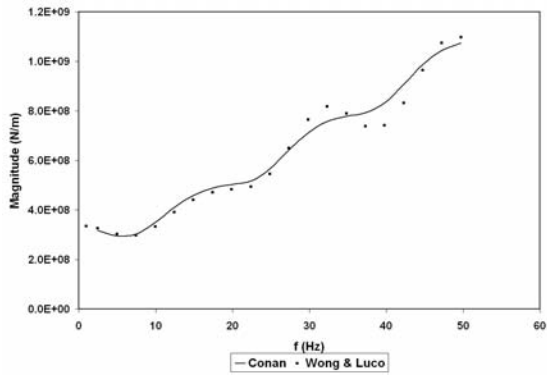
Figure 3-28. Vertical Impedance Functions for Model 8: Poisson's Ratio=0.45, Wong and Luco (1985). A) Real. B) Imaginary. C) Magnitude.



A

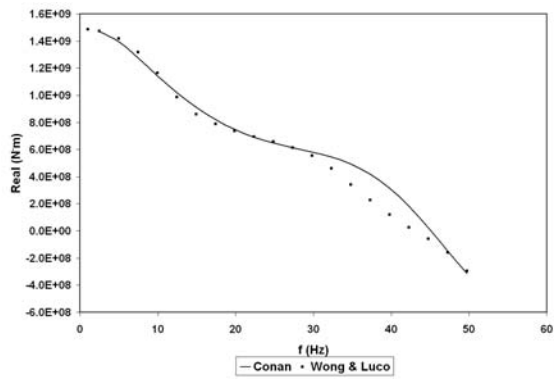


B

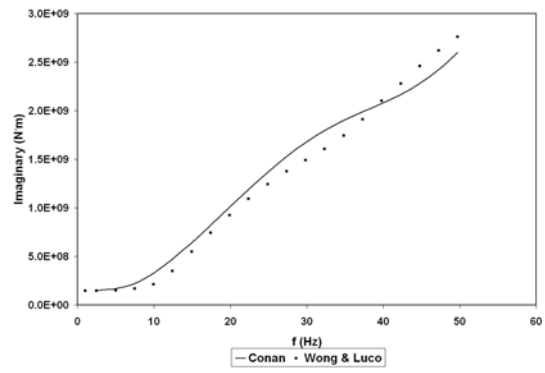


C

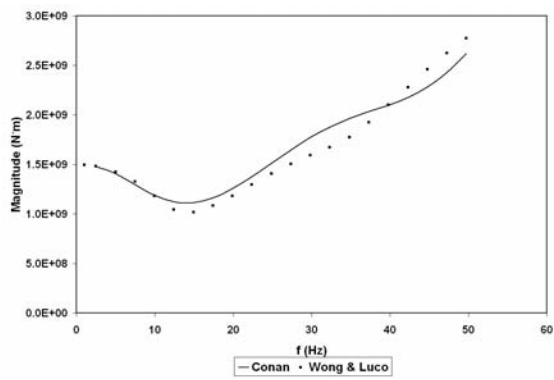
Figure 3-29. Horizontal Impedance Functions for Model 8: Poisson's Ratio=0.45, Wong and Luco (1985). A) Real. B) Imaginary. C) Magnitude.



A

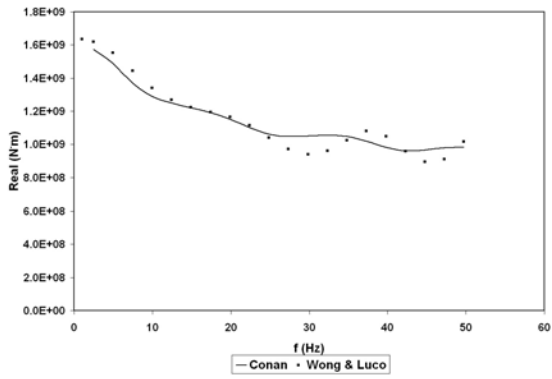


B

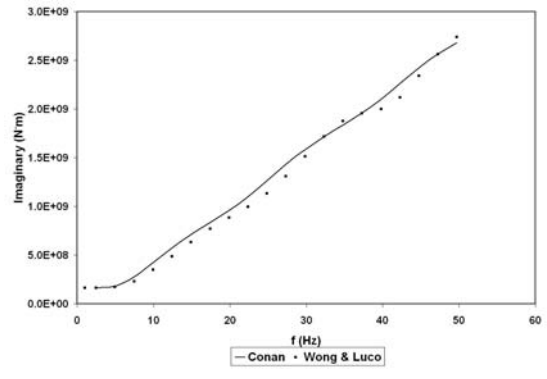


C

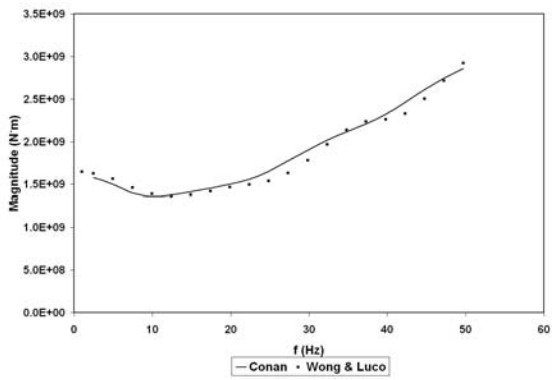
Figure 3-30. Rocking Impedance Functions for Model 8: Poisson's Ratio=0.45, Wong and Luco (1985). A) Real. B) Imaginary. C) Magnitude.



A

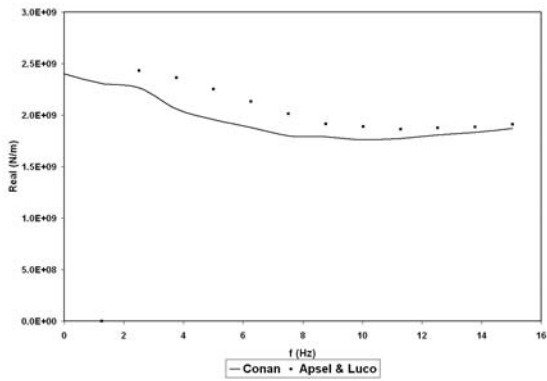


B

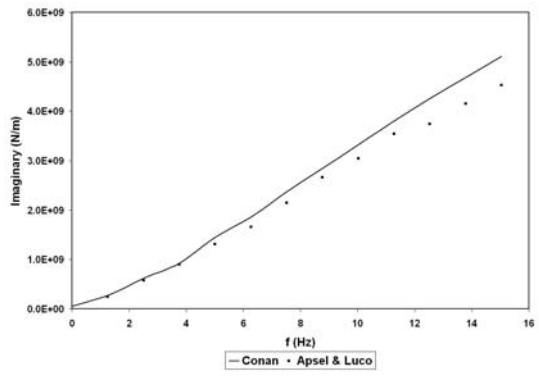


C

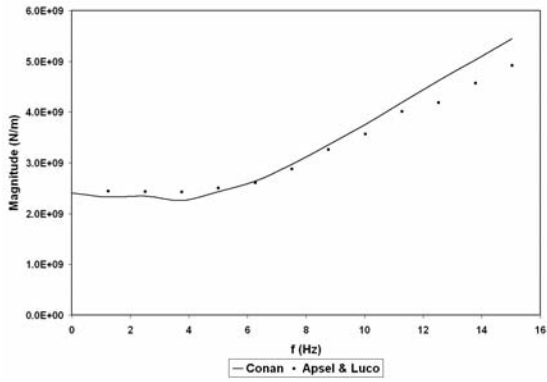
Figure 3-31. Torsional Impedance Functions for Model 8: Poisson's Ratio=0.45, Wong and Luco (1985). A) Real. B) Imaginary. C) Magnitude.



A

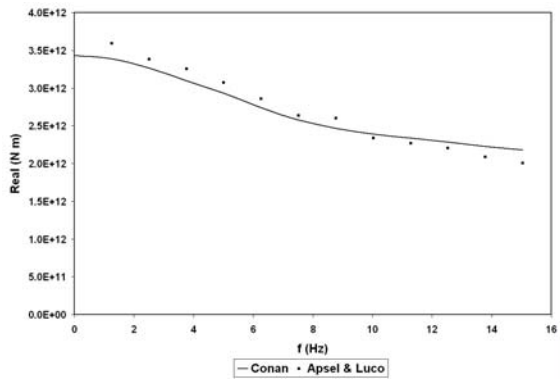


B

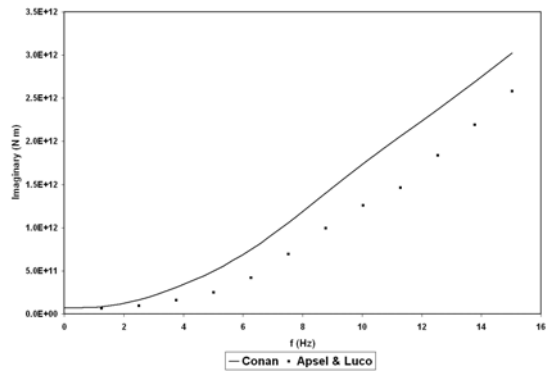


C

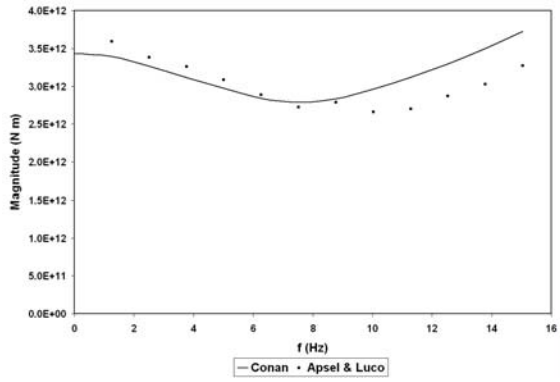
Figure 3-32. Horizontal Impedance Functions for Layered Model, ApseI and Luco (1987). A) Real. B) Imaginary. C) Magnitude.



A

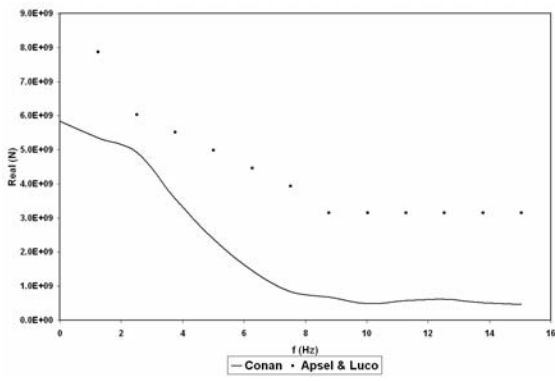


B

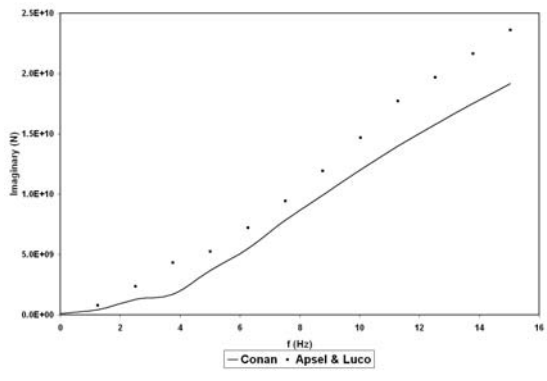


C

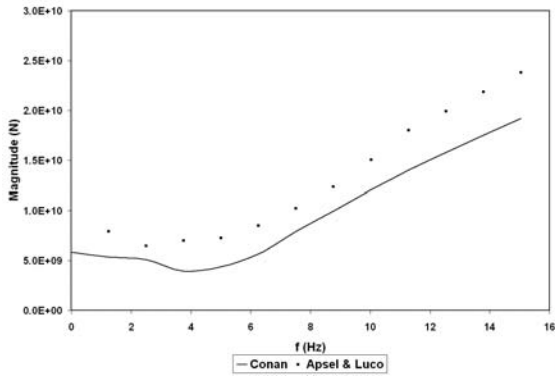
Figure 3-33. Rocking Impedance Functions for Layered Model, Apse and Luco (1987). A) Real. B) Imaginary. C) Magnitude.



A

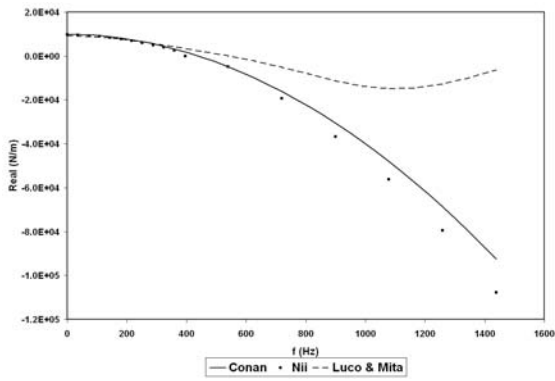


B

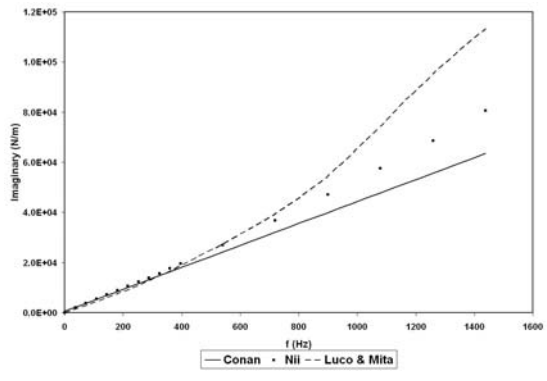


C

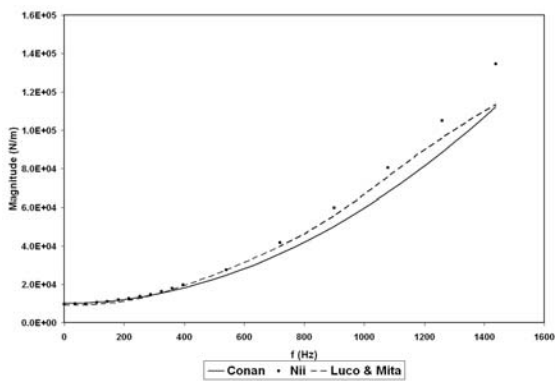
Figure 3-34. Coupled Impedance Functions for Layered Model, Apse and Luco (1987). A) Real. B) Imaginary. C) Magnitude.



A

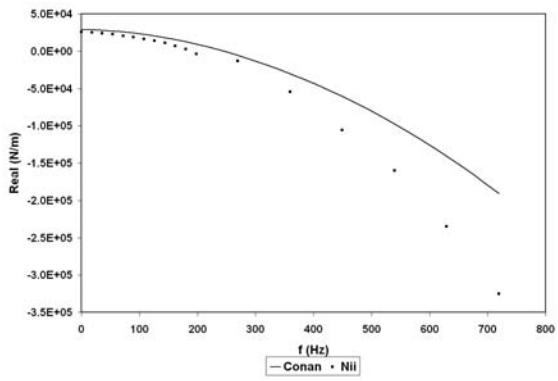


B

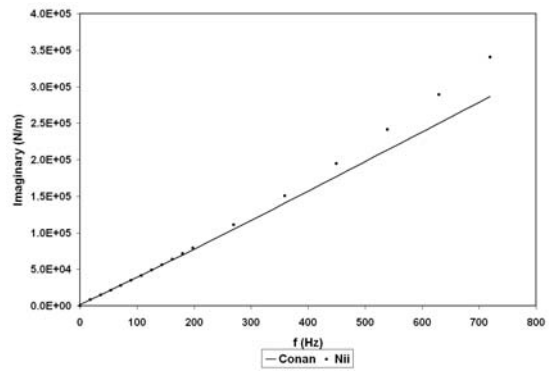


C

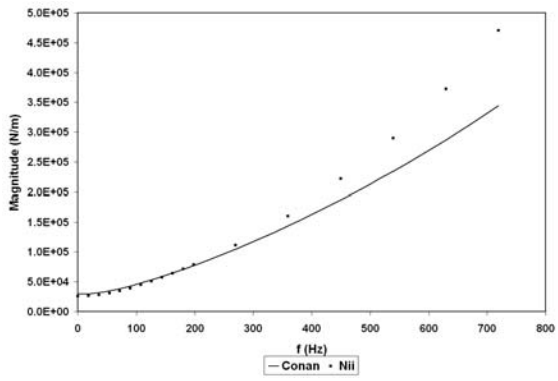
Figure 3-35. Vertical Impedance Functions for Circular, Surface Model Footing, Nii (1987). A). Real. B) Imaginary. C) Magnitude.



A

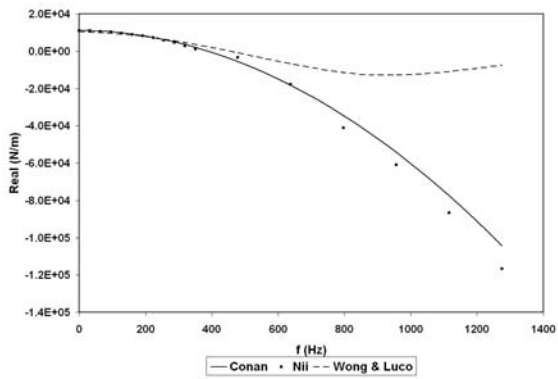


B

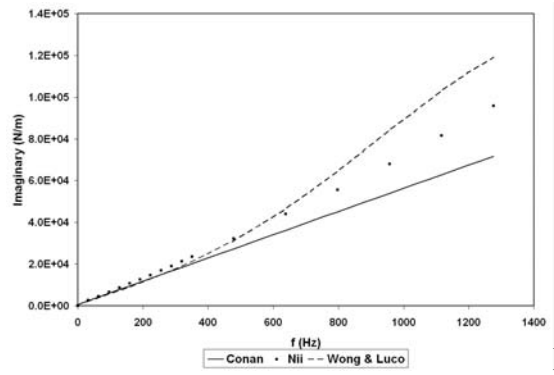


C

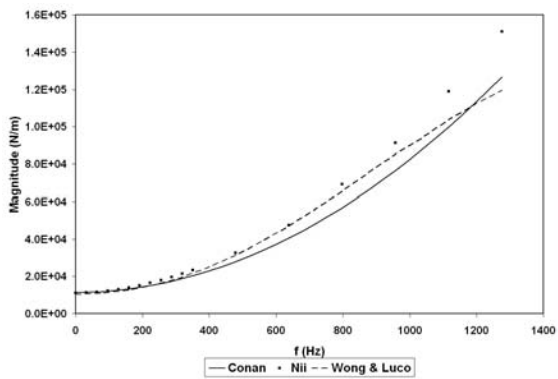
Figure 3-36. Vertical Impedance Functions for Circular, Fully Embedded Model Footing, Nii (1987). A). Real. B) Imaginary. C) Magnitude.



A

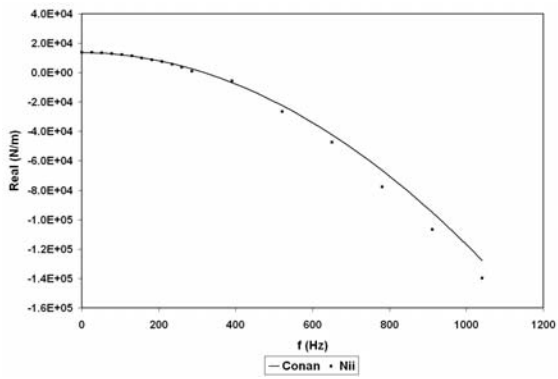


B

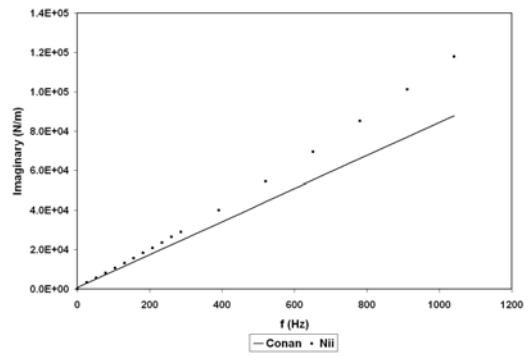


C

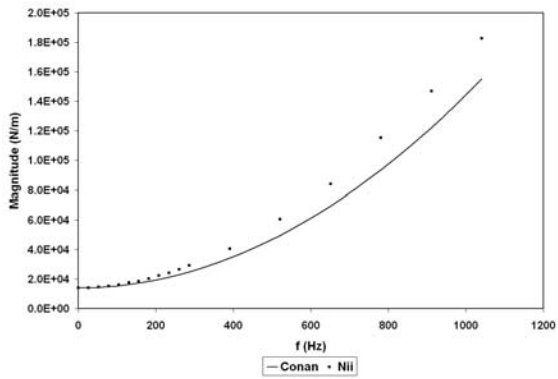
Figure 3-37. Vertical Impedance Functions for Rectangular, Surface,  $L/W=1$  Model Footing, Nii (1987). A). Real. B) Imaginary. C) Magnitude.



A

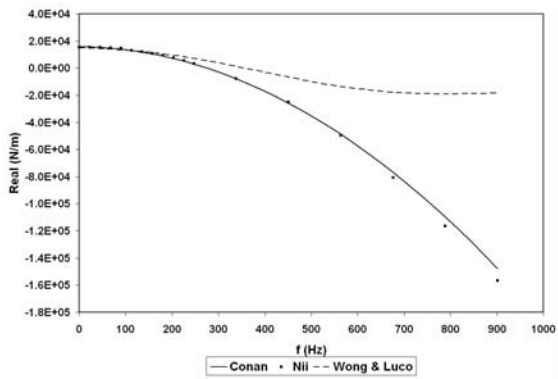


B

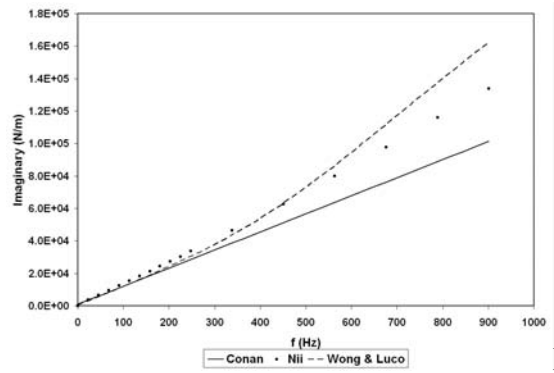


C

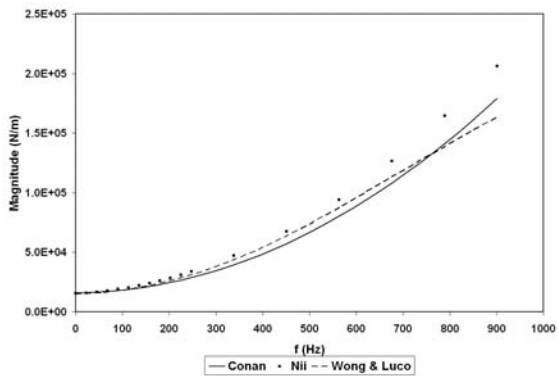
Figure 3-38. Vertical Impedance Functions for Rectangular, Surface,  $L/W=1.5$  Model Footing, Nii (1987). A) Real. B) Imaginary. C) Magnitude.



A

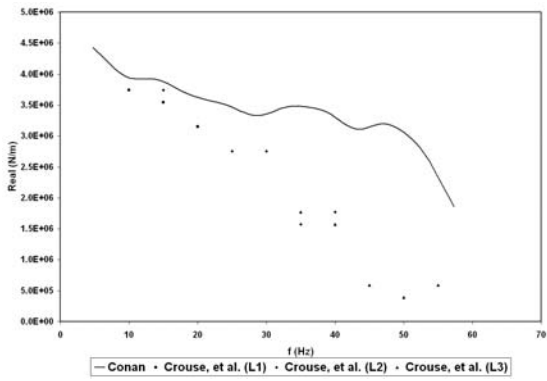


B

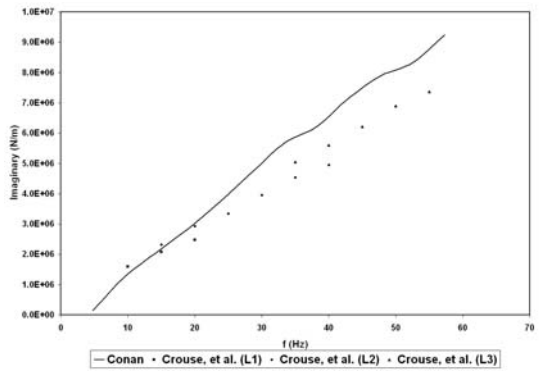


C

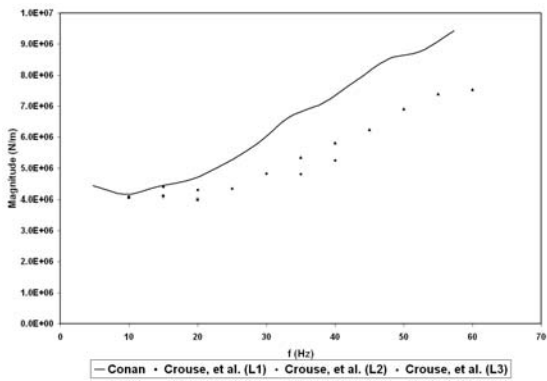
Figure 3-39. Vertical Impedance Functions for Surface,  $L/W=2$  Model Footing, Nii (1987). A). Real. B) Imaginary. C) Magnitude.



A

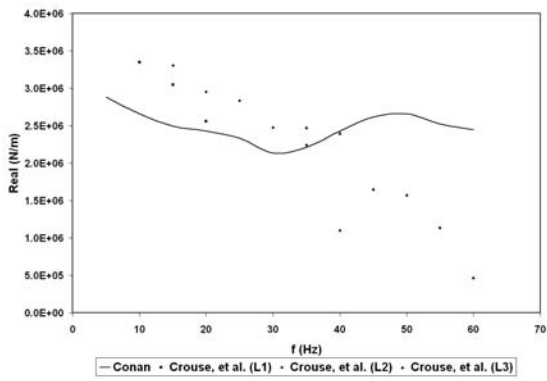


B

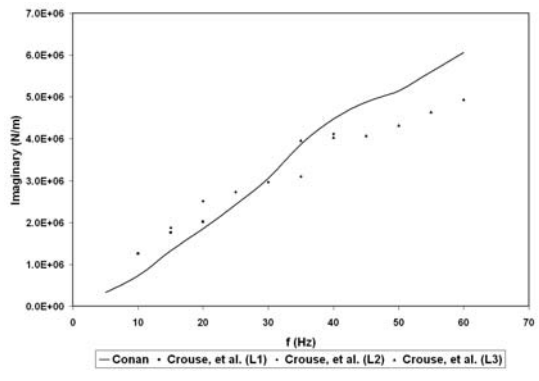


C

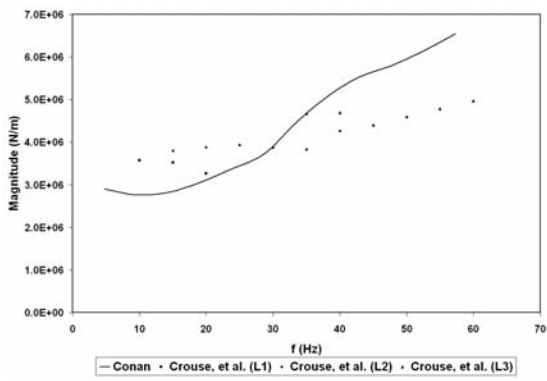
Figure 3-40. Vertical Impedance Functions for Station 6, Crouse, et al. (1990). A) Real. B) Imaginary. C) Magnitude.



A

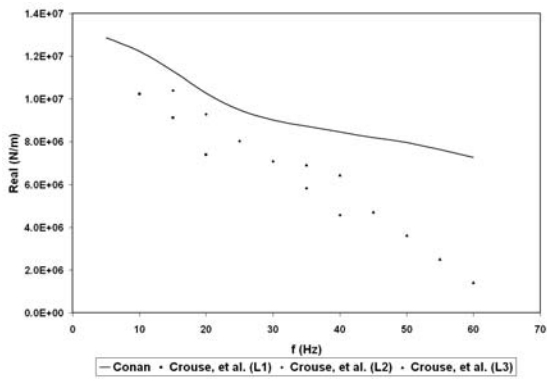


B

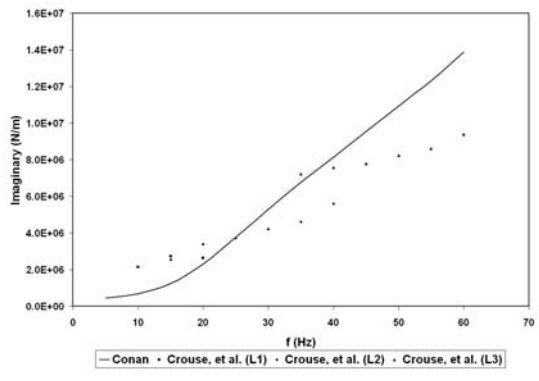


C

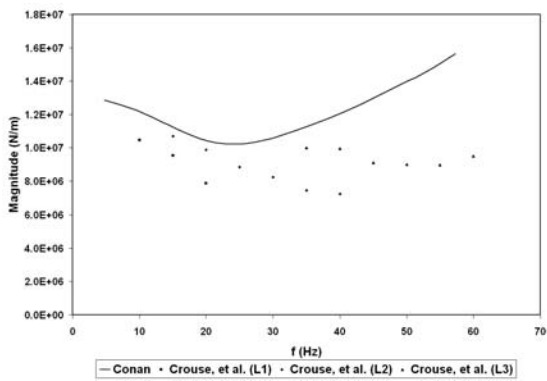
Figure 3-41. Horizontal Impedance Functions for Station 6, Crouse, et al. (1990). A) Real. B) Imaginary. C) Magnitude.



A



B



C

Figure 3-42. Rocking Impedance Functions for Station 6, Crouse, et al. (1990). A) Real. B) Imaginary. C) Magnitude.

## CHAPTER 4 SITE CHARACTERIZATION

Two shallow foundations, the first 1 m x 1m in plan and embedded 0.9 m, and the second 3 m x 3 m in plan and embedded 0.9 m, have been dynamically loaded at the National Geotechnical Experiment Site (NGES) on the campus of Texas A&M University (TAMU). Foundation responses were recorded in order to determine measured values for impedance functions. This chapter presents a description of the site, foundations, and equipment used to perform tests and also supplies necessary information for calculating impedance functions.

### **4.1 Site Investigation**

The TAMU NGES site has been extensively characterized via both in situ and laboratory soil testing techniques, including shear wave velocity via both borehole and surface wave methods. The site consists of an upper layer of approximately 10 m of medium dense, silty, fine sand followed by hard clay. The water table is approximately 5 m below the ground surface. A more detailed description of site conditions is presented in the following paragraphs.

#### **4.1.1 Traditional Investigation**

The NGES site was investigated by both traditional and seismic geotechnical methods. Traditional methods are outlined in the proceedings of Briaud and Gibbens (1994). Of particular interest is the soil's profile which consists of a layer (Layer 1) of tan medium dense silty fine sand from existing grade to approximately two m. Directly beneath the first layer is a tan medium dense silty sand with clay (Layer 2) to approximately 10.5 m below grade. The water table is encountered in the second layer at an approximate depth of five m. Below the second layer is a dark gray very hard clay (Layer 3) extending to the bottom of the borings all of which terminate 15.2 m below grade.

Values for unit weights of each layer were either identified in Briaud and Gibbens (1994) or calculated from information available in the proceedings. For layers one and two they give values of unit weight above the water table as  $15.28 \text{ KN/m}^2$  and  $15.65 \text{ KN/m}^2$  respectively. Below the water table, values were calculated based on saturation and void ratio of  $19.11 \text{ KN/m}^2$ . Properties of the clay were assumed based on boring log descriptions due to the lack of tests performed on the clay in the proceedings. Prior to the construction of foundations, between approximately 0.5 m and 1.5 m of overburden was removed from the site.

Many additional studies were conducted. Field tests such as standard penetration tests (SPT) and cone penetration tests (CPT) were performed along with others. Laboratory tests were also conducted such as triaxial tests and those used to calculate the information above. Results for all tests can be found in Briaud and Gibbens (1994).

#### **4.1.2 Seismic Investigation**

Seismic tests of the NGES site were performed. Briaud and Gibbens (1994) present data for crosshole seismic testing to a depth of ten meters. Testing did not include the clay layer which starts at 10.5 m thus did not allow adequate seismic characterization of the layer. An accurate model below ten meters would not be possible without further seismic testing to characterize the clay layer. Horizontal crosshole rays were initiated at a depth of two meters. Depths for each subsequent ray were increased at two meter intervals which provided a general idea of subsurface conditions but, these intervals were not sufficient to produce the accuracy desired for the seismic modeling of the soil. Boreholes used for the test were measured by an inclinometer to determine a precise distance between crosshole equipment at each depth. Resonant column tests were also performed on samples from the site and are available in Briaud and Gibbens (1994).

A second set of crosshole seismic tests were performed in March of 2007 to enhance the available velocity profile and extend the velocity profile into the clay layer. The results of these additional tests are displayed in Figure 4-1. Horizontal rays were measured in the same boreholes used for the first tests and another inclinometer survey was performed to accurately calculate the distance between crosshole equipment at each depth. The second set of crosshole tests differed from the first in depth and increment. The holes were surveyed to a depth of 14.6 m which was 4.6 m deeper than the initial test and 4.1 m into the clay.

Tran and Hiltunen (2008) outline three seismic surface wave surveys conducted at the site in October of 2006. SASW, MASW, and passive MASW surveys were able to provide shear wave data for both footings. This was accomplished by laying out a single survey line that all surface wave tests were conducted along. The survey line was placed in close proximity to both footings assuring the most effective representation of the subsurface with regards to shear modulus.

A detailed account of the methodology of all three techniques along with a comprehensive report of test procedures is given in Tran and Hiltunen (2008). Of most importance is the general agreement of all four tests indicating that the tests were performed well thereby bolstering confidence in shear wave velocities used in impedance function prediction calculations.

Traditional investigation data such as the borehole log and SPT values also seem to agree with seismic methods. Similarities noted by Tran and Hiltunen (2008) between two somewhat different approaches to measuring soil strength further suggest that results provided by seismic analysis are reliable and appropriate for use in impedance function calculations.

## **4.2 Foundation Selection and Construction**

Field testing required certain characteristics for a footing to be acceptable. Acceptable characteristics were those found in typical construction practices such as scale. There is no

specific guideline for such a footing so some estimation was required pertaining to what is common. Embedded footings were necessary as a surface footing would have neglected the study of coupling impedances. Additionally, the footing had to essentially behave as a rigid body under dynamic loading conditions.

The NGES site was selected for its previously conducted site investigations and foundations that were constructed for previous research. The intention was to minimize time, cost and effort by utilizing available resources. Generally these intentions were realized. Soil data was readily available though some additional tests were required to expand it. In the case of existing footings, a visual inspection of the site revealed that many of the footings described in Briaud and Gibbons (1994) were unsuitable due to severe cracking. Of the footings that were considered for testing, only one, previously named Footing 5, remained in tact, Figure 4-2. That footing was a small unreinforced 0.9 m by 0.9 m by 1.2 m solid concrete footing embedded 0.7 m. Its center was approximately 3 m from the seismic surface wave survey line making its location convenient for impedance function predictions.

A larger footing was desired for shaking. Unfortunately prior testing had damaged any other acceptable footings at the site. The decision to construct a larger footing was made. An arbitrary design was decided upon that was approximately 3 m by 3 m by 1 m and fully embedded, Figure 4-3. The design is fully reinforced with # 6 reinforcing steel every 5 in, Figure 4-4, concrete block of 4,000 psi concrete which avoids failure of the foundation during testing and assures rigid behavior. A contractor was contacted that was capable of assisting with a design. The footing, deemed Footing 6, was constructed with the east edge 6 m from the seismic surface wave survey line. Though not as close as Footing 5, Footing 6 was adequately positioned to make use of the SASW survey line.

Both footings were to be tested in the vertical direction with shakers resting on their surfaces. After vertical tests were concluded, shakers were to test in the horizontal direction requiring anchor bolts to be sunk in order to fasten the shakers to the footings. These anchor bolts were also to be used to attach frames for additional shaker configurations. In the case of Footing 6 multiple anchoring positions were to be created.

### **4.3 Shakers**

Four dynamic loading devices implemented in several configurations have been used to excite each footing in vertical, horizontal sliding, and rocking vibration modes. The four devices are listed as follows: 1) an APS Model 400 Electro Seis presented in Figure 4-2 capable of applying a constant maximum load amplitude of 70 lb over a frequency range from 1 to 100 Hz, 2) an ANCO Model MK-12 rotating mass vibrator presented in Figure 4-5 with a maximum applied load of 10,000 lb, and a frequency range from 0 to 100 Hz, 3) the NSF NEES “Thumper” mobile shaker presented in Figure 4-6 operated by the University of Texas (Stokoe, et al.), and 4) the NSF NEES “T-Rex” mobile shaker presented in Figure 4-7 operated by the University of Texas (Stokoe, et al.). The “Thumper” and “T-Rex” shakers were used to apply vertical loads to the footings, while the APS and ANCO devices were configured to conduct independent experiments in both the vertical and horizontal directions. In addition, the APS and ANCO shakers configured in horizontal mode were mounted directly on the footings, and in an elevated position via an attached frame in order to accentuate the rocking mode of vibration, and to provide a second means to excite the coupled horizontal sliding and rocking modes by at least two independent means as described above.

The complete experimental program produced impedance functions for the vertical, horizontal sliding, rocking, and coupled sliding/rocking vibration modes and for each of the two embedded foundations. For some vibration modes, independent experiments were conducted

using more than one of the available vibration shakers. Results for these experiments are presented in the following chapter.

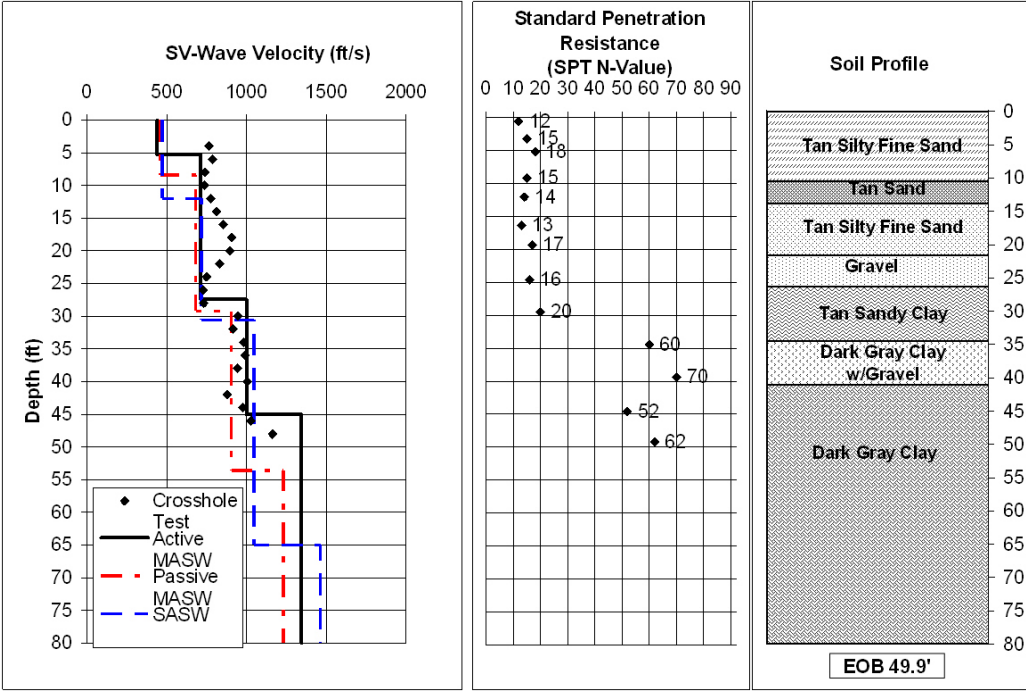


Figure 4-1. Seismic, SPT, and profile Tran and Hiltunen [2008]



Figure 4-2. Footing 5



Figure 4-3. Footing 6



Figure 4-4. Reinforcement of Footing 6



Figure 4-5. ANCO Model MK-12



Figure 4-6. NSF NEES "Thumper" mobile shaker



Figure 4-7. NSF NEES “T-Rex” mobile shaker

## CHAPTER 5 MEASURED IMPEDANCE FUNCTIONS

Dynamic loads were applied to foundations to determine dynamic impedance functions as presented in Chapter 4. Two shallow foundations were chosen for this investigation and four dynamic load devices were available. The specific experiments are described in the following paragraphs from which dynamic impedance functions were determined herein in accordance with the calculations of Chapter 2.

### 5.1 Footing 5

#### 5.1.1 Vertical Loading

Figure 5-1 presents an experiment for the vertical loading of Footing 5 using an ANCO Model MK-12 rotating mass shaker mounted flush to the footing surface. The shaker was configured to load in the vertical direction. The magnitude of the load was determined by the speed and eccentricity settings of the rotating masses. The photograph also displays the velocity transducers deployed at each of the four corners of the footing surface for measurement of the footing response to load.

Figure 5-2 presents measurements of foundation load and vertical displacement. Figure 5-2a displays continuously increasing amplitude of vertical load as frequency increases, which is characteristic behavior for a rotating-mass-type shaker. The resulting vertical displacement response of the foundation is displayed in Figures 5-2b and 5-2c. The complex number (real and imaginary) format implicitly contains both the amplitude of the sinusoidal displacement response, as well as the phase lag of the displacement from the applied sinusoidal loading. In operation, the loading was conducted in a steady-state mode wherein several cycles of load were applied at a constant frequency, beginning at the lowest frequency. The dynamic response of the foundation was measured simultaneously via the velocity transducers, and recorded via a

dynamic signal analyzer capable of characterizing the signals in complex number format. The displacement response was determined by integration of the velocity transducer measurements, and the loading was repeated at small increments of frequency through the frequency range noted in Figures 5-2b and 5-2c. Finally, it is noted that the real and imaginary components of the displacement responses are displayed for each of the four corners of the foundation. The four responses are indeed very similar, which in part indicates that the foundation is moving vertically in a rigid-body-like fashion. The average foundation displacement is calculated from the response of all the footing corners, which in turn is used to calculate the impedance relationship.

Figure 5-3 presents the real and imaginary components of the dynamic impedance function computed from the vertical load, response measurements, and the foundation characteristics as outlined in Equation 2-6. Vertical force was calculated in accordance with Equation 2-7.

### **5.1.2 Horizontal Loading**

Figure 5-4 presents an experiment for the horizontal loading of Footing 5 using an APS Dynamics Model 400 Electro-Seis shaker suspended from a tripod and configured to load in the horizontal direction. The horizontal load was applied to a steel frame attached to the footing surface, and the magnitude of the applied load was measured via a load cell attached between the shaker and frame connection. The photograph also displays the velocity transducers deployed at each of the four corners of the footing surface for measurement of the footing response to load.

Figures 5-5, 5-6, 5-7, and 5-8 present measurements of foundation load, horizontal displacement, and vertical displacement for shaker elevations of 1, 2, 3, and 4 ft above the top surface of the footing. The loading and measurement process was very similar to that described above for previous tests, and the results are displayed in the same complex number (real and imaginary) format. The responses at each of the foundation corners are presented individually in

the figures. It should be noted that the four horizontal displacements appear very similar for each elevation, indicating that the foundation is moving horizontally in a rigid-body-like fashion.

The vertical displacements are due to the rocking motion of the foundation. Here, it is observed that there are two pairs of similar data for each elevation. The similar responses are for the two corners along a foundation edge that is parallel to the axis of rocking. Of course, there are two such edges, and they are each on opposite sides of the axis of rocking. These responses should be at similar amplitude, but 180 degrees out of phase if the rocking axis is contained in the same vertical plane as the center of the foundation. Indeed, the data possess this symmetry: the real and imaginary pairs are both of similar magnitude, but opposite in sign (i.e., 180 degrees out of phase). This behavior also suggests a rigid-body-like rocking motion, and with this as an assumption, the rotation of the foundation can be calculated from the geometry and the vertical displacement responses.

Some other observations regarding these data are appropriate. First, it should be noted that the applied shaker force decreases significantly with increasing frequency. The APS 400 is ideally suited to apply constant force amplitude of about 70 pounds (340 KN) over a frequency range from about 1 to 10 Hz. Above 10 Hz, the force output diminishes significantly due to the limitations of the power amplifier. Second, it is observed that a system resonant response occurs at a frequency between 40 and 45 Hz. At resonance, the real component of the displacement passes through zero, and a local peak occurs in the imaginary component. The resonance effect is also noted in the force response for shaker positions at 3 and 4 ft. Unfortunately, the low force output coupled with a system resonance produces erratic behavior in the measured data at frequencies above approximately 35 Hz. The erratic behavior is more significant as the shaker becomes closer to the footing surface.

Using the measured load and displacement responses, impedance functions were calculated following the procedures described in Chapter 2.

First, Figures 5-9, 5-10, 5-11, and 5-12 present the real and imaginary components of the horizontal and rocking dynamic impedance functions for each of the four shaker positions and computed from the horizontal load and response measurements as well as the foundation characteristics. The impedance functions were calculated in accordance with the single degree of freedom method expressed in Equations 2-8 and 2-9, and thus assume that the cross-coupling impedances are zero. Because of the erratic behavior of the data discussed above, the impedance functions are displayed only to a maximum frequency of 30 Hz.

While there is some variability, it is observed that the impedance functions are consistent in both magnitude and variation with frequency (i.e., shape) for each of the four shaker positions. It is encouraging that the results are similar for each of the shaker positions, and suggests that the assumption of a linear relationship between force and displacement appears reasonable for this experimental configuration.

Second, impedance functions were calculated from the measured load and displacement responses following the two-degree-of-freedom approach presented in Equations 12 through 15 in Chapter 2. These calculations require load and displacement data from experiments conducted at two independent shaker positions. Figures 13 through 18 present results for each of the six possible pairs of shaker position measurements (e.g., 1 ft and 2 ft, 1 ft and 3 ft, 1 ft and 4 ft, etc.), and assumes that the cross-coupling impedances are independent. Similarly, Figures 19 through 24 present results assuming the cross coupling impedances are equal to one another. As for the one-degree-of-freedom results presented above, all impedances are displayed to a maximum frequency of 30 Hz.

First, it is observed in both sets of results that many of the impedance functions calculated based on experimental data from the 1 ft shaker position are suspect. It is recalled that data from this position are most erratic. Several of these suspect impedances display erratic variation in magnitude with changing frequency, and in a few cases negative values for the real (stiffness) or imaginary (damping) components are produced, which are very unlikely to be indicative of real physical behavior. On the other hand, the results produced from shaker position pairs of 2 ft and 3 ft, 2 ft and 4 ft, and 3 ft and 4 ft appear consistent in both magnitudes and shape, and do not display the negative values previously noted.

Finally, as a means of comparison between solution techniques, Figure 25 presents impedance functions from a one-degree-of-freedom solution at position 4 ft (Figure 12), a two-degree-of-freedom solution with independent cross-coupling using shaker positions 2 ft and 4 ft (Figure 17), and a two-degree-of-freedom solution assuming equal cross-coupling and using shaker positions 2 ft and 4 ft (Figure 23).

A last issue needs to be addressed regarding the calculation of impedance functions from the measured load and response data presented herein, and following the procedures detailed in Chapter 2. In Chapter 2, Equations 10 and 11 enable calculation of the horizontal soil force,  $F_s$ , and the rocking moment,  $M_s$ , referenced to the foundation soil interface at the horizontal center of the footing. The calculation of  $F_s$  and  $M_s$  for a given frequency, are based upon several parameters that include the footing mass and geometric characteristics, the input shaker force, and the measured displacements of the foundation, assuming that the foundation moves as a rigid body. As noted above, the assumption of rigid body motion appears reasonable. In addition, the calculation of  $F_s$  and  $M_s$  also depends on the mass and geometric characteristics and the displacements of the attached frame for those cases in which a frame was utilized in the

experiment. Two approaches were utilized and compared for determination of the frame displacements. First, like the foundation, the frame was assumed to behave as a rigid body, and thus the frame displacements were as determined from the responses of the geophones attached to the footing. Second, the frame displacements were calculated using a structural dynamics model available in Paz and Leigh (2004) that will account for the flexibility of the frame rather than assume rigid body motion. The model assumed the frame was a cantilever beam subdivided into elements, each with appropriate lumped mass and stiffness properties. Utilizing these two sets of frame displacements, two sets of impedance functions were calculated. It was found that the two impedance function sets were essentially identical, which indicates that the inertial effects due to flexibility of the frame were inconsequential in these experiments. All of the impedance functions presented herein are based upon frame displacements calculated using the structural dynamics model.

## **5.2 Footing 6**

### **5.2.1 Vertical loading**

Figure 5-26 and 5-27 present the experiment for the vertical loading of Footing 6 using the shaker named Thumper provided by the University of Texas. The shaker was configured to load in the vertical direction. Magnitude and frequency of the load were determined by an Interface Model 1020 load cell. In the photograph in Figure 5-25 three velocity transducers can be seen deployed at each of the four corners of the footing surface for measurement of the footing response to load. While it appears the tires are resting on the footing, Thumper is actually supported by four black bladders, two of which can be seen compressed in Figure 5-26. The bladders allow the shaker to dynamically load the footing while isolating the truck from vibration.

Figure 5-28 presents measurements of foundation load and vertical displacement in similar fashion to Figure 5-2. Figure 5-28a displays amplitude of vertical load as a function of frequency. The resulting vertical displacement response of the foundation is displayed in Figures 5-28b and 5-28c. The complex number (real and imaginary) format containing both the amplitude of the sinusoidal displacement response, as well as the phase lag of the displacement from the applied sinusoidal loading is again used. As with the ANCO shaker, loading was conducted in a steady-state mode to allow several cycles of load to be applied at a constant frequency, beginning at the lowest frequency. The dynamic response of the foundation was measured simultaneously via the velocity transducers, and recorded via a dynamic signal analyzer capable of characterizing the signals in complex number format. The displacement response was determined by integration of the velocity transducer measurements, and the loading was repeated at small increments of frequency through the frequency range noted in Figures 5-28b and 5-28c. Again, it is noted that the displacement responses are displayed for each of three corners of the foundation. Data for the fourth corner was not available due to a malfunctioning geophone. The three responses are similar, indicating that the foundation is moving vertically in a rigid-body-like fashion.

Figure 5-29 presents the real and imaginary components of the vertical dynamic impedance function calculated from the Thumper data. Vertical impedances for the test of Footing 6 using thumper were computed and displayed in the same fashion as those of Section 5.1.

Figures 5-30 and 5-31 are images of an experiment for the vertical loading of Footing 6 using the shaker provided by the University of Texas named T-Rex. The shaker was configured to load in the vertical direction. Magnitude and frequency of the load were determined by an Interface Model 1240 load cell exhibited in Figure 5-31. The photographs in Figure 5-30 and

Figure 5-31 also exhibit three velocity transducers deployed at each of the four corners of the footing surface for measurement of the footing response to load.

Figure 5-32 presents measurements of foundation load and vertical displacement. Figure 5-32a displays amplitude of vertical load for each frequency. The resulting vertical displacement responses of the foundation are found in Figures 5-32b and 5-32c. As with the test configurations discussed above, the complex number (real and imaginary) format contains both the amplitude of the sinusoidal displacement response, as well as the phase lag of the displacement from the applied sinusoidal loading. During the experiment, loading was conducted in a steady-state mode wherein several cycles of load were applied at a constant frequency, beginning at the lowest frequency. The dynamic response of the foundation was measured concurrently via the velocity transducers, and recorded via a dynamic signal analyzer capable of characterizing the signals in complex number format. The displacement response was determined by integration of the velocity transducer measurements, and the loading was repeated at small increments of frequency through the frequency range noted in Figures 5-32b and 5-32c. The displacement responses are presented for each of the four corners of the foundation. The four responses are similar, indicating that the foundation is moving vertically as a rigid-body.

Figure 5-33 presents the real and imaginary components of the vertical dynamic impedance function. Impedances for the test of Footing 6 using T-Rex were calculated and presented in the same fashion as those from Sections 5.1 and 5.3.

### **5.2.2 Horizontal Loading**

Figure 5-34 and Figure 5-35 present two experiments for the horizontal loading of Footing 6 using an ANCO Model MK-12 rotating mass shaker configured to load in the horizontal direction. The first horizontal loading configuration was performed with the shaker attached directly to the foundation as illustrated by Figure 5-34. The second loading configuration

includes a frame attached to the foundation and the shaker attached to the top of the frame pictured in Figure 5-35. The magnitude of the load was determined by the speed and eccentricity settings of the rotating masses. The photograph in Figure 5-34 also displays the velocity transducers deployed at each of the four corners of the footing surface for measurement of the footing response to load.

Figures 5-36 and 5-37 present measurements of foundation load, horizontal displacement, and vertical displacement for the flush mounting and the elevated mounting. The loading and measurement process was very similar to those of previously mentioned loading experiments, and the results displayed in Figure 5-36 and Figure 5-37 are in the same complex number (real and imaginary) format. The responses at each of the foundation corners are displayed individually in the figures. It should be noted that the four horizontal displacements are very similar for each shaker arrangement, which in part indicates that the foundation is moving horizontally in a rigid-body-like fashion.

The vertical displacements are due to the rocking motion of the foundation. As with the horizontal test of Section 5.2, it is observed that there are two pairs of similar data. The similar responses are for the two corners along a foundation edge that is parallel to the axis of rocking. There are two such edges, and they are each on opposite sides of the axis of rocking. These responses should be at similar amplitude, but 180 degrees out of phase if the rocking axis is contained in the same vertical plane as the center of the foundation. The displacements possess this symmetry: the real and imaginary pairs are both of similar magnitude, but opposite in sign. This behavior suggests rigid-body rocking motion, and with this as an assumption, the rotation of the foundation can be calculated from the geometry and the vertical displacement responses.

Using the measured load and displacement responses, impedance functions were calculated following the procedures described in Chapter 2.

Figures 5-38 and 5-39 present the real and imaginary components of the horizontal and rocking dynamic impedance functions for each of the two shaker positions and computed from the horizontal load and response measurements as well as the foundation characteristics. The impedance functions were calculated in accordance with the single-degree-of-freedom method expressed in Equations 2-8 and 2-9, and thus assume that the cross-coupling impedances are zero.

While there is some variability, it is observed that the impedance functions are similar in both magnitude and variation with frequency (i.e., shape) for the two shaker positions. If anything, the behavior of the horizontal impedance function for the elevated position displays more erratic behavior for frequency above 25 Hz.

Impedance functions were calculated from the measured load and displacement responses following the two-degree-of-freedom approach presented in Equations 12 through 15 in Chapter 2. These calculations require load and displacement data from experiments conducted at two independent shaker positions. Figure 40 presents results assuming that the cross-coupling impedances are independent, while results shown in Figure 41 assume the cross coupling impedances are equal to one another. While there are some instances of erratic behavior, it is observed that the impedance functions are similar in both magnitude and variation with frequency (i.e., shape) for the two solution techniques.

As a means of comparison between solution techniques, Figure 42 presents impedance functions from one-degree-of-freedom solutions for both flush and elevated mountings (Figures

38 and 39), and the two-degree-of-freedom solution with independent cross-coupling (Figure 40) and the two-degree-of-freedom solution assuming equal cross-coupling (Figure 41).



Figure 5-1. Vertical Experiment for Footing 5 with ANCO shaker.

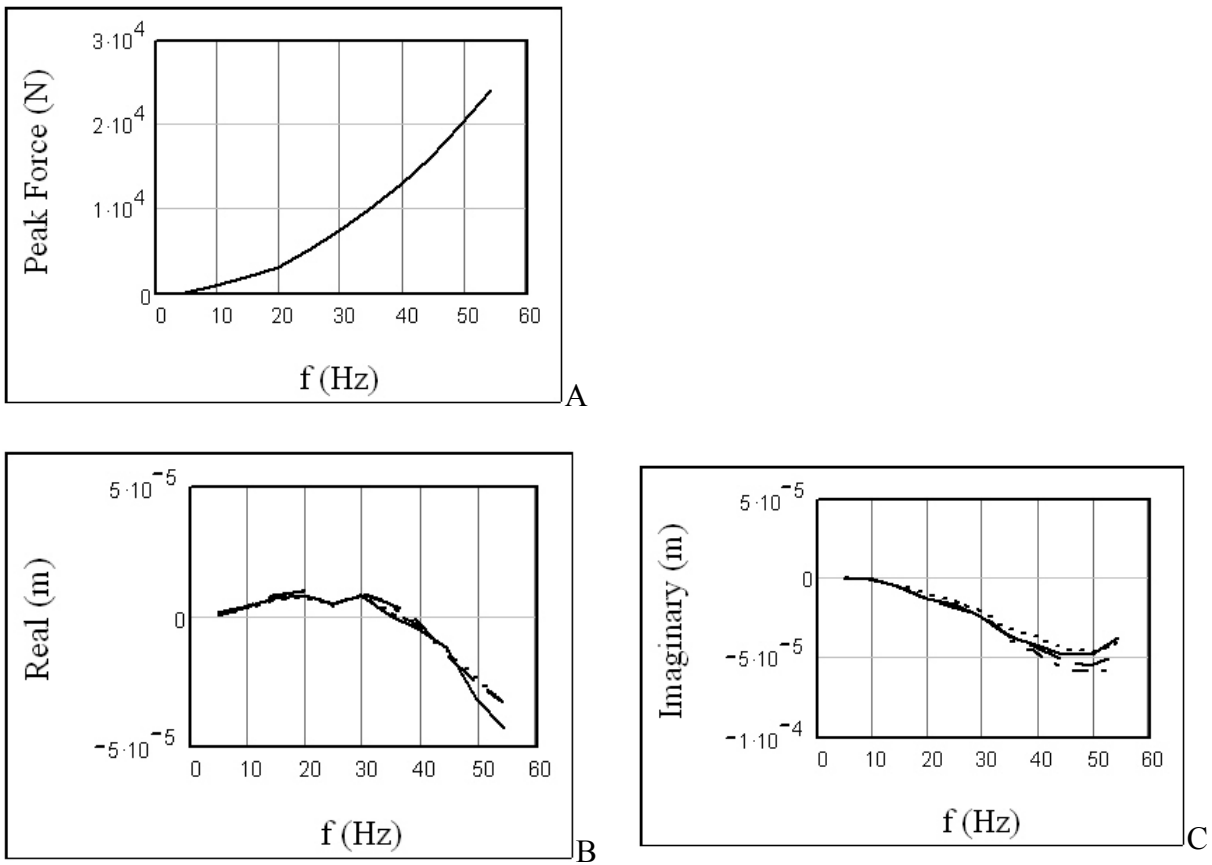


Figure 5-2. ANCO vertical results for Footing 5. A) Vertical Load. B) Vertical Displacement, Real Component. C) Vertical Displacement, Imaginary Component.

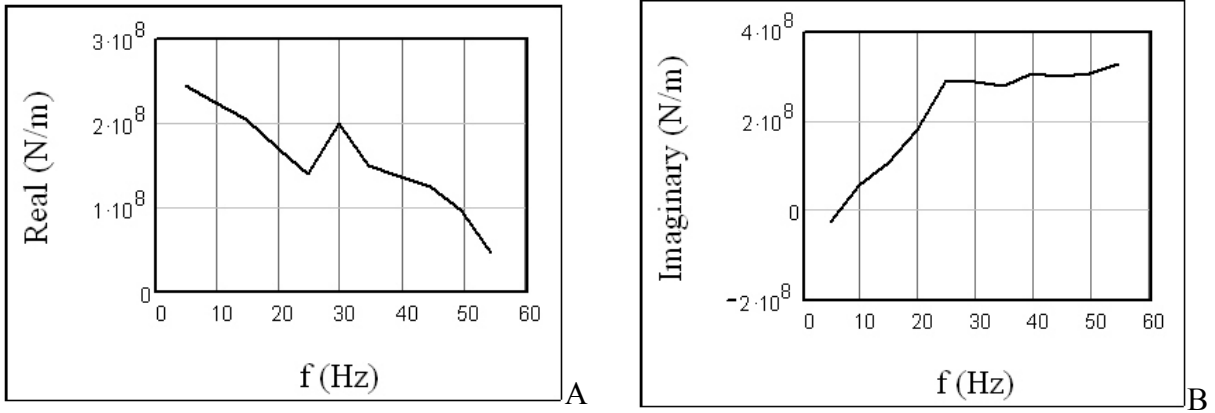


Figure 5-3. ANCO vertical results for Footing 5. A) Vertical Impedance, Real Component. B) Vertical Impedance, Imaginary Component.



Figure 5-4. Horizontal Experiment for Footing 5 with Model 400 Electro-Seis shaker.

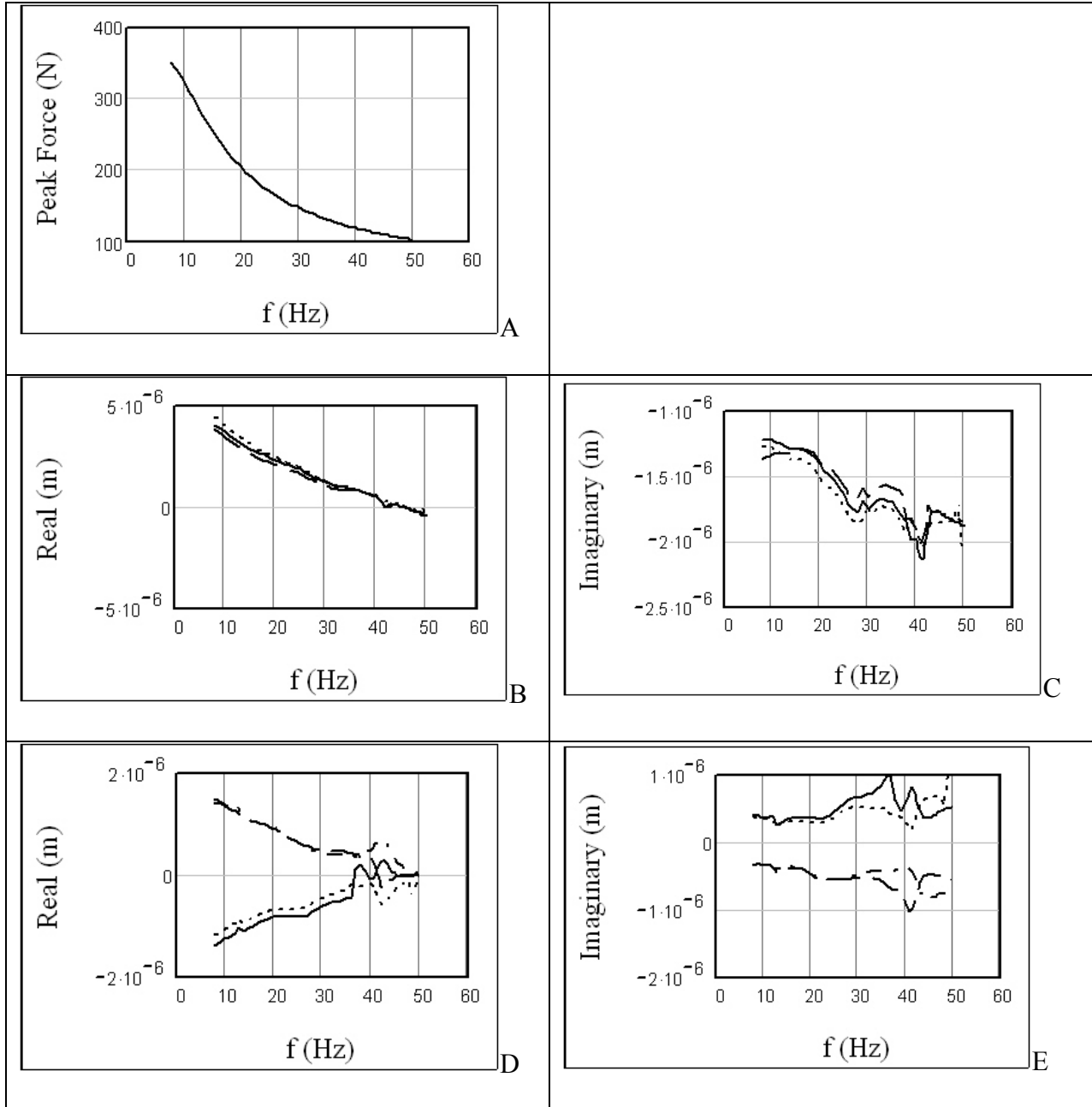


Figure 5-5. Electro-Seis horizontal loading results for Footing 5 at elevation 1 ft. A) Horizontal Load. B) Horizontal Displacement, Real Component. C) Horizontal Displacement, Imaginary Component. D) Vertical Displacement, Real Component. E) Vertical Displacement, Imaginary Component.

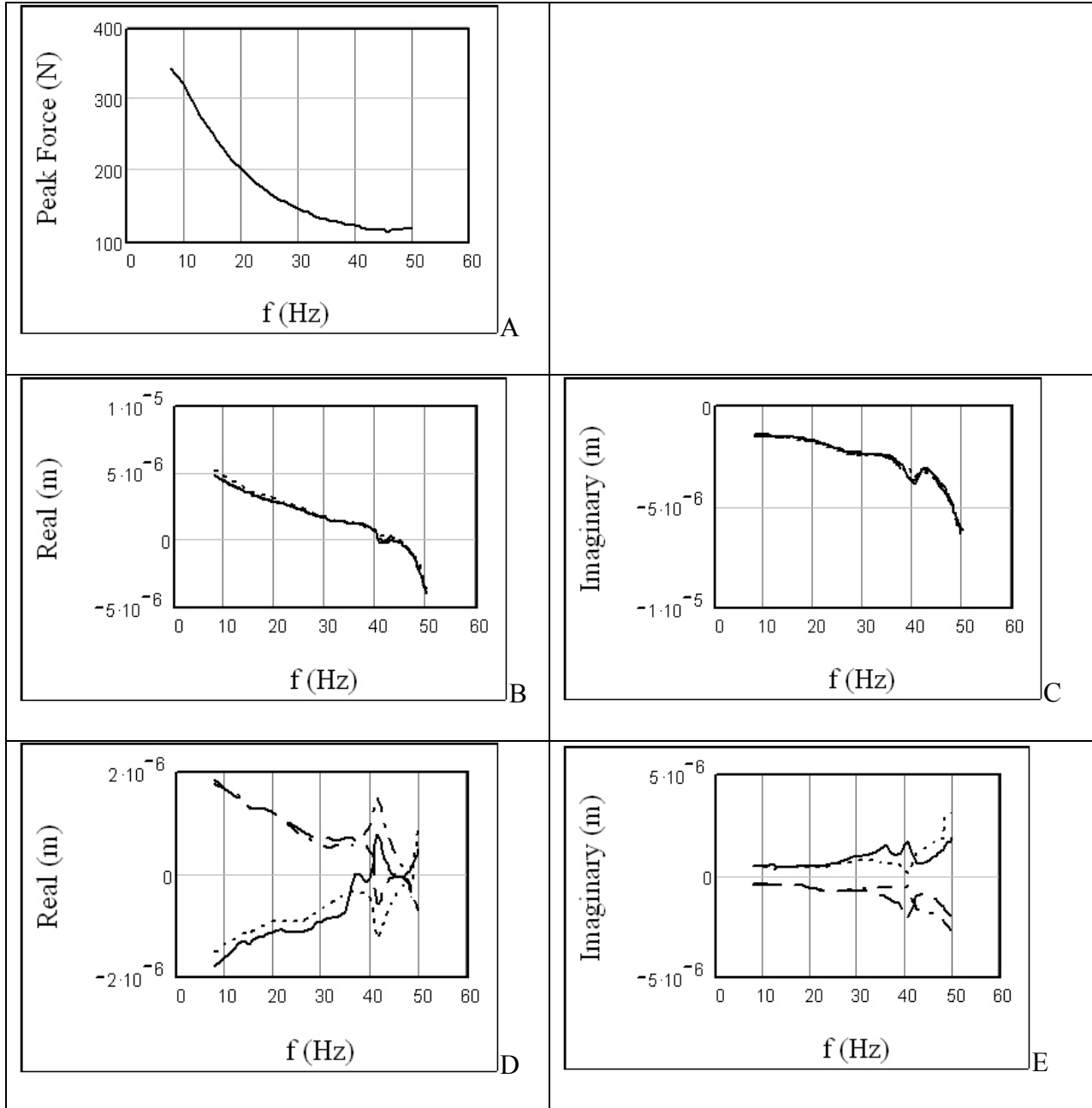


Figure 5-6. Electro-Seis horizontal loading results for Footing 5 at elevation 2 ft. A) Horizontal Load. B) Horizontal Displacement, Real Component. C) Horizontal Displacement, Imaginary Component. D) Vertical Displacement, Real Component. E) Vertical Displacement, Imaginary Component.

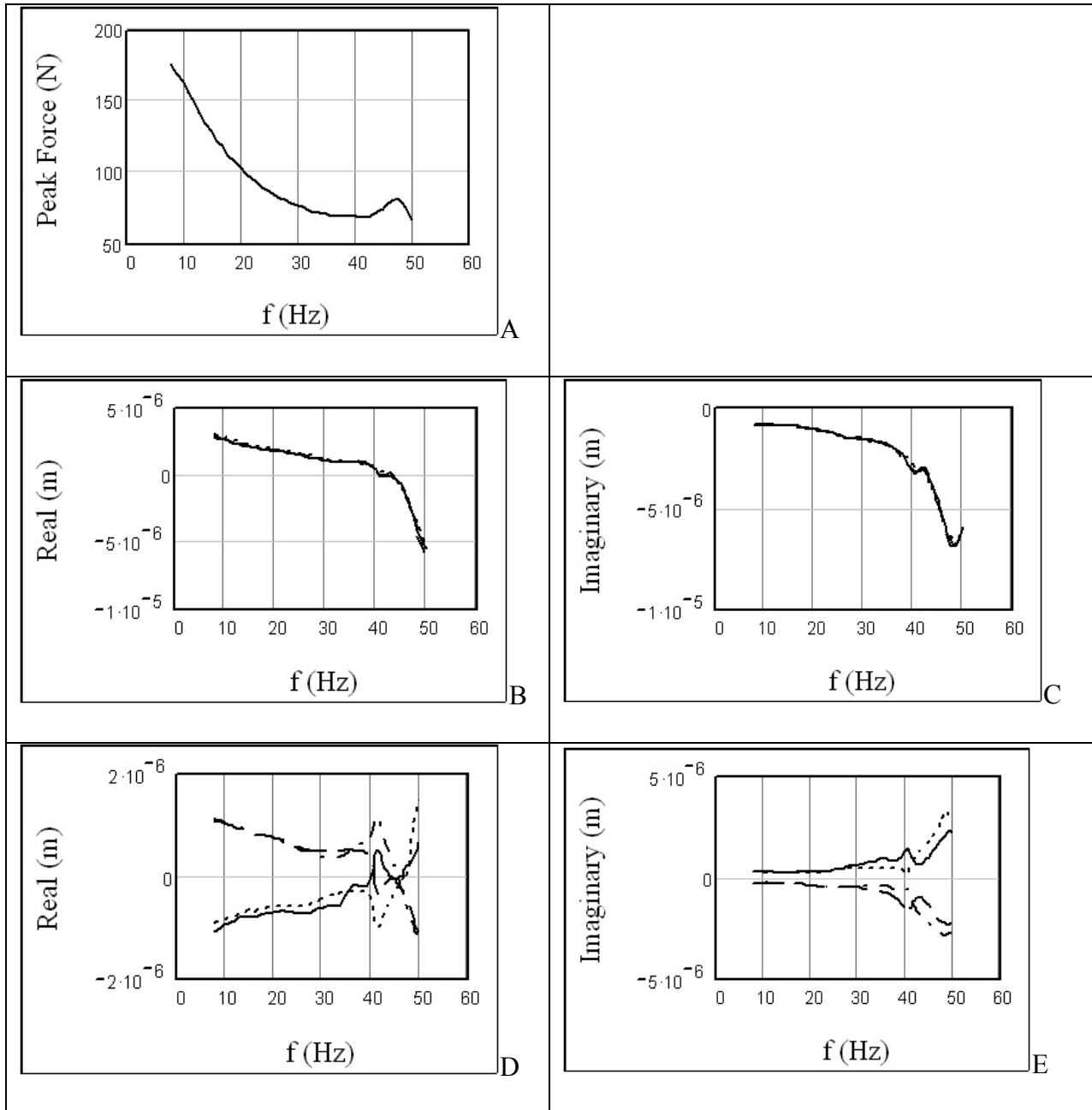


Figure 5-7. Electro-Seis horizontal loading results for Footing 5 at elevation 3 ft. A) Horizontal Load. B) Horizontal Displacement, Real Component. C) Horizontal Displacement, Imaginary Component. D) Vertical Displacement, Real Component. F) Vertical Displacement, Imaginary Component.

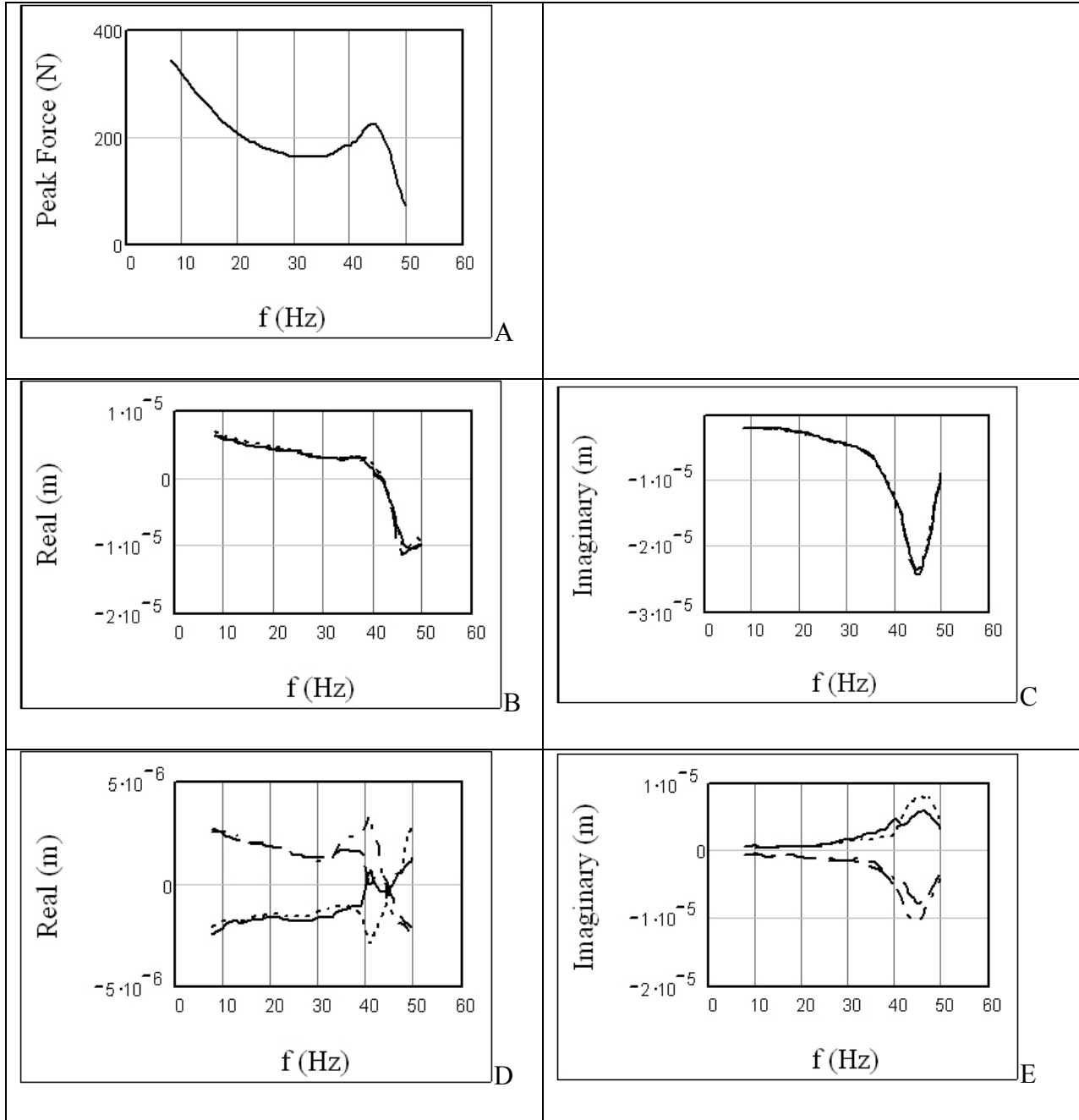


Figure 5-8. Electro-Seis horizontal loading results for Footing 5 at elevation 4 ft. A) Horizontal Load. B) Horizontal Displacement, Real Component. C) Horizontal Displacement, Imaginary Component. D) Vertical Displacement, Real Component. E) Vertical Displacement, Imaginary Component.

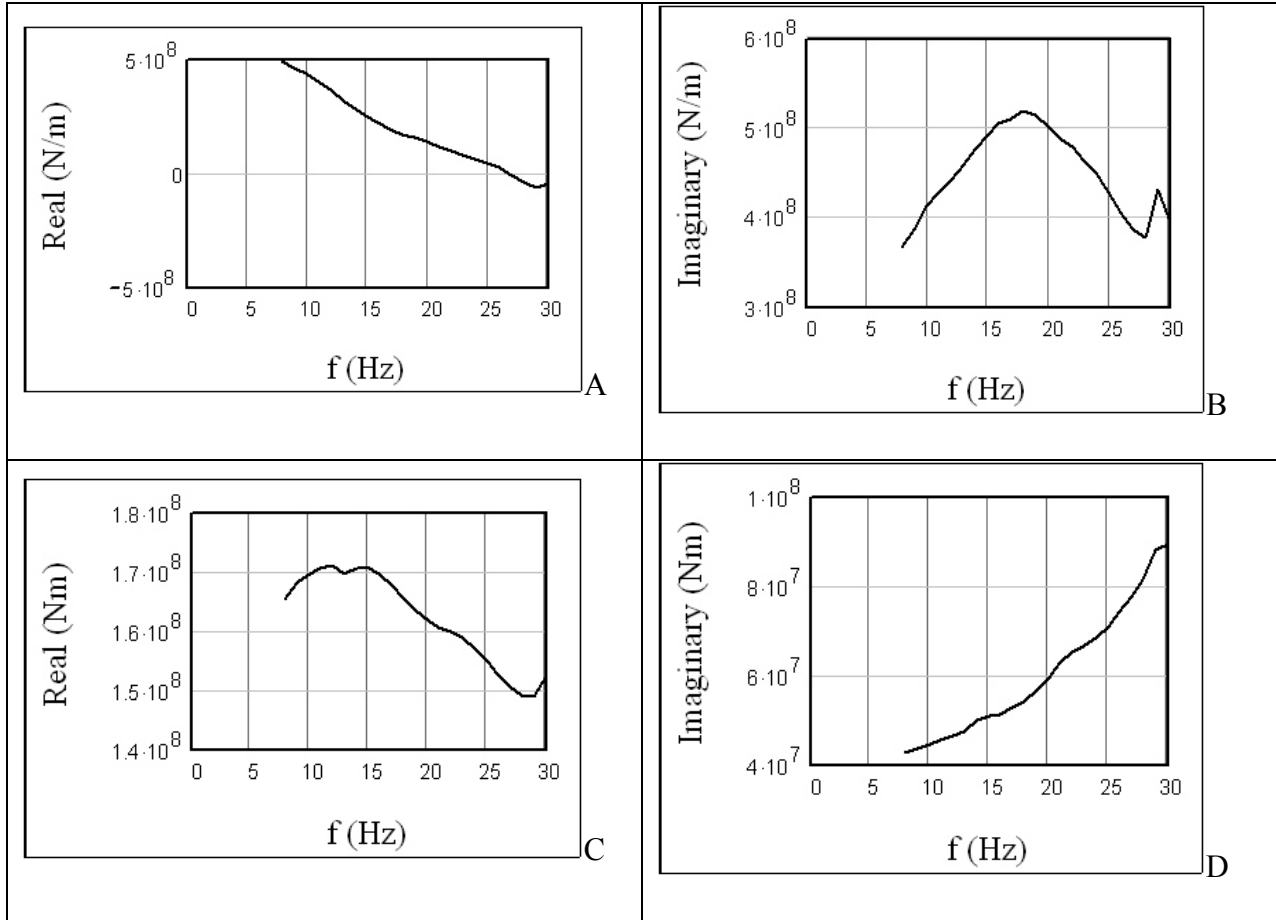


Figure 5-9. Electro-Seis horizontal loading results for the one-degree-of-freedom analyses of Footing 5 at elevation 1 ft. A) Horizontal Impedance, Real Component. B) Horizontal Impedance, Imaginary Component. C) Rocking Impedance, Real Component. D) Rocking Impedance, Imaginary Component.

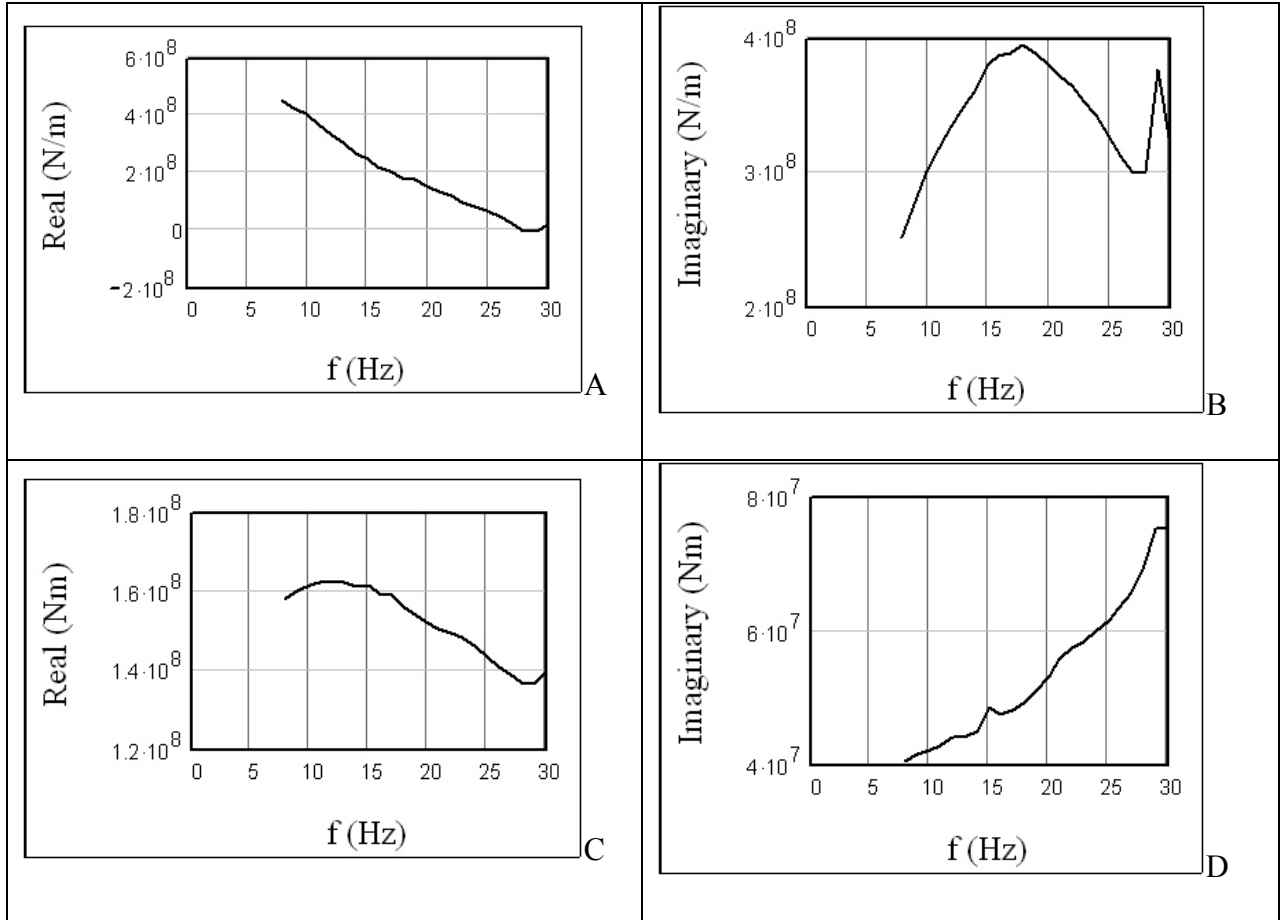


Figure 5-10. Electro-Seis horizontal loading results for the one-degree-of-freedom analyses of Footing 5 at elevation 2 ft. A) Horizontal Impedance, Real Component. B) Horizontal Impedance, Imaginary Component. C) Rocking Impedance, Real Component. D) Rocking Impedance, Imaginary Component.

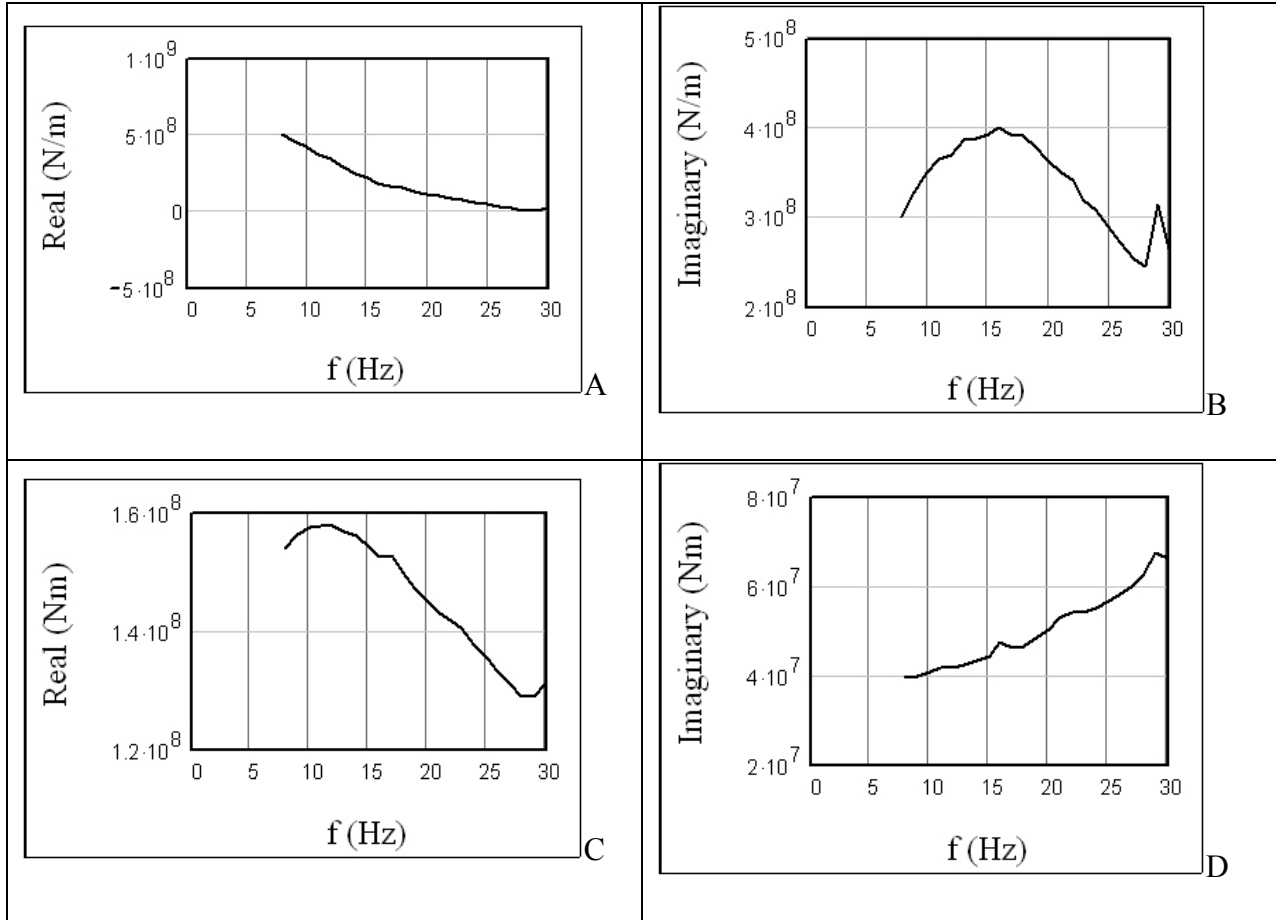


Figure 5-11. Electro-Seis horizontal loading results for the one-degree-of-freedom analyses of Footing 5 at elevation 3 ft. A) Horizontal Impedance, Real Component. B) Horizontal Impedance, Imaginary Component. C) Rocking Impedance, Real Component. D) Rocking Impedance, Imaginary Component.

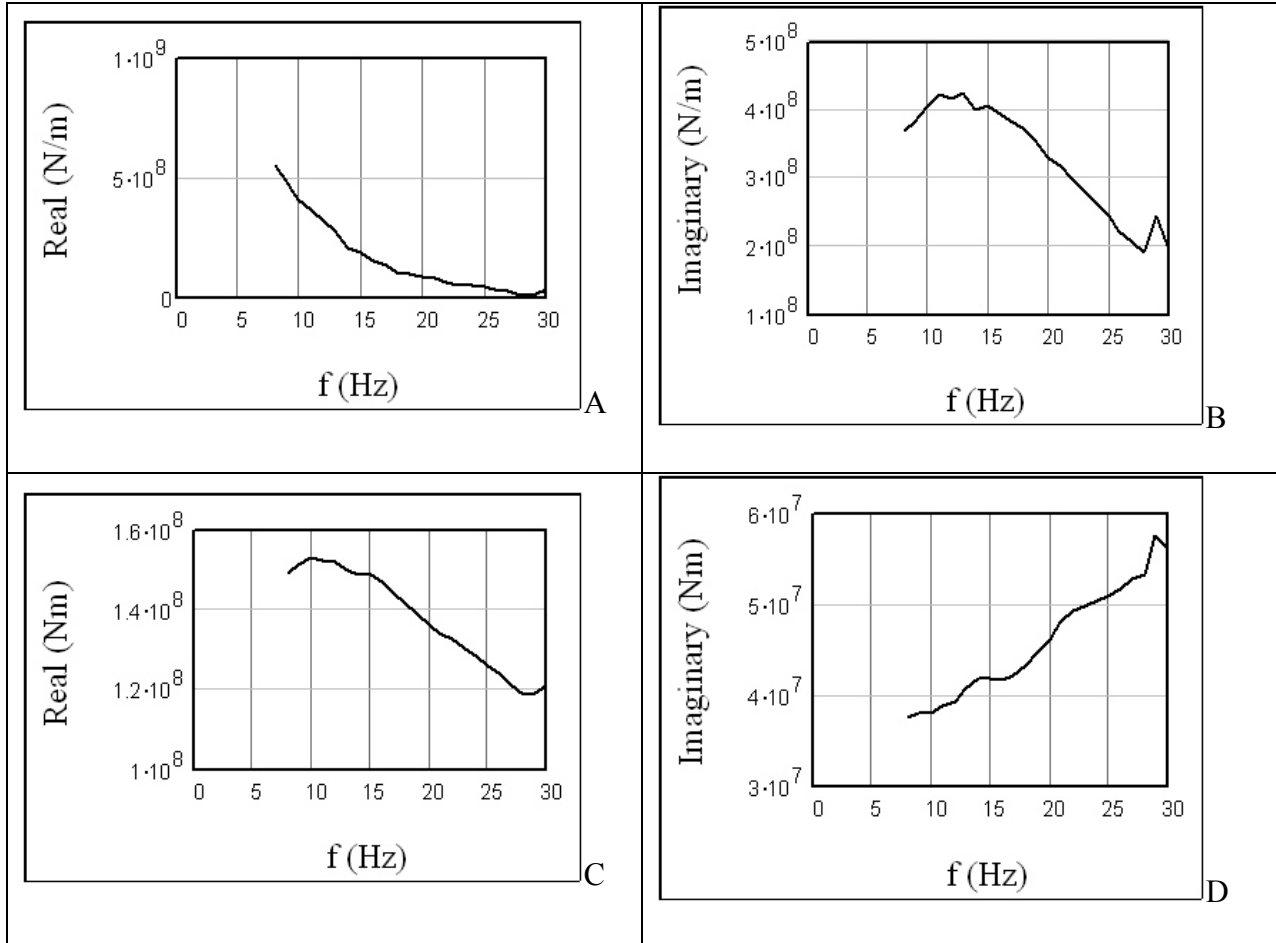


Figure 5-12. Electro-Seis horizontal loading results for the one-degree-of-freedom analyses of Footing 5 at elevation 4 ft. A) Horizontal Impedance, Real Component. B) Horizontal Impedance, Imaginary Component. C) Rocking Impedance, Real Component. D) Rocking Impedance, Imaginary Component.

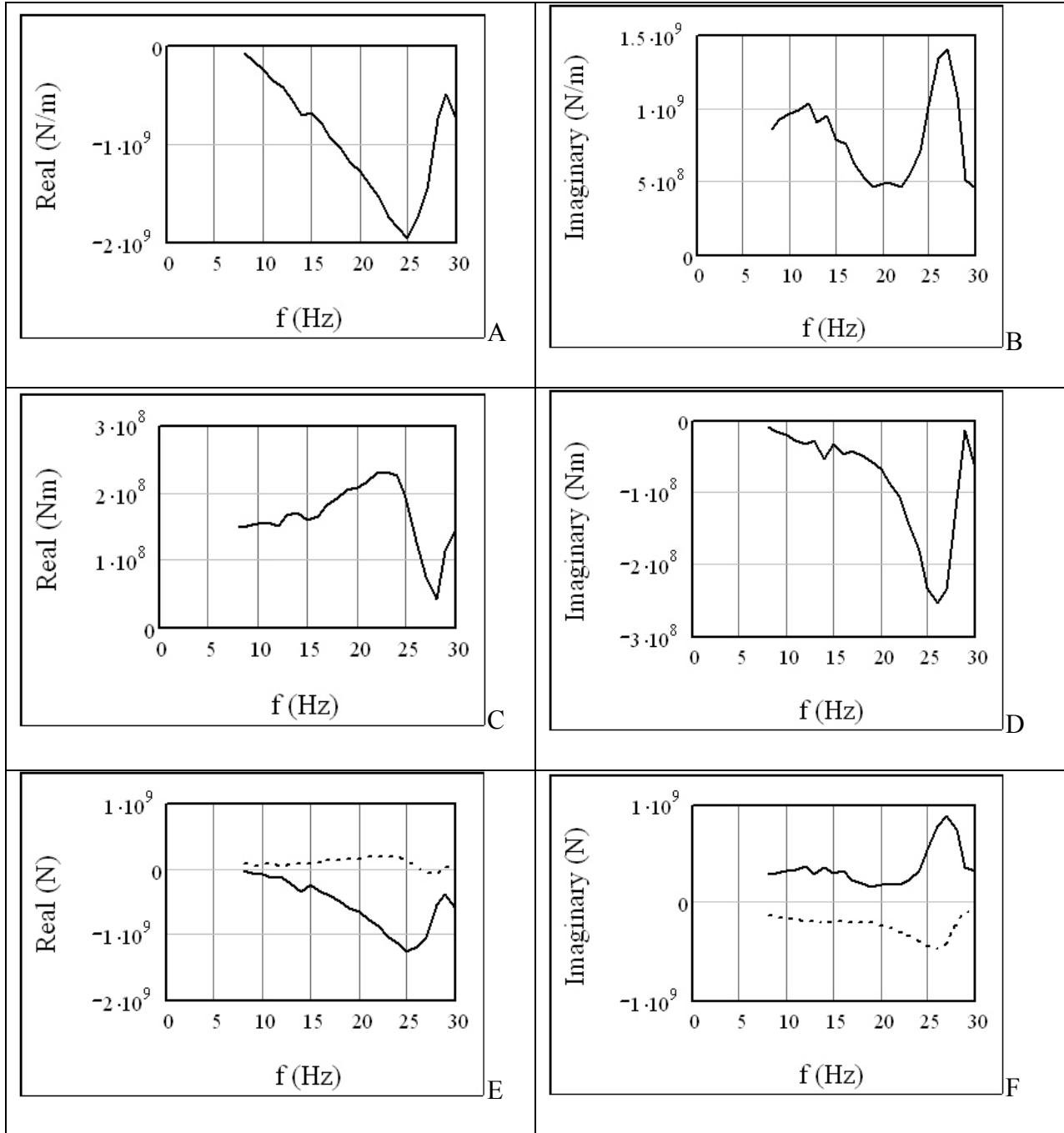


Figure 5-13. Electro-Seis horizontal loading results for the non-equal coupling two-degree-of-freedom analyses of Footing 5 at elevations 1 ft and 2 ft. A) Horizontal Impedance, Real Component. B) Horizontal Impedance, Imaginary Component. C) Rocking Impedance, Real Component. D) Rocking Impedance, Imaginary Component. E) Coupling Impedance, Real Component. F) Coupling Impedance, Imaginary Component.

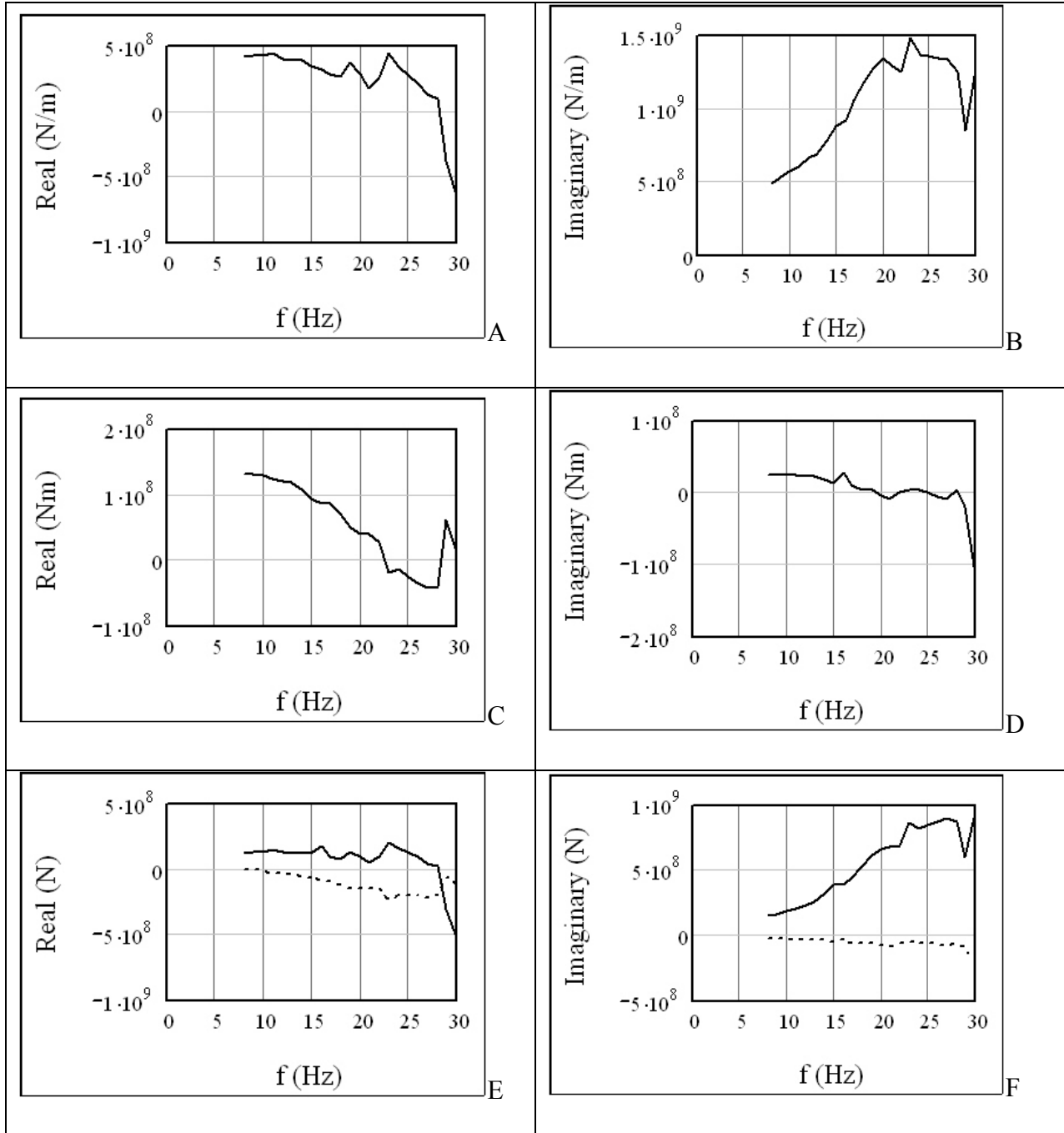


Figure 5-14. Electro-Seis horizontal loading results for the non-equal coupling two-degree-of-freedom analyses of Footing 5 at elevations 1 ft and 3 ft. A) Horizontal Impedance, Real Component. B) Horizontal Impedance, Imaginary Component. C) Rocking Impedance, Real Component. D) Rocking Impedance, Imaginary Component. E) Coupling Impedance, Real Component. F) Coupling Impedance, Imaginary Component.

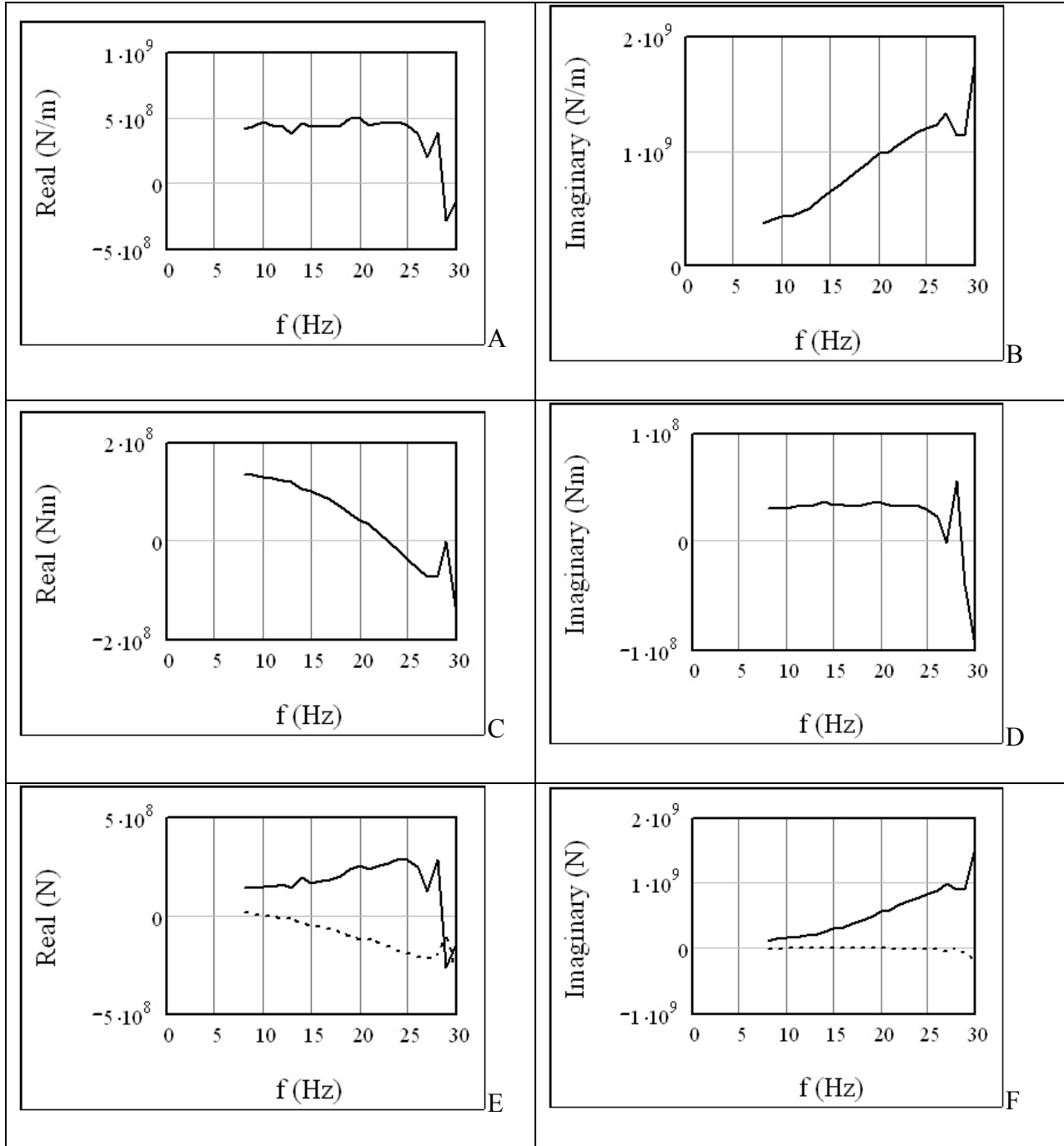


Figure 5-15. Electro-Seis horizontal loading results for the non-equal coupling two-degree-of-freedom analyses of Footing 5 at elevations 1 ft and 4 ft. A) Horizontal Impedance, Real Component. B) Horizontal Impedance, Imaginary Component. C) Rocking Impedance, Real Component. D) Rocking Impedance, Imaginary Component. E) Coupling Impedance, Real Component. F) Coupling Impedance, Imaginary Component.

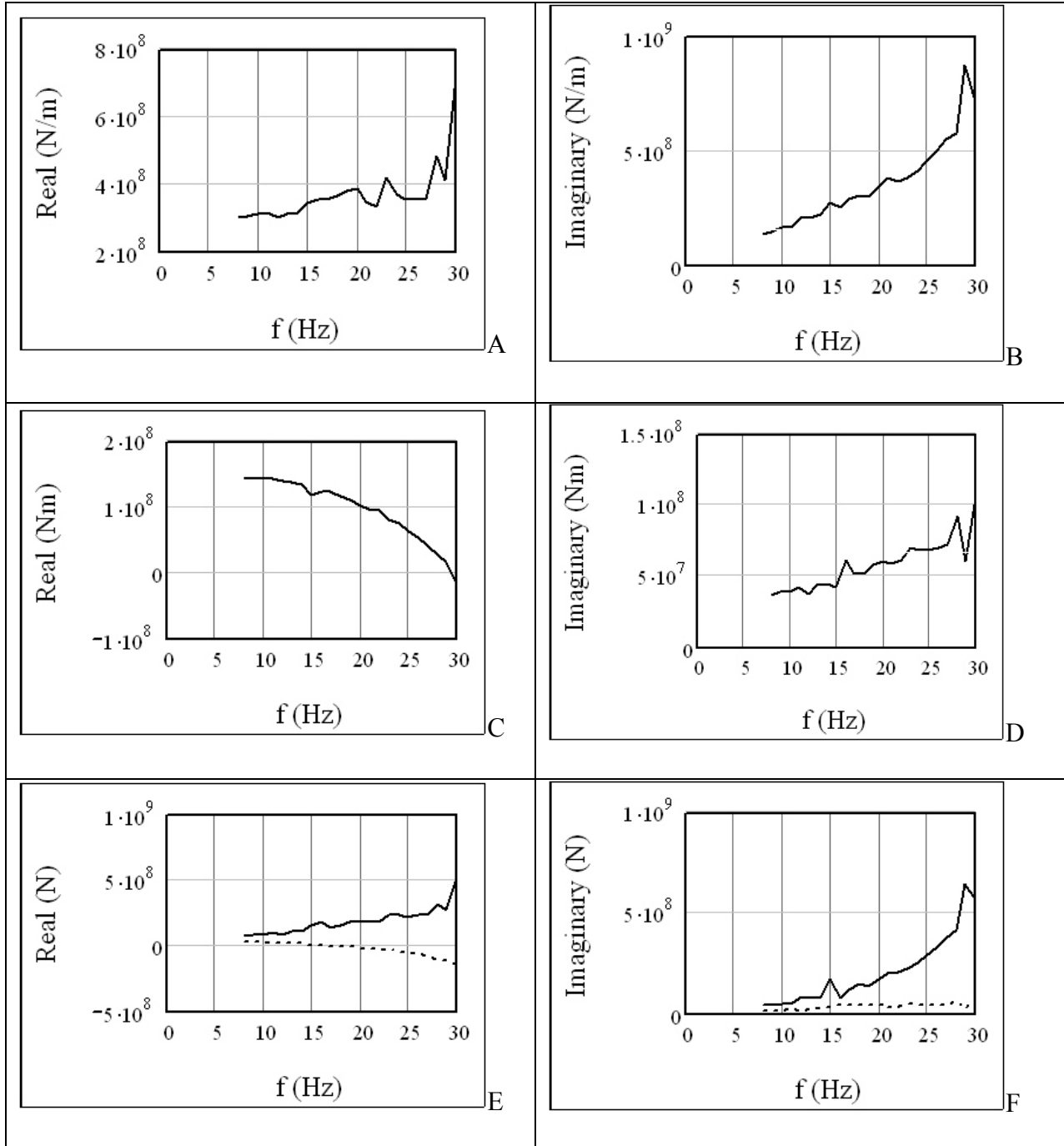


Figure 5-16. Electro-Seis horizontal loading results for the non-equal coupling two-degree-of-freedom analyses of Footing 5 at elevations 2 ft and 3 ft. A) Horizontal Impedance, Real Component. B) Horizontal Impedance, Imaginary Component. C) Rocking Impedance, Real Component. D) Rocking Impedance, Imaginary Component. E) Coupling Impedance, Real Component. F) Coupling Impedance, Imaginary Component.

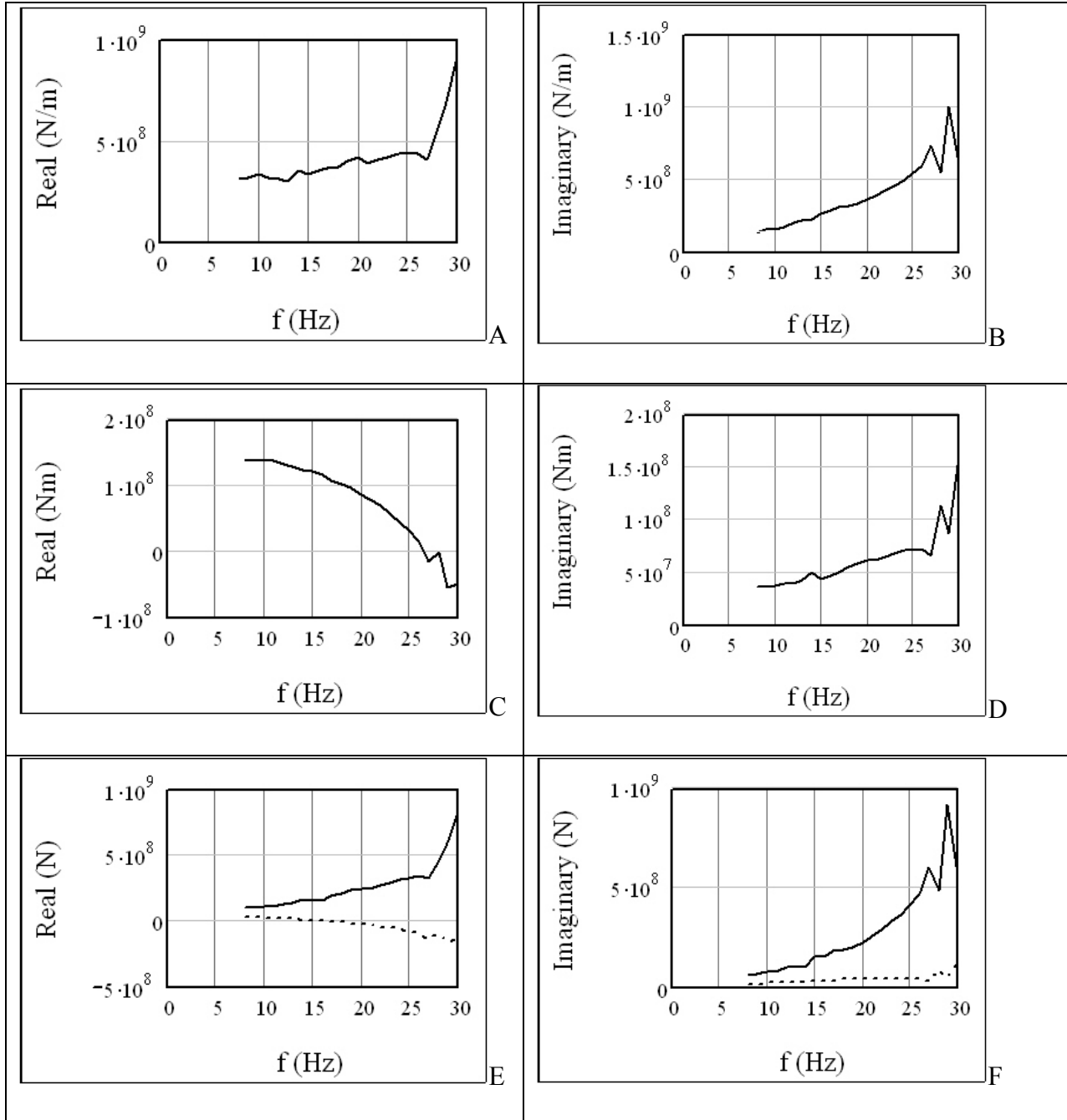


Figure 5-17. Electro-Seis horizontal loading results for the non-equal coupling two-degree-of-freedom analyses of Footing 5 at elevations 2 ft and 4 ft. A) Horizontal Impedance, Real Component. B) Horizontal Impedance, Imaginary Component. C) Rocking Impedance, Real Component. D) Rocking Impedance, Imaginary Component. E) Coupling Impedance, Real Component. F) Coupling Impedance, Imaginary Component.

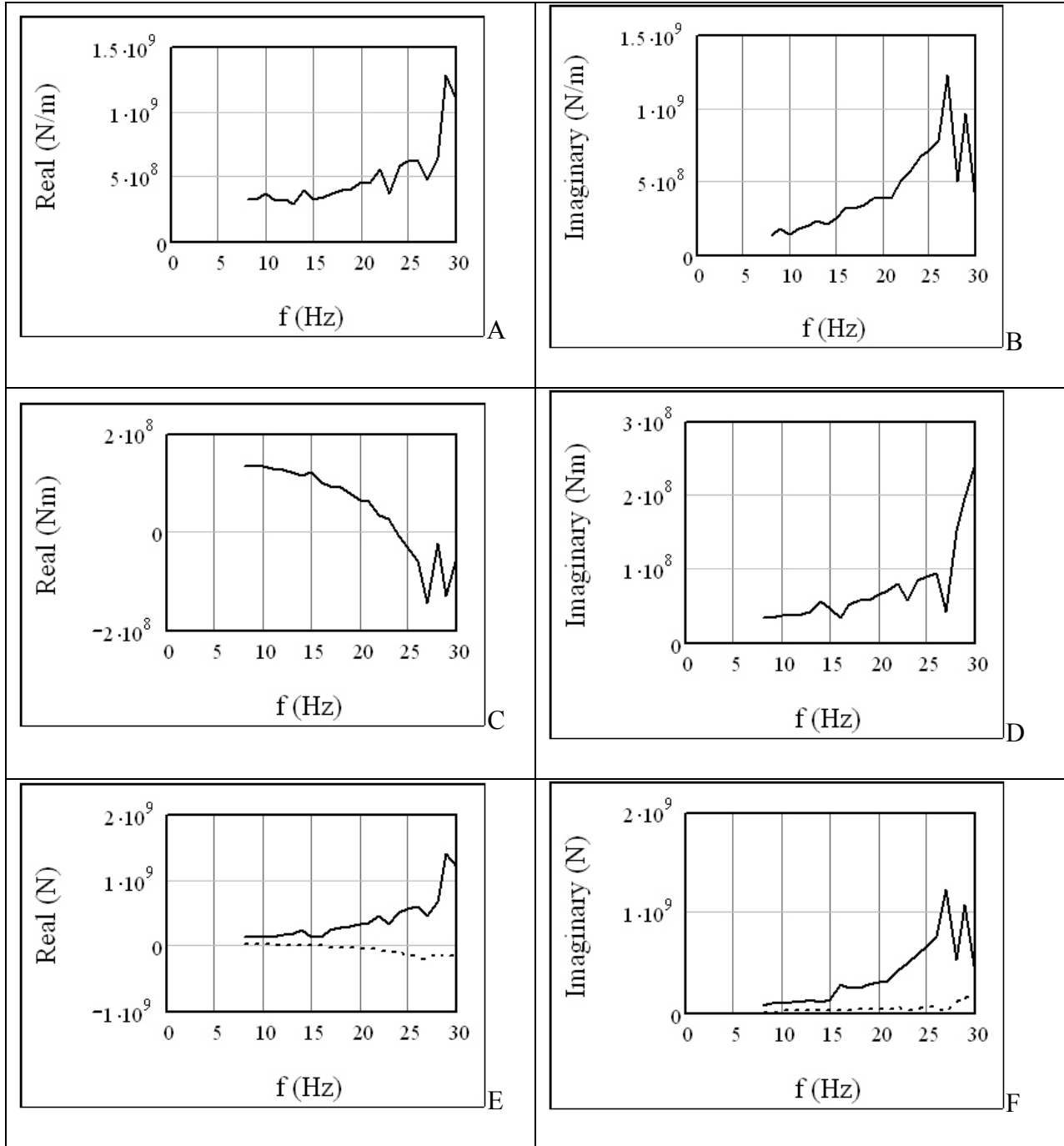


Figure 5-18. Electro-Seis horizontal loading results for the non-equal coupling two-degree-of-freedom analyses of Footing 5 at elevations 3 ft and 4 ft. A) Horizontal Impedance, Real Component. B) Horizontal Impedance, Imaginary Component. C) Rocking Impedance, Real Component. D) Rocking Impedance, Imaginary Component. E) Coupling Impedance, Real Component. F) Coupling Impedance, Imaginary Component.

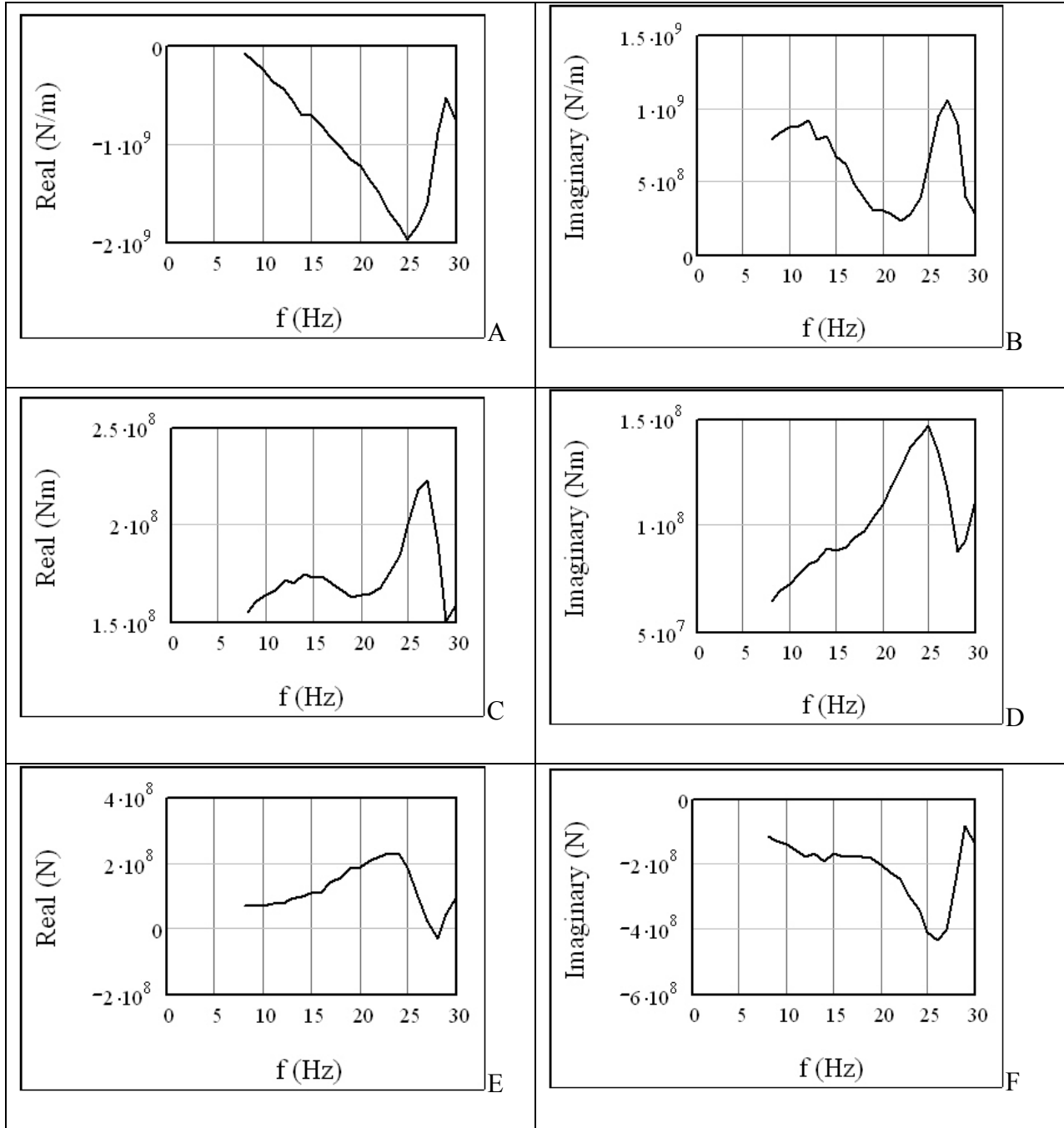


Figure 5-19. Electro-Seis horizontal loading results for the equal coupling two-degree-of-freedom analyses of Footing 5 at elevations 1 ft and 2 ft. A) Horizontal Impedance, Real Component. B) Horizontal Impedance, Imaginary Component. C) Rocking Impedance, Real Component. D) Rocking Impedance, Imaginary Component. E) Coupling Impedance, Real Component. F) Coupling Impedance, Imaginary Component.

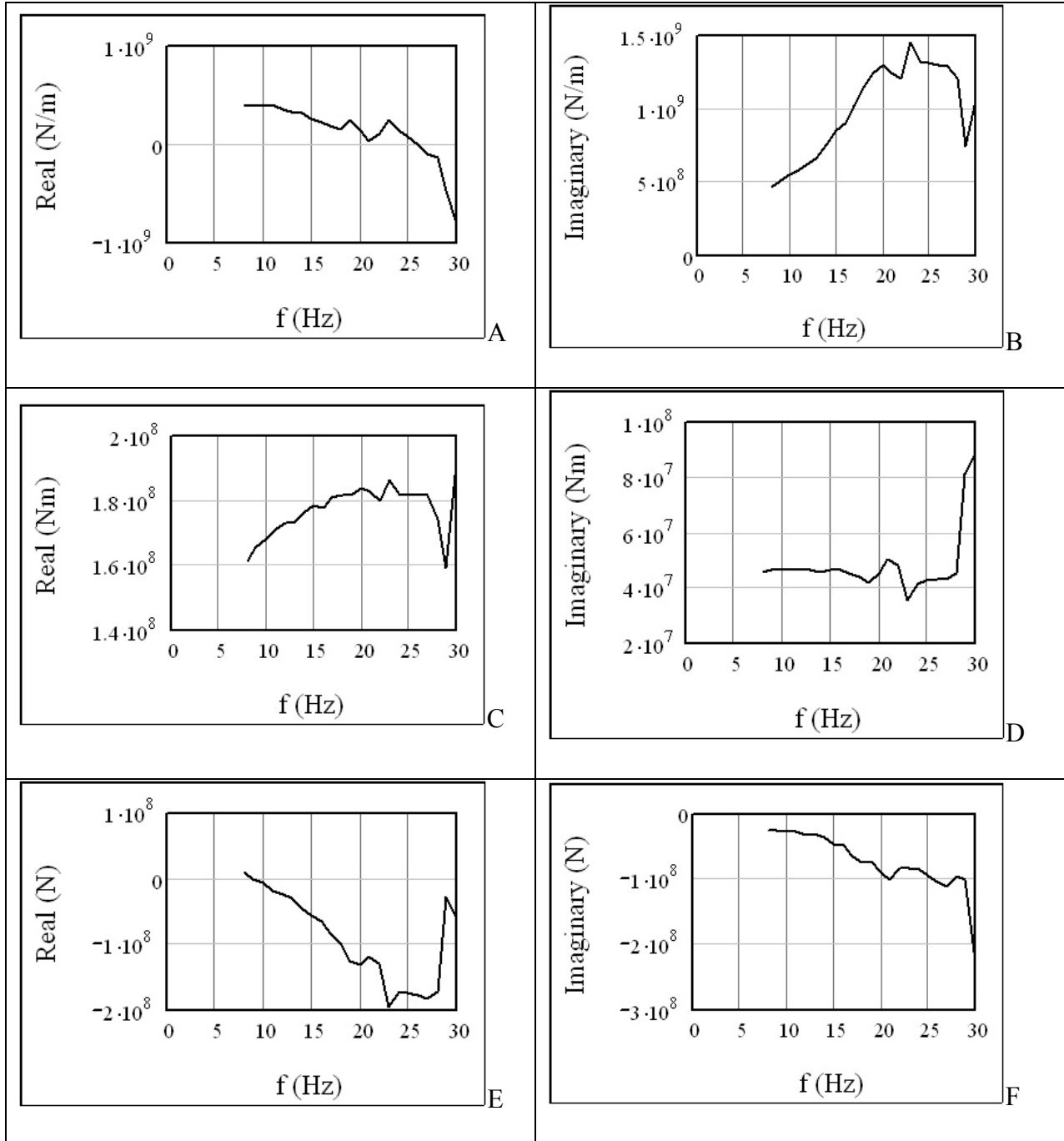


Figure 5-20. Electro-Seis horizontal loading results for the equal coupling two-degree-of-freedom analyses of Footing 5 at elevations 1 ft and 3 ft. A) Horizontal Impedance, Real Component. B) Horizontal Impedance, Imaginary Component. C) Rocking Impedance, Real Component. D) Rocking Impedance, Imaginary Component. E) Coupling Impedance, Real Component. F) Coupling Impedance, Imaginary Component.

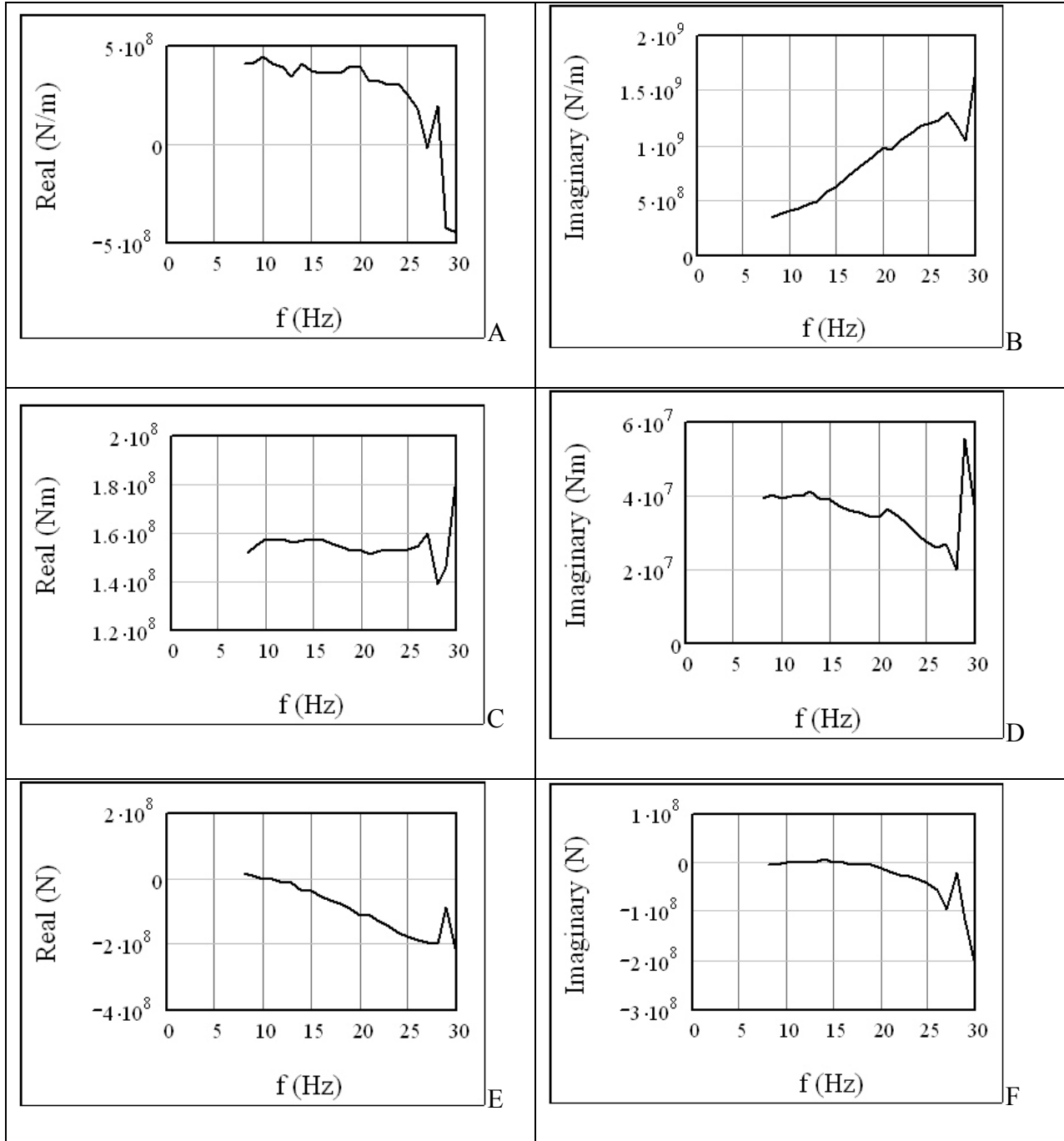


Figure 5-21. Electro-Seis horizontal loading results for the equal coupling two-degree-of-freedom analyses of Footing 5 at elevations 1 ft and 4 ft. A) Horizontal Impedance, Real Component. B) Horizontal Impedance, Imaginary Component. C) Rocking Impedance, Real Component. D) Rocking Impedance, Imaginary Component. E) Coupling Impedance, Real Component. F) Coupling Impedance, Imaginary Component.

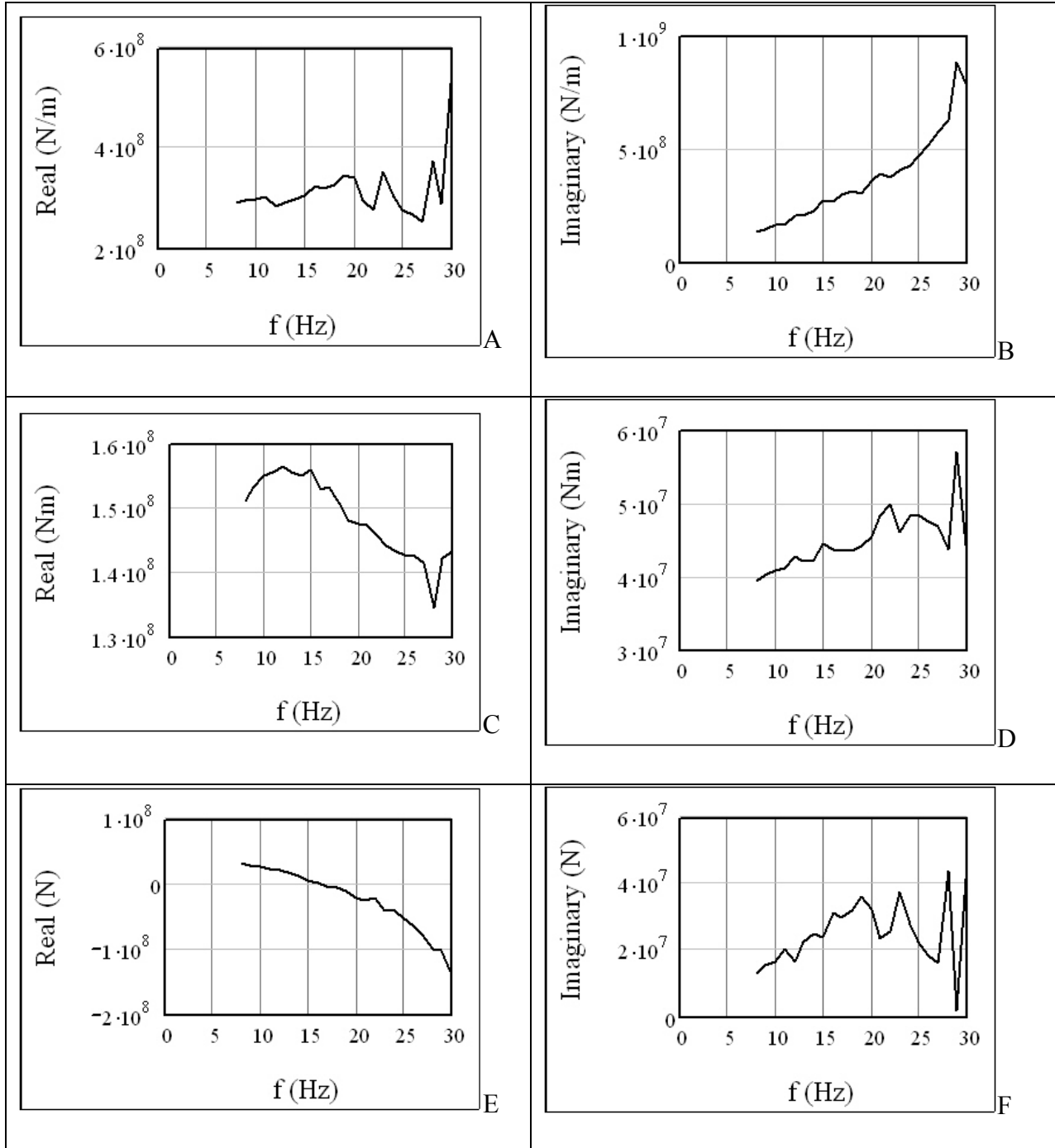


Figure 5-22. Electro-Seis horizontal loading results for the equal coupling two-degree-of-freedom analyses of Footing 5 at elevations 2 ft and 3 ft. A) Horizontal Impedance, Real Component. B) Horizontal Impedance, Imaginary Component. C) Rocking Impedance, Real Component. D) Rocking Impedance, Imaginary Component. E) Coupling Impedance, Real Component. F) Coupling Impedance, Imaginary Component.

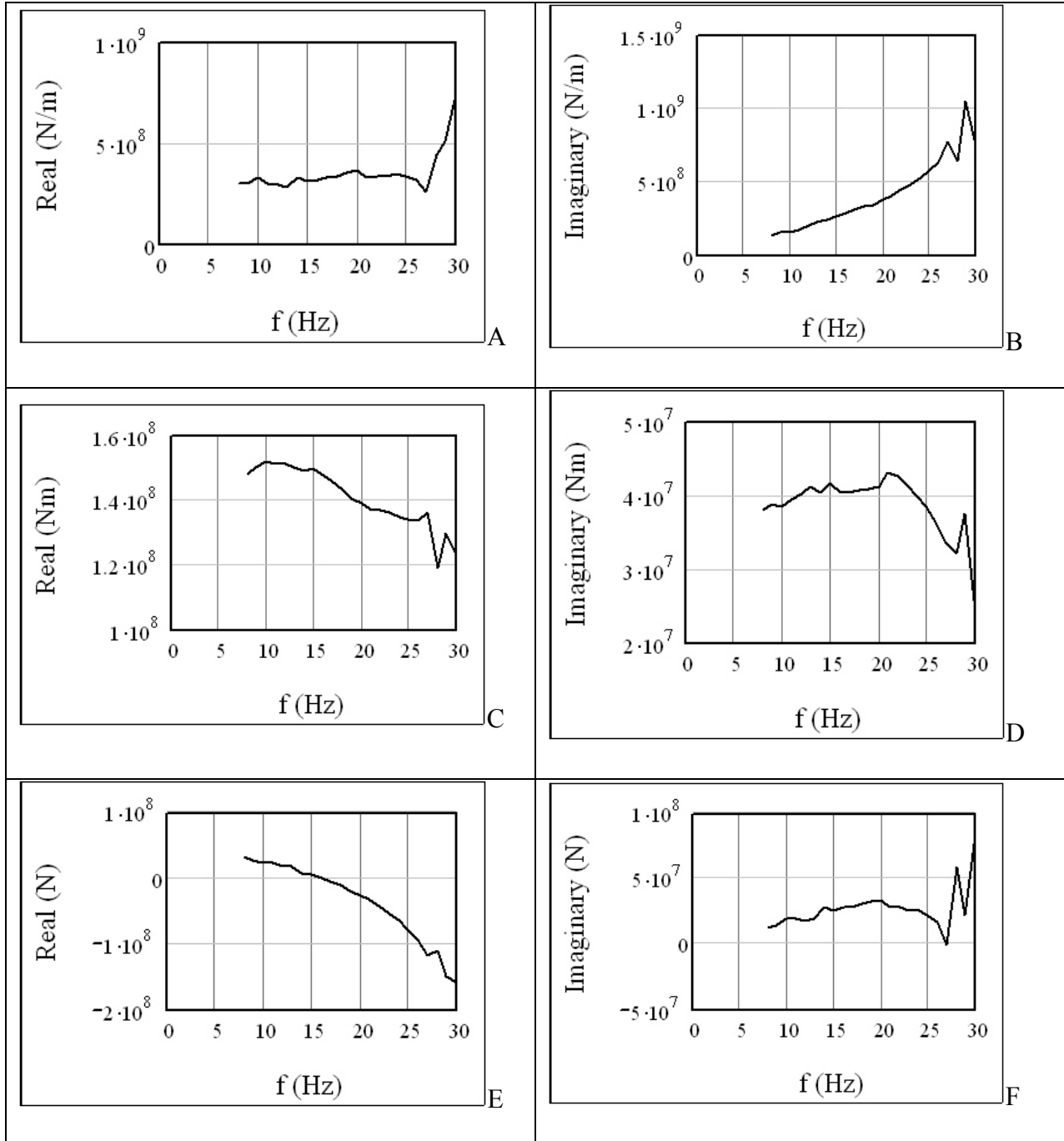


Figure 5-23. Electro-Seis horizontal loading results for the equal coupling two-degree-of-freedom analyses of Footing 5 at elevations 2 ft and 4 ft. A) Horizontal Impedance, Real Component. B) Horizontal Impedance, Imaginary Component. C) Rocking Impedance, Real Component. D) Rocking Impedance, Imaginary Component. E) Coupling Impedance, Real Component. F) Coupling Impedance, Imaginary Component.

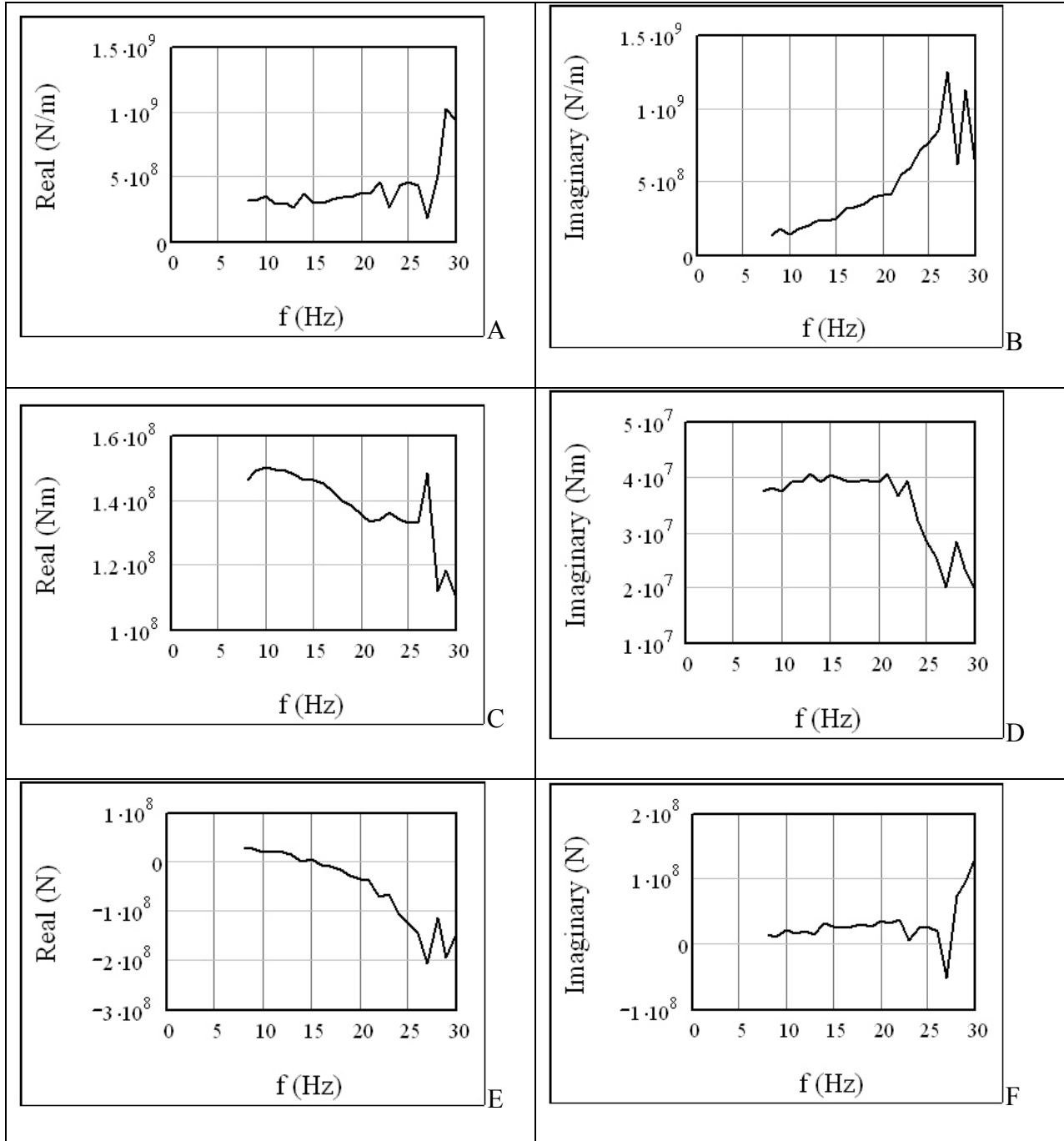


Figure 5-24. Electro-Seis horizontal loading results for the equal coupling two-degree-of-freedom analyses of Footing 5 at elevations 3 ft and 4 ft. A) Horizontal Impedance, Real Component. B) Horizontal Impedance, Imaginary Component. C) Rocking Impedance, Real Component. D) Rocking Impedance, Imaginary Component. E) Coupling Impedance, Real Component. F) Coupling Impedance, Imaginary Component.

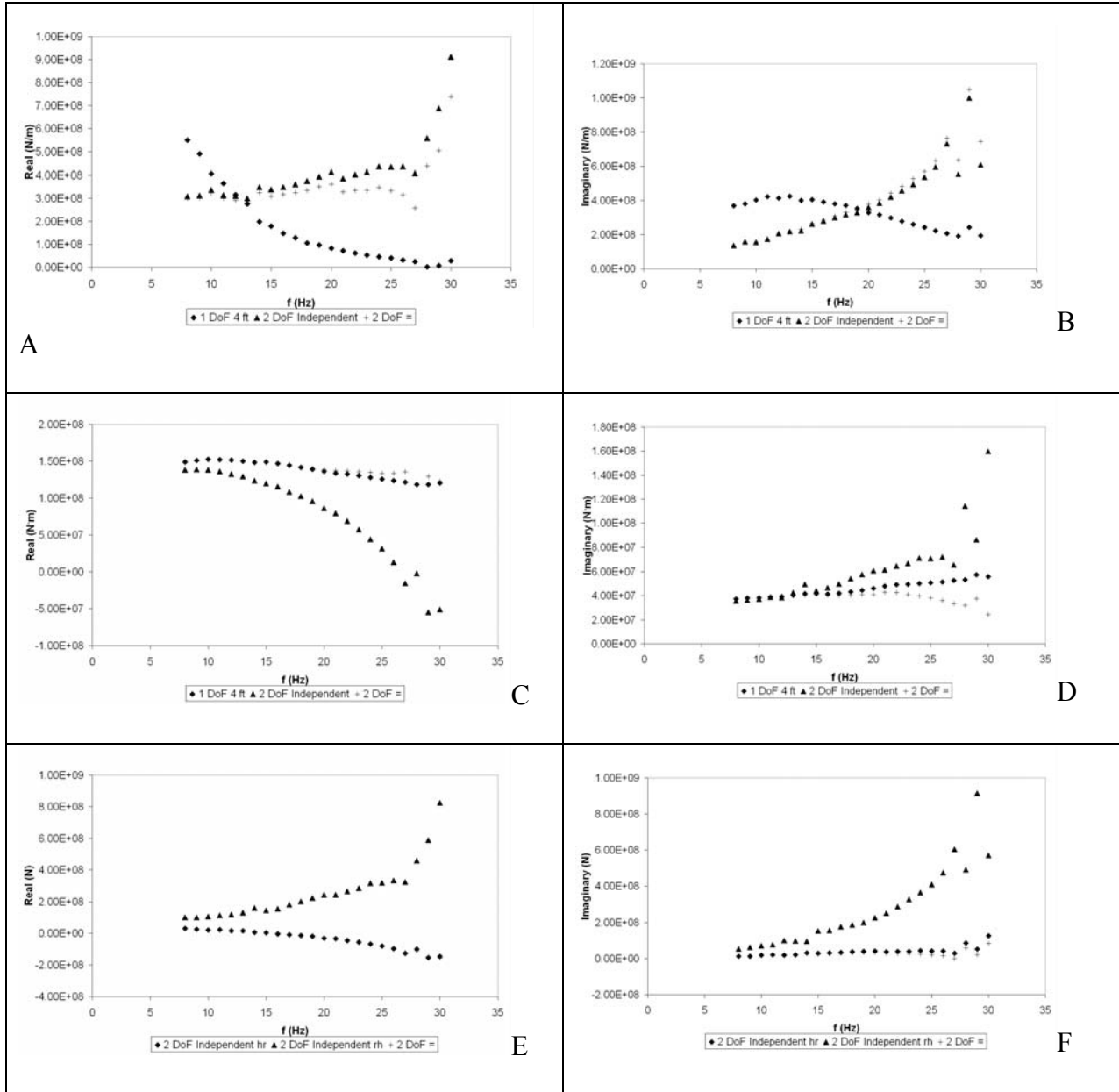


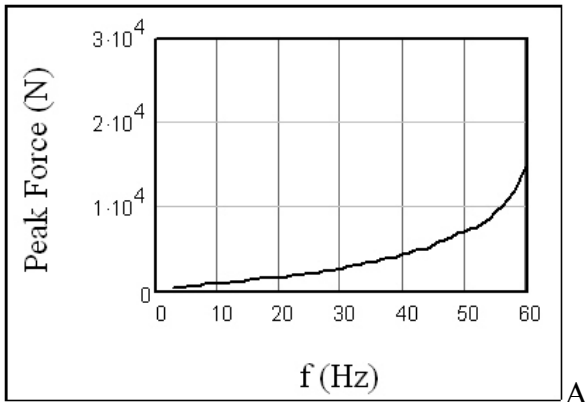
Figure 5-25. Electro-Seis horizontal loading results for the one-degree-of-freedom at 4 ft, independent coupling two-degree-of-freedom at 2 ft and 4 ft, the equal coupling two-degree-of-freedom analyses of Footing 5 at elevations 2 ft and 4 ft. A) Horizontal Impedance, Real Component. B) Horizontal Impedance, Imaginary Component. C) Rocking Impedance, Real Component. D) Rocking Impedance, Imaginary Component. E) Coupling Impedance, Real Component. F) Coupling Impedance, Imaginary Component.



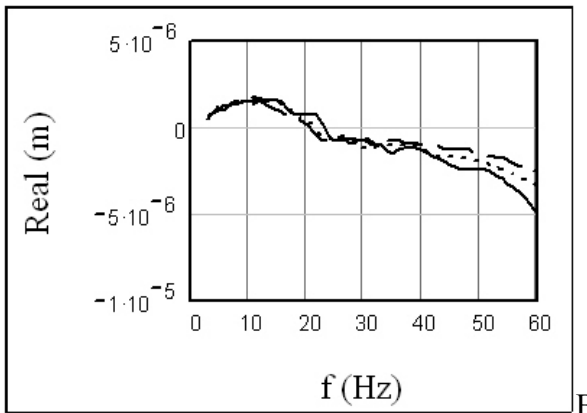
Figure 5-26. Vertical Experiment with Thumper shaker.



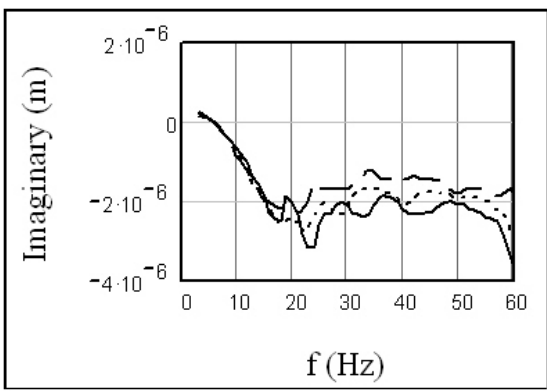
Figure 5-27. Vertical Experiment with Thumper shaker.



A

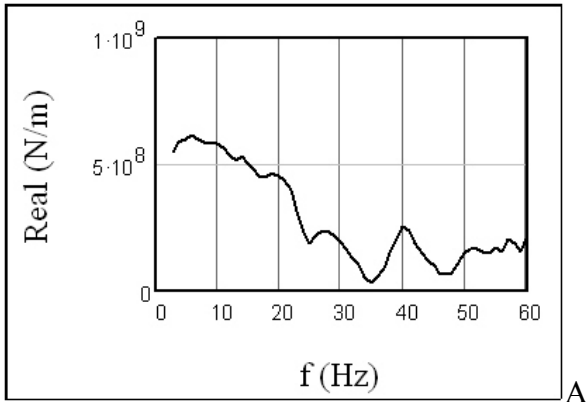


B

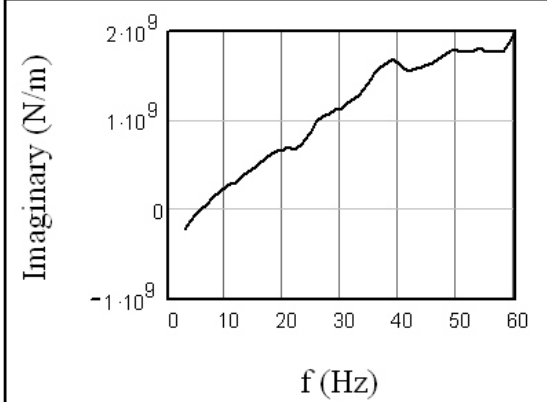


C

Figure 5-28. Thumper vertical results for Footing 6. A) Vertical Load. B) Vertical Displacement, Real Component. C) Vertical Displacement, Imaginary Component.



A



B

Figure 5-29. Thumper vertical results for Footing 6. A) Vertical Impedance, Real Component. B) Vertical Impedance, Imaginary Component.



Figure 5-30. Vertical Experiment with T-Rex shaker.



Figure 5-31. Vertical Experiment with T-Rex shaker.

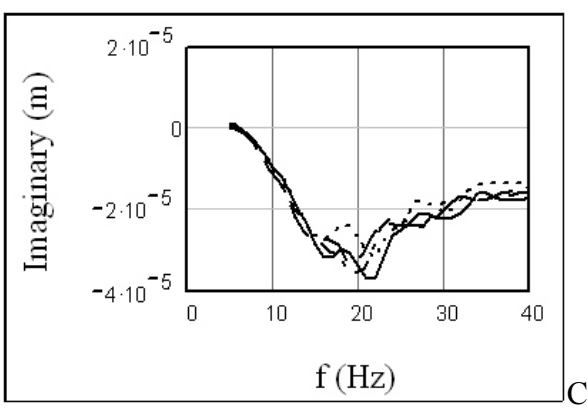
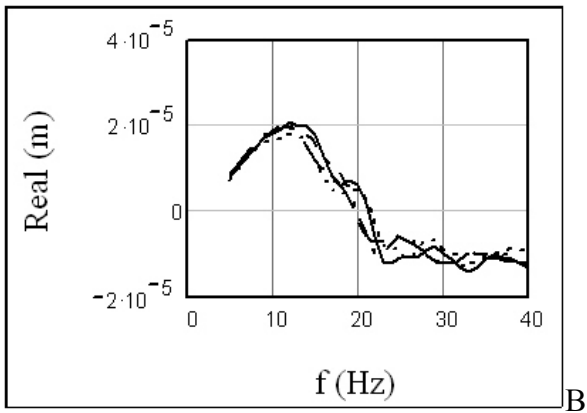
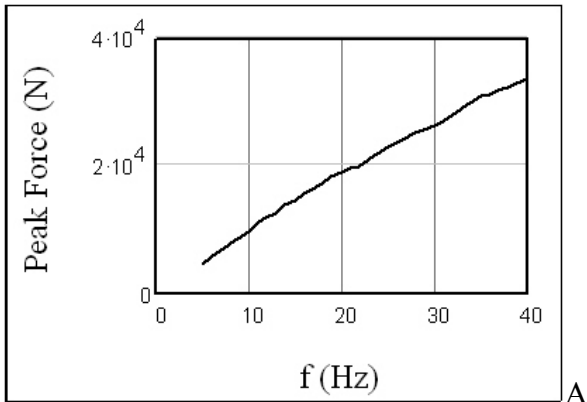


Figure 5-32. T-Rex vertical results for Footing 6. A) Vertical Load. B) Vertical Displacement, Real Component. C) Vertical Displacement, Imaginary Component.

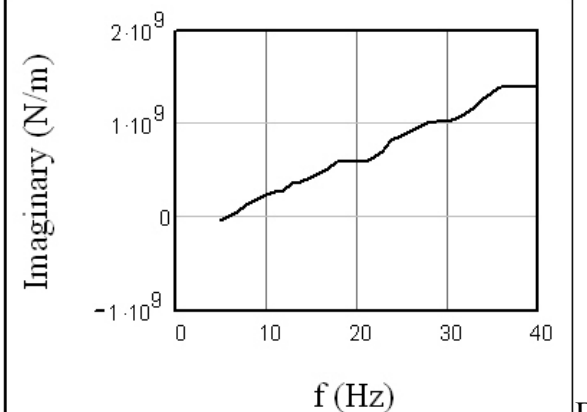
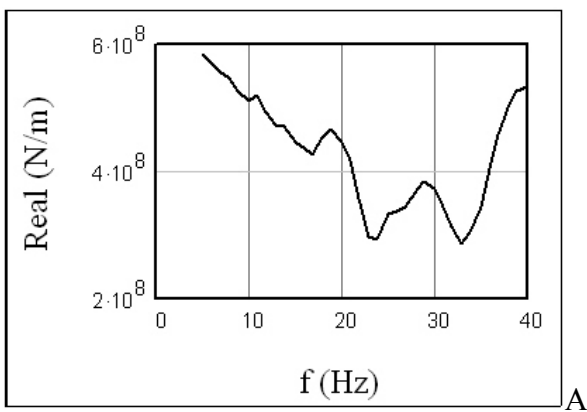


Figure 5-33. T-Rex vertical results for Footing 6. A) Vertical Impedance, Real Component. B) Vertical Impedance, Imaginary Component.



Figure 5-34. Horizontal Experiment for Footing 6 with Model MK-12 ANCO shaker mounted flush.



Figure 5-35. Horizontal Experiment for Footing 6 with Model MK-12 ANCO shaker on stand.

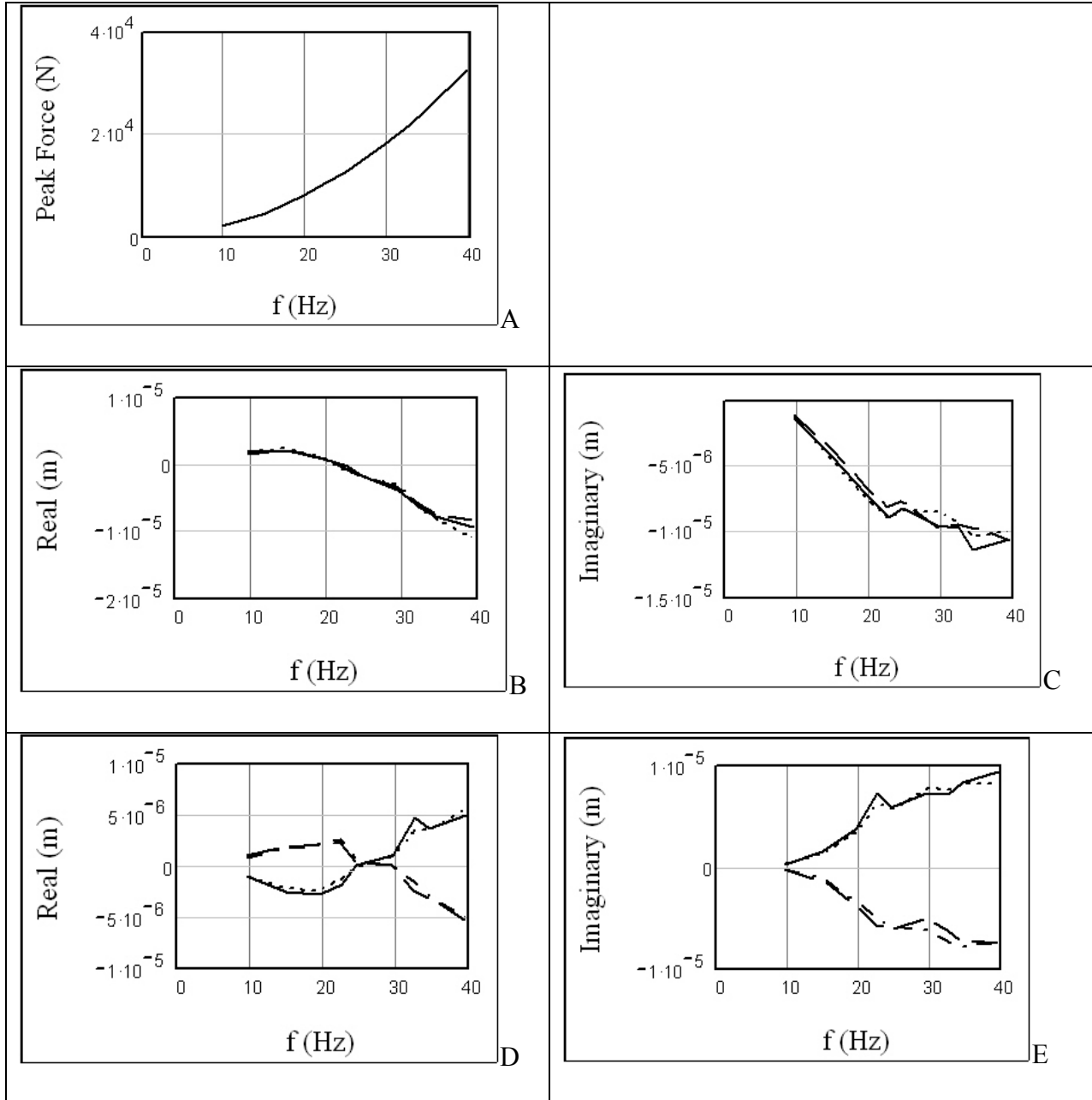


Figure 5-36. ANCO horizontal loading results for Footing 6 flush mounting. A) Horizontal Load. B) Horizontal Displacement, Real Component. C) Horizontal Displacement, Imaginary Component. D) Vertical Displacement, Real Component. F) Vertical Displacement, Imaginary Component.

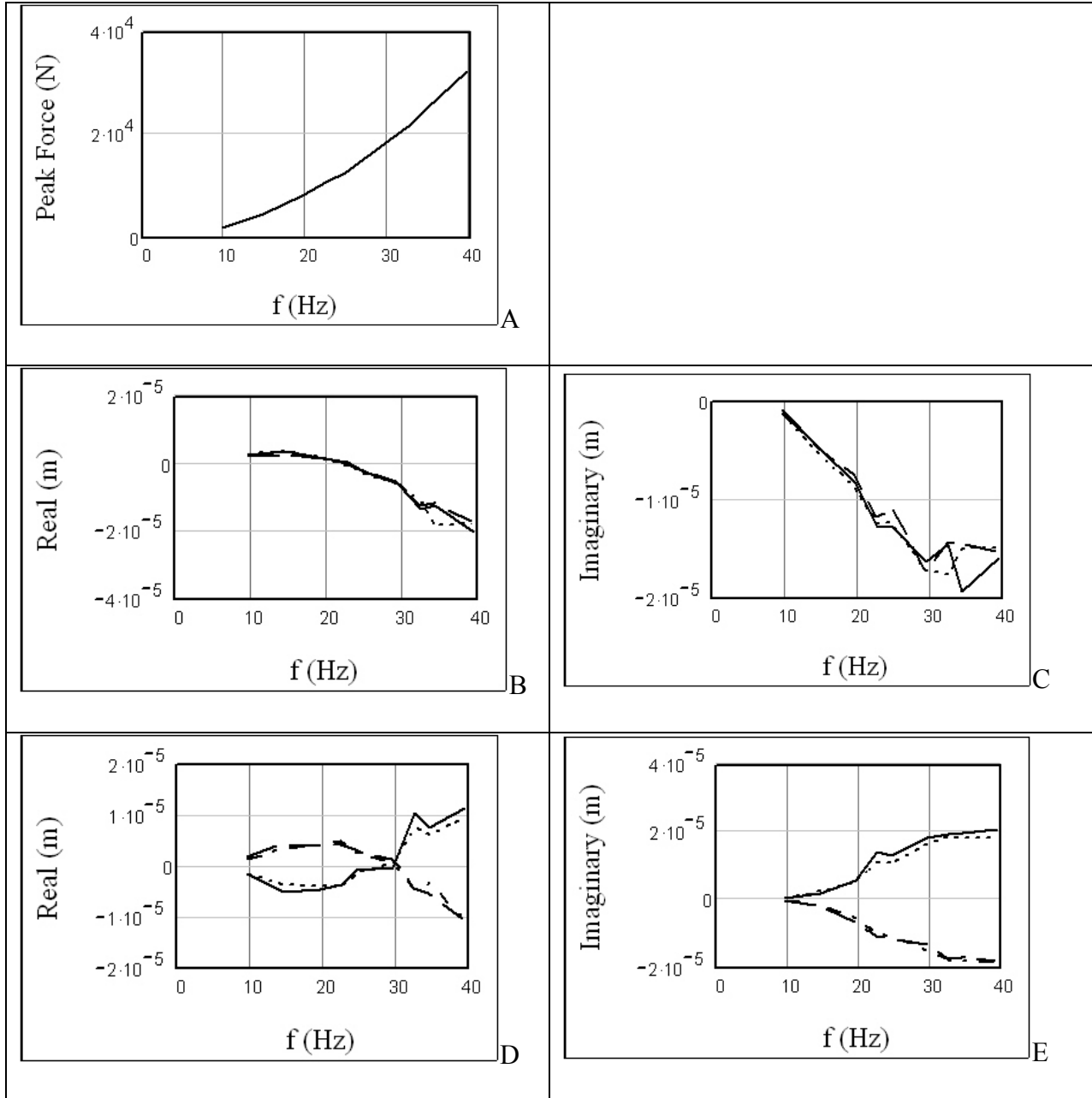


Figure 5-37. ANCO horizontal loading results for Footing 6 elevated mounting. A) Horizontal Load. B) Horizontal Displacement, Real Component. C) Horizontal Displacement, Imaginary Component. D) Vertical Displacement, Real Component. E) Vertical Displacement, Imaginary Component.

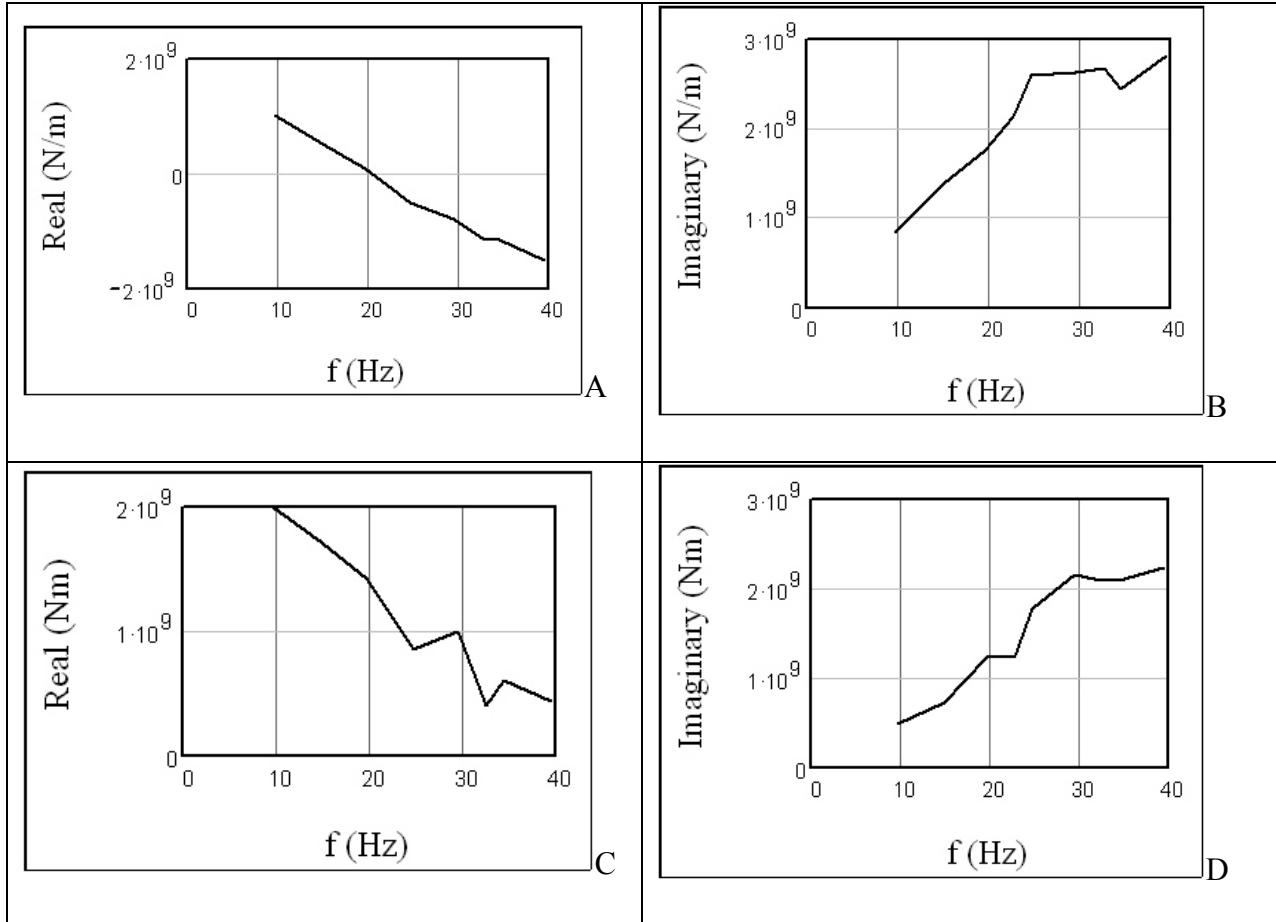


Figure 5-38. ANCO horizontal loading results for the one-degree-of-freedom analyses of Footing 6 flush mounting. A) Horizontal Impedance, Real Component. B) Horizontal Impedance, Imaginary Component. C) Rocking Impedance, Real Component. E) Rocking Impedance, Imaginary Component.

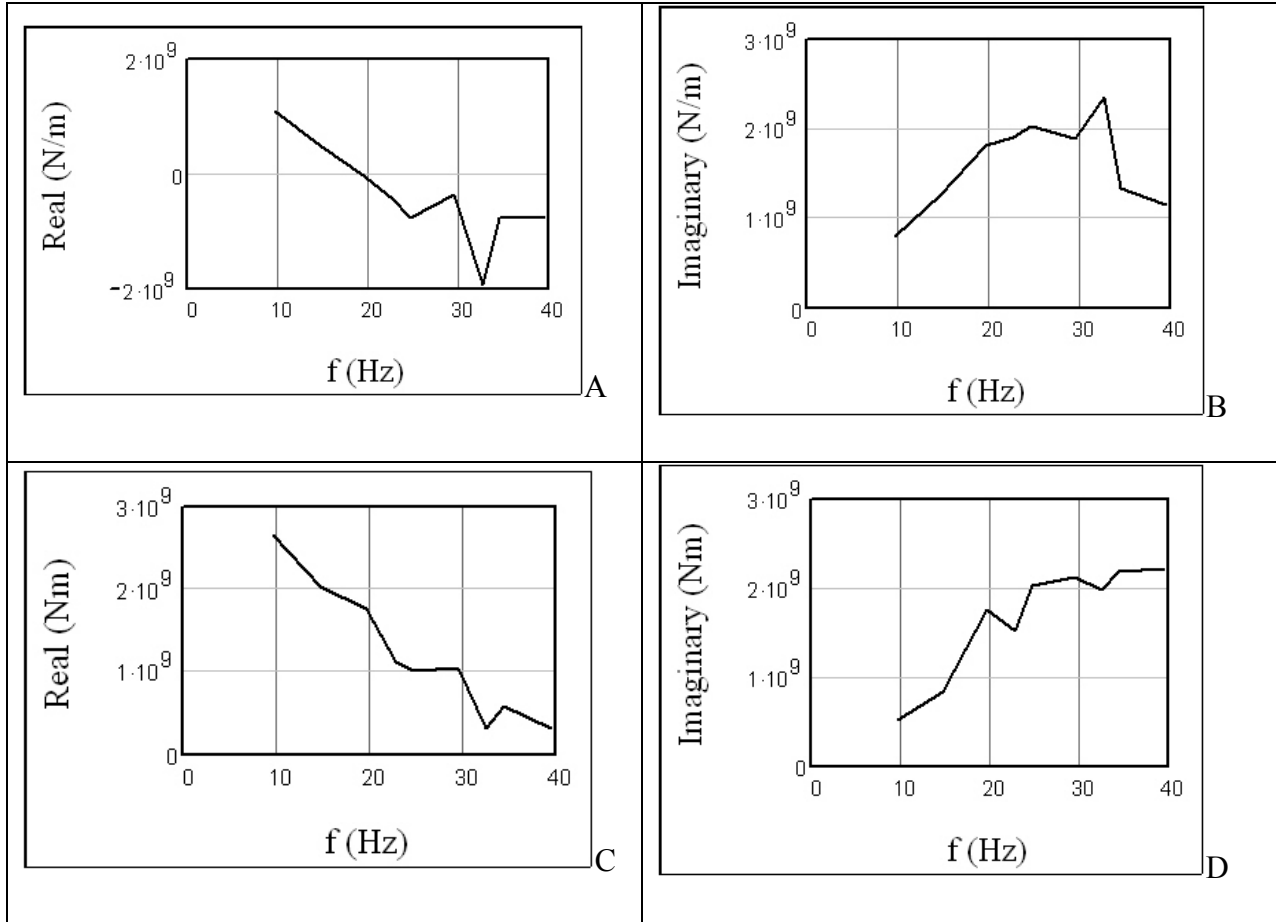


Figure 5-39. ANCO horizontal loading results for the one-degree-of-freedom analyses of Footing 6 elevated mounting. A) Horizontal Impedance, Real Component. B) Horizontal Impedance, Imaginary Component. C) Rocking Impedance, Real Component. D) Rocking Impedance, Imaginary Component.

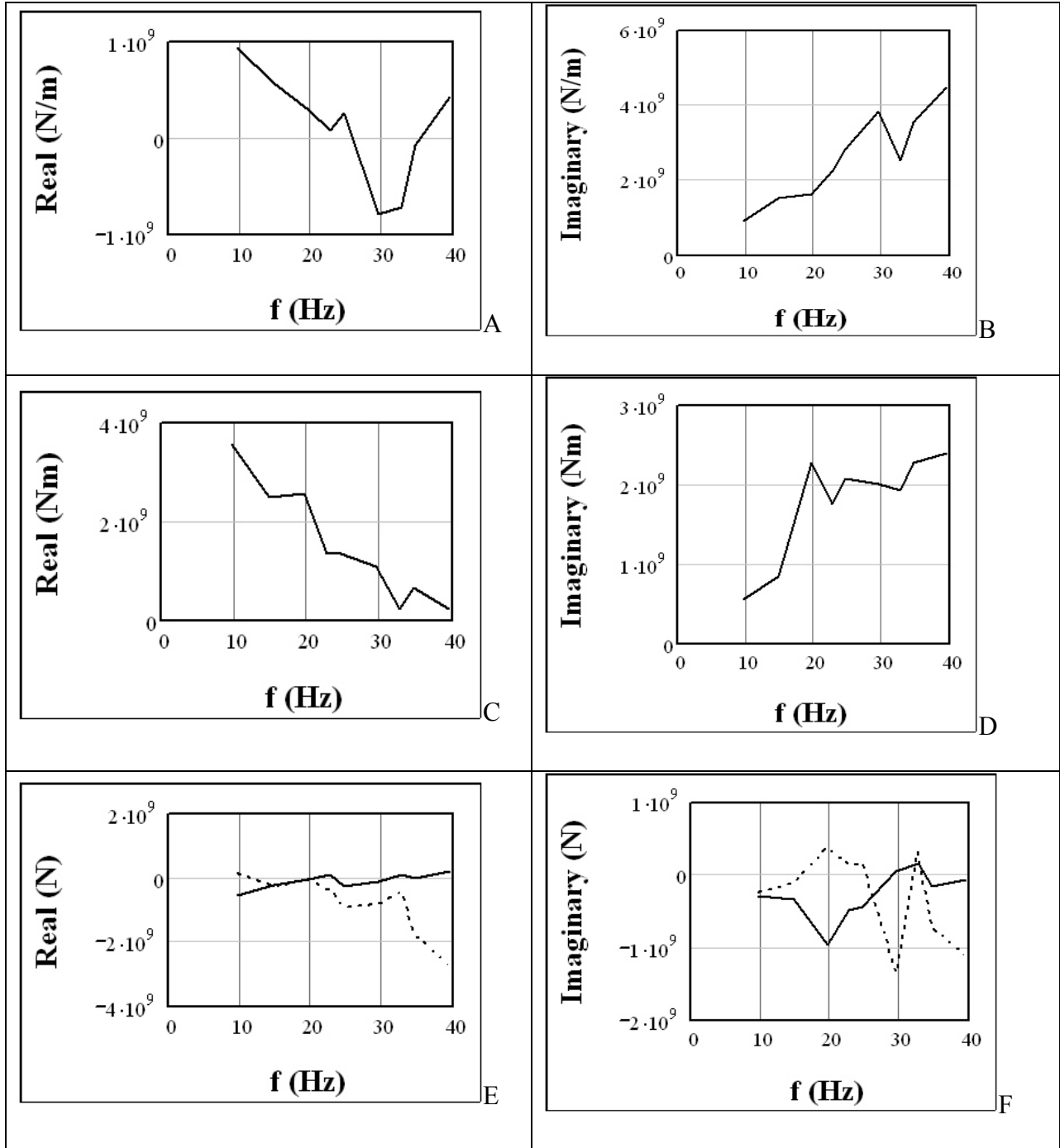


Figure 5-40. ANCO horizontal loading results for the non-equal coupling two-degree-of-freedom analyses of Footing 6. A) Horizontal Impedance, Real Component. B) Horizontal Impedance, Imaginary Component. C) Rocking Impedance, Real Component. D) Rocking Impedance, Imaginary Component. E) Coupling Impedance, Real Component. F) Coupling Impedance, Imaginary Component.

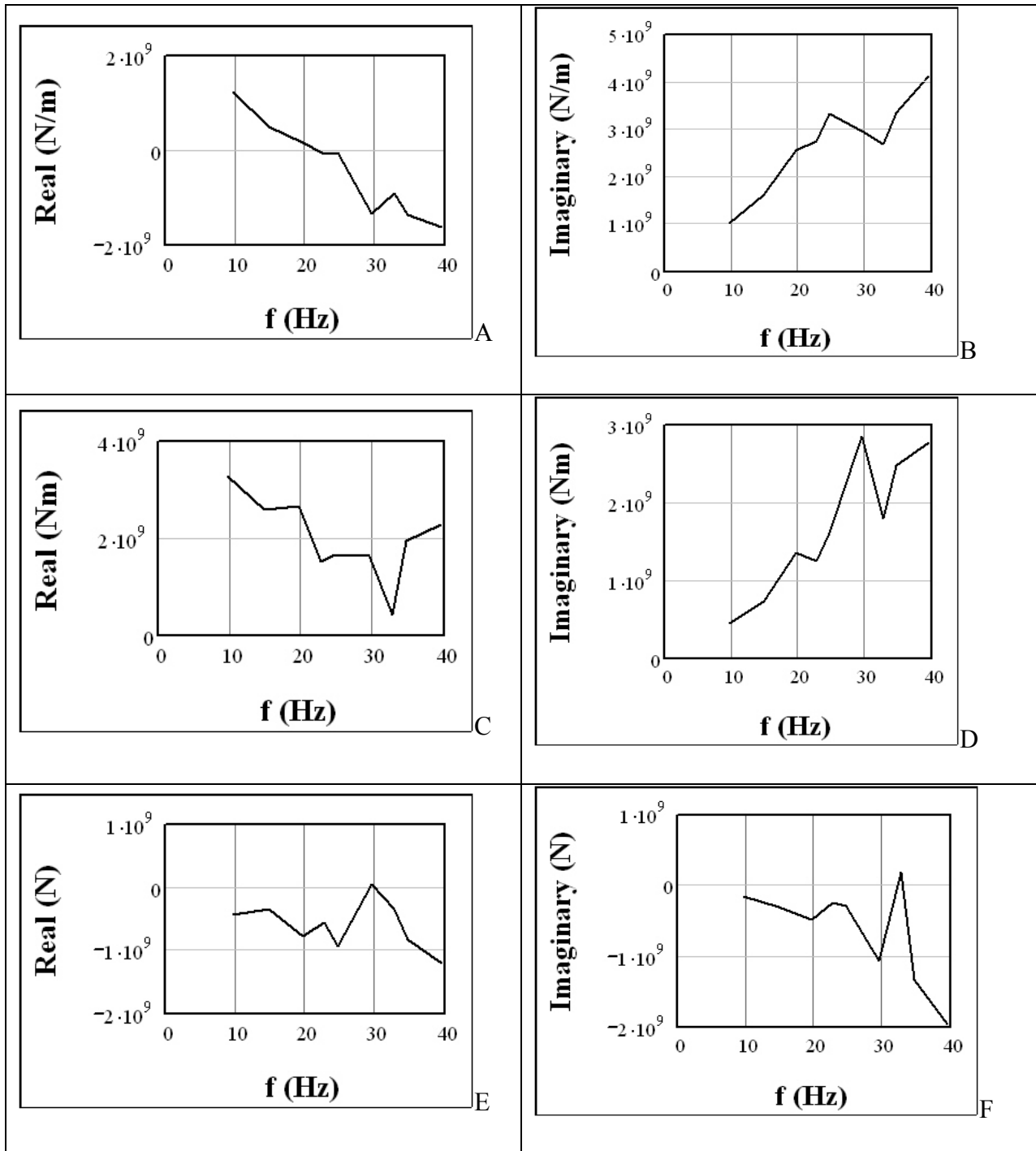


Figure 5-41. ANCO horizontal loading results for the equal coupling two-degree-of-freedom analyses of Footing 6. A) Horizontal Impedance, Real Component. B) Horizontal Impedance, Imaginary Component. C) Rocking Impedance, Real Component. D) Rocking Impedance, Imaginary Component. E) Coupling Impedance, Real Component. F) Coupling Impedance, Imaginary Component.

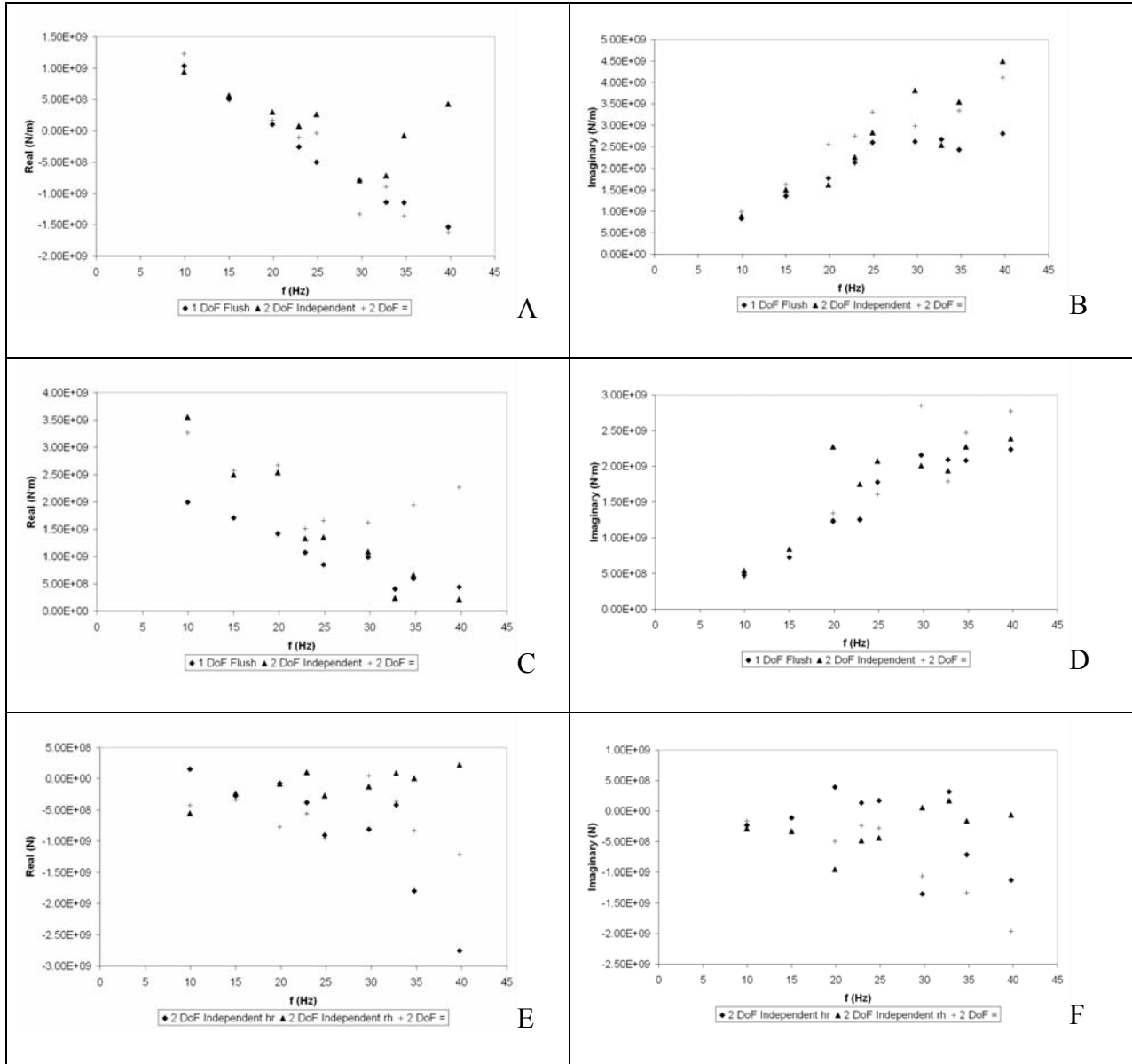


Figure 5-42. ANCO horizontal loading results for one-degree-of-freedom at flushed and elevated positions, independent coupling two-degree-of-freedom, and equal coupling two-degree-of-freedom analyses of Footing 6. A) Horizontal Impedance, Real Component. B) Horizontal Impedance, Imaginary Component. C) Rocking Impedance, Real Component. D) Rocking Impedance, Imaginary Component. E) Coupling Impedance, Real Component. F) Coupling Impedance, Imaginary Component.

## CHAPTER 6 IMPEDANCE FUNCTION COMPARISON AND ASSESSMENT

In-situ impedance functions were calculated for two shallow foundations as presented in Chapter 5. In Chapter 3, cone models demonstrated agreement with more rigorous prediction techniques. Predictions for the Foundations 5 and 6 were produced using the cone model executable program CONAN. Development of cone models and comparison of cone model predictions to in-situ results are presented in the following paragraphs.

### **6.1 Cone Model Development**

#### **6.1.1 Soil Profile**

Impedance function predictions were calculated via cone modeling. With accuracy suitable to represent other prediction techniques and relatively simple implementation, cone modeling was selected for comparison to measured in-situ values of impedance functions. The cone models required certain physical characteristics of the soil profile and foundation. Table 6-1 presents the properties of the soil surrounding Footings 5 and 6 utilized for CONAN predictions. The properties were either provided by, calculated from, or assumed based on results from Briard and Gibbens (1994), Tran and Hiltunen (2008) or testing performed primarily for impedance function research.

Layer interface depths were determined from a combination of information from Briard and Gibbens (1994) and Tran and Hiltunen (2008). At depths where parameters changed a layer interface was assumed. For example, Briard and Gibbens (1994) reported a soil density and friction angle change at a depth of 1.80 m thus, there a layer interface was determined to exist. The MASW survey provided by Tran and Hiltunen (2008) indicated at a depth of 8.38 m shear wave velocity changes which required a layer interface.

The shear modulus,  $G_s$ , was calculated as a function of shear wave velocity,  $c_s$ , and layer density,  $\rho$ , to form Equation 6-1. Shear wave velocity for each layer was determined via an MASW survey as described in Chapter 4. Soil density was reported by Briard and Gibbens (1994) for Layers 1 through 5 of Table 6-1. For Layers 6 and 7 no measured densities were available thus, soil density was assumed based on descriptions available from the boring logs of Briard and Gibbens (1994). The description of a very hard clay led to the assumption for density of  $1,886 \text{ kg/m}^3$ .

$$G_s = c_s^2 \rho \quad (6-1)$$

Poisson's Ratio was not available in Briard and Gibbens (1994), thus, as with density, this property was assumed based on borehole data. Layers 2 through 9 indicated medium dense sand with silt and clay content varying with depth; as a result a ratio of 0.333 was assumed. For Layers 10 and 11 a ratio of 0.45 is typical for hard clay below the water table.

Soil Damping was assumed to be 3 percent based on soil descriptions from Briard and Gibbens (1994) and typical values provided by Prakash and Puri (1988). This term indicates only mechanical energy losses in the soil as geometric damping is accounted for by the cone models. An investigation of the damping term was conducted to assess its effects on CONAN predicted impedance functions. Three additional damping values were inputted to CONAN with all other properties remaining constant. The resulting impedance functions varied slightly indicating material damping has a limited effect on cone model predictions for Footings 5 and 6.

### **6.1.2 CONAN Model**

Upon completion of a soil profile, the information was used to create CONAN input files. Some data was corrected due to differences between survey and test conditions. Table 6-2

presents CONAN input file data for the Footings 5 vertical input file. The input data represented here corresponds to testing performed using the Thumper shaker.

Seven physical properties were required for each layer of the cone models, the first being the layer type which is designated by one of four letters as follows: F indicates the free surface, L a finite layer, H a half-space, and R a perfectly rigid half-space. The bottom layer must be designated by either H or R.

For each layer, a radius was defined. Layers containing the foundation were assigned a non-zero radius and layers below the foundation were assigned a zero radius. It should be noted that though CONAN required a radius, it was not necessary for the foundation to be circular. The equivalent radius for a rectangular footing depended on its geometry and motion. For the radius of vertical and horizontal motion,  $r_{vh}$ , the area of the bottom of the foundation,  $A_f$ , was calculated. As presented in Equation 6-2, the footing area was then treated as a circular area for calculating the equivalent radius. For rocking motions the equivalent radius,  $r_r$ , was calculated much the same as with horizontal and vertical motions, the difference being that area moment of inertia  $\bar{I}_x$ , was used instead of area yielding Equation 6-3.

$$r_{vh} = \sqrt{\frac{A_f}{\pi}} \quad (6-2)$$

$$r_r = \sqrt[4]{\frac{4\bar{I}_x}{\pi}} \quad (6-3)$$

The shear modulus for each layer was corrected for the effects of increased effective stress experienced by the soil. The increase in effective stress was due to two factors of construction and testing. First, soil was removed and replaced with concrete which has a higher density thereby increasing the effective stress under the footings. Second, an increase in stress was experienced from equipment resting on the footings. The corrected vertical effective stress,  $\sigma'_{vc}$ ,

was calculated by first employing Boussinesq's solution of vertical stress at a point caused by a rectangular loaded area and adding it to the free field vertical effective stress,  $\sigma'_{\text{vff}}$ . The implementation of Boussinesq's solution for rectangular load areas is current standard practice though the footing is not rigid and the material is not homogeneous. Next, the at rest earth pressure coefficient,  $K_0$ , for sand layers and clay layers was calculated utilizing Equations 6-4 and 6-5 respectively. Horizontal effective stresses,  $\sigma'_h$ , for both before and after the stress increase were determined via Equation 6-6. The mean stress,  $\sigma'_0$ , was then calculated for free field and post loading arrangements as presented in Equation 6-7. A corrected shear wave velocity,  $V_{\text{sc}}$ , was computed utilizing the MASW free field velocity,  $V_{\text{sff}}$ ,  $\sigma'_{\text{off}}$ , and  $\sigma'_{\text{oc}}$  as in Equation 6-8. Finally, the corrected shear modulus,  $G_{\text{sc}}$ , was calculated via Equation 6-9.

$$K_{0\text{sand}} = 1 - \sin \phi \quad (6-4)$$

$$K_{0\text{clay}} = \frac{\nu}{1 - \nu} \quad (6-5)$$

$$\sigma'_h = K_0 \sigma'_v \quad (6-6)$$

$$\sigma'_0 = \frac{\sigma'_v + 2\sigma'_h}{3} \quad (6-7)$$

$$V_{\text{sc}} = \sqrt[4]{\frac{\sigma'_{\text{oc}}}{\sigma'_{\text{off}}}} \cdot V_{\text{sff}} \quad (6-8)$$

$$G_{\text{sc}} = V_{\text{sc}}^2 \cdot \rho \quad (6-9)$$

The next three layer properties were determined from Table 6-1. Poisson's Ratio, soil density, and damping were inserted directly into the CONAN input file with no corrected values necessary.

Finally thickness is required for any finite layer. The nine layer thicknesses required were determined by a combination of boring logs and MASW survey results. Layers not containing the foundation radius were simply calculated by subtracting the bottom depth of a layer from that of the layer above it. For layers containing the foundation, a maximum layer thickness,  $d$ , adjacent to the footing was required. Equation 6-10 determined layer thickness utilizing shear wave velocity,  $c_s$ , and the maximum angular velocity,  $\omega_{\max}$ , of the dynamic force to be imparted on the footing. In the case of foundation embedment depth being greater than the maximum allowable thickness, the soil around the foundation is separated into additional layers until Equation 6-10 is satisfied.

$$d \leq \frac{\pi c_s}{5\omega_{\max}} \quad (6-10)$$

Upon completing the model inputs, CONAN was run three separate times for each footing to calculate impedance functions for vertical, horizontal, and rocking. Additionally, coupling terms were calculated with the rocking mode. Depending on the mode of excitation the appropriate radius was used. Impedance functions were produced for a specified range of frequency. For Footing 5, impedance functions were calculated from 8 Hz to 50 Hz at a 1 Hz interval. Footing 6 impedance functions were calculated for frequencies ranging from 10 Hz to 40 Hz at a 1 Hz interval.

Table 6-3 contains CONAN input data for Footing 6 horizontal testing. The input file corresponds to the test configuration performed with the ANCO shaker elevated. It was developed in the same manner as the input file of table 6-2.

## 6.2 Cone Model and Measured Impedance Function Comparison

### 6.2.1 Footing 5

Cone model vertical impedance solutions are compared to the experimental results for Footing 5. Figure 6-1 represents the real value in A, the imaginary value in B, and the dashpot coefficient, or viscous damping, in C. The dashpot coefficient was simply calculated by dividing the imaginary component by  $\omega$  thereby removing the frequency effect. Each plot contains values for testing using the ANCO shaker indicated by points and values predicted by CONAN represented by the curve.

Predicted and measured impedance functions and dashpot coefficients exhibit fairly good agreement. With the exception of peaks in the vicinity of the resonance at 25 Hz, magnitudes plot well within an order of magnitude of each other. An important characteristic of Figure 6-1 B is predicted values plotting lower though exceptions exist at high and low frequencies. Predicted and measured real values both demonstrate a decrease with respect to frequency. The decrease is noticeably more extreme in measured values. Imaginary values reveal an increase with frequency and predicted and measured trends agree somewhat well, the peak at 25 Hz being the largest difference. Figure 6-1 C demonstrates much of the same agreement and many of the exceptions noticed in A and B. Values are within a magnitude of each other with the peak near 25 Hz being the greatest exception. Predicted and measured dashpots tend to be constant regardless of frequency. This is consistent with dashpot plots for square footings found in Gazetas (1991).

Figure 6-2 through Figure 6-4 graph the real and imaginary components and dashpot coefficients for Footing 5 horizontal testing using the Electro-Seis shaker positioned at 2 ft and 4 ft. Cone model predictions are presented for horizontal, rocking, and coupling terms. Measured values include the one-degree-of-freedom solution at 4 ft, and two two-degree-of-freedom

solutions for horizontal and rocking modes. Independent and equal cross-coupling terms are included for measured values in Figure 6-4.

To a lesser extent than the vertical mode and with the exception of the one-degree-of-freedom solution, measured impedance functions demonstrate some agreement with horizontal cone model predictions via comparable magnitudes in Figure 6-2. They are separated by much less than a factor of ten. It should be noted, both real and imaginary values are consistently predicted low when compared to the two-degree-of-freedom model. A positive aspect is that measured value trends possess similar slopes to predicted values until frequencies begin experiencing resonance effects at 28 Hz. Again as expected, negative and positive slopes are observed in the real and imaginary plots respectively. When looking at damping, an increase in slope of the measured values is noticeable while the predicted curve remains generally straight causing a much greater difference in damping values at higher frequencies. Dashpot coefficients seem to possess characteristics of the Gazetas (1991) graphs. Predicted and measured trends remain constant with a change in frequency until approximately 28 Hz which is near resonance.

Figure 6-3 A and B present the real and imaginary values for predicted and measured rocking impedance functions. They compare much the same as the horizontal impedance functions though, in this case the real two-degree-of-freedom independent solution seems to be the exception instead of the one-degree-of-freedom solution. The magnitudes of values for real and imaginary are within a factor of ten but, as with horizontal, cone models under predict impedance functions. As for curve shapes, measured trend slopes and predicted slopes seem to be agreement. The real one-degree-of-freedom and real two-degree-of-freedom over-determined measured values demonstrate a negative slope which is expected. The imaginary values behave as expected with positive slopes and generally agree with one another until 28 Hz which is

approaching resonance. Plot C presents dashpot coefficients that agree somewhat with Gazetas (1991) plots for rocking dashpot coefficients. Values are noticeably higher at the lowest frequencies for predicted values but eventually become constant. Measured values demonstrate a trend with a gradually diminishing negative slope. Though differing from each other, predicted and measured behavior both possess characteristics of the Gazetas (1991) plots.

Figure 6-4 A, B, C, and D present the real and imaginary values for predicted and measured coupling impedance functions. Figures 6-4 C and D contain the same data as A and B, but have been altered to focus on the predicted, one-degree-of-freedom, and independent two-degree-of-freedom. As observed in A and B the over-determined two-degree-of-freedom values were much larger than the others, thus did not compare well with predicted, one-degree-of-freedom, and over-determined two-degree-of-freedom value. Studying Figure 6-4 C and D magnitudes for real components are fairly similar and for imaginary components the similarity is more noticeable. Predicted and measured values are within a factor of ten of each other, the exceptions being at high frequencies for both real and imaginary values. Predictions seem to be higher for real values but, when observing imaginary values lower in the low frequency range. Real values demonstrate a drop with an increase in frequency for both predicted and measured values, though the measured values demonstrate a much steeper drop. The severity of the rate of this drop increases with frequency. Imaginary values for predicted and measured impedances possess a similar slope until reaching 28 Hz. Figure 6-4 E and F are treated much the same as the previous plots by shifting focus from the independent two-degree-of-freedom dashpot values. Studying F it should be noted that predictions are lower with the exception of high frequencies. All three dashpots are well within a magnitude of each other. Their trends with respect to

frequency are also similar exhibiting a constant value with increased frequency until approximately 28 Hz.

### **6.2.2 Footing 6**

Cone model vertical impedance solutions are compared to the experimental results for Footing 6. Figure 6-5 represents the real value in A, the imaginary value in B, and the dashpot coefficient, or viscous damping, in C. The dashpot coefficient was calculated by dividing the imaginary component by  $\omega$  thereby removing the frequency effect. Each plot contains values for testing using the Thumper and T-Rex shakers indicated by points and values predicted by CONAN represented by the curves.

Predicted and measured impedance functions and dashpot coefficients demonstrate fairly good agreement for real values and good agreement for imaginary values. Real and imaginary values plot within a magnitude of each other. The measured real component for Thumper agrees well with its corresponding predictions at low frequency before becoming consistently lower. T-Rex measured real values are consistently low but remain comparable to predicted values. The imaginary component of both Thumper and T-Rex compare very well with their respective predictions though slightly low. When observing trends with respect to frequency, Thumper drops as frequency increases though predicted values tend to drop until approximately 10 Hz and slightly rise thereafter. T-Rex demonstrates agreement with predicted values dropping slightly at low frequencies then beginning to rise in the higher frequency ranges. Imaginary components exhibit good agreement between predicted and measured values. The slopes of the curve and trend lines are in the same direction and seem to increase with frequency at the same rate. Figure 6-5 C demonstrates much of the same agreement and many of the exceptions noticed in B. Values are within a magnitude of each other. Predicted and measured dashpots seem to approach

zero at low frequencies and become constant at high frequencies. This is consistent with dashpot plots for square footings found in Gazetas (1991).

Figure 6-6 through Figure 6-8 present the real and imaginary components and dashpot coefficients for Footing 6 horizontal testing using the ANCO shaker positioned flush to the footing surface and elevated on a frame. Cone model predictions are presented for horizontal, rocking, and coupling terms. Measured values include the one-degree-of-freedom solution with the shaker flush, and two two-degree-of-freedom solutions for horizontal and rocking modes. Independent and equal cross-coupling terms are included for measured values in Figure 6-8.

Though not as strong as the vertical mode, measured impedance functions demonstrate some agreement with horizontal cone model predictions via comparable magnitudes in Figure 6-6. Values are separated by much less than a factor of ten. It should be noted, the real component is slightly higher at low frequency than predicted values but, imaginary values are consistently predicted low when compared to all three solutions. The decrease of real values with respect to frequency is also significant. Predicted real values do not decrease as sharply as those measured. A similar but opposite relationship is apparent when observing the imaginary components. Predicted values possess a positive slope but the trend of measured values is to rise more sharply with respect to frequency. Figure 6-6 C reveals dashpots that are somewhat consistent with each other and with Gazetas (1991). The coefficients appear to maintain a constant value with regard to frequency and plots found in Gazetas (1991). The cone predictions, however, are significantly lower than the measured values.

Figure 6-7 A and B present the real and imaginary values for predicted and measured rocking impedance functions and demonstrate some agreement between the two. The magnitudes of values for real and imaginary are within a factor of ten. The real predicted curve

is observed lying near the median of the one-degree-of-freedom and independent two-degree-of-freedom real components and within a magnitude of the over-determined two-degree-of-freedom real components. Again, the cone model predictions are consistently lower than the measured values. Measured trend slopes and predicted slopes seem to be in some agreement. Real components for predicted and measured values decrease with an increase in frequency, though measured values tend decrease at a higher rate. The over-determined two-degree-of-freedom values begin to rise at 30 Hz. The imaginary component rises at a similar but slower rate with respect to frequency. Plot C presents dashpot coefficients. Dashpot coefficients are noticeably lower at the lowest frequencies for predicted values but eventually become constant. Measured values demonstrate a trend with a gradually diminishing positive slope. Again, the cone model predictions are consistently lower than the measured values.

Figure 6-8 A and B present the real and imaginary values for predicted and measured coupling impedance functions. Both real and imaginary components are predicted high with few exceptions. Many measured real values seem to plot erratically with some points falling close to the predicted curve and others falling more than a magnitude away. Of the three measured real components, the independent two-degree-of-freedom  $r_h$  values seem to match the predicted curve the best. The measured imaginary components seem to compare only slightly better than the real. While some values fall near the predicted curve many fall close to a magnitude away. Again the independent two-degree-of-freedom  $r_h$  values seem to match the curve best. Predicted real component changes with respect to frequency exhibit a slight similarity to measured values but, seem to not match well. The predicted values plot nearly horizontal while measured values seem to drop more severely with respect to frequency. Predicted imaginary values seem to rise with increased frequency which contrasts to measured values falling. Observing C, the predicted

dashpot rises slightly at low frequencies then begins to become constant at higher frequencies. The measured values seem erratic and possess very little apparent shape or trend.

In summary, it would appear measured impedance functions compare fairly well to cone predicted impedance functions in many aspects according to the plots in this section, but there are exceptions. Perhaps the two most important differences between predicted and measured impedances are the consistent under prediction of damping and the sharp decrease of measured real values demonstrated with Footing 6. The under prediction is noticeable in multiple modes, both footings, and varying severities. As for the drop in measured stiffness compared to predicted, this phenomenon is also recognized in multiple modes, both footings, and a variety of severities. Positive characteristics are observed with respect to the magnitude of both predicted and measured values. Nearly all the plots present comparisons that are within the same magnitude. When studying differences between the two footings, the most noticeable is in stiffness. Footing 5 measured value trends seem to share a somewhat common slope with predicted curves while in most cases significantly under predicting the magnitudes. Footing 6 stiffness predictions demonstrate the opposite by being fairly accurate with respect to magnitude while not displaying the severe drop with respect to frequency. Expected differences between the footings outlined in Gazetas (1991) were noticed. For example, the stiffness of Footing 6 is larger than that of 5 which is consistent with their difference in size. Another difference is the quality of the coupling data. Gazetas (1991) states that as the depth-width ratio increases the coupling term should increase. Footing 5 has a significantly larger depth-width ratio and also demonstrates a better comparison in coupling terms than Footing 6. Observing differences between modes, vertical impedance function predictions appear to match measured values more than horizontal, rocking, and coupled predictions. Much of the behavior exhibited by measured

and predicted impedance functions were consistent with what was generally expected from Gazetas (1991).

### **6.3 Assessment**

Noticeable differences appear in the comparison between predicted and measured values. It is necessary to address these inconsistencies as they are observed in both footings, in all modes, and are of many degrees of severity. It seems appropriate to approach these differences in three categories, measurement error, prediction parameter accuracy, and cone model assumptions. The following paragraphs discuss potential reasons for these inconsistencies in each of the three stated categories.

#### **6.3.1 Measurement Error**

To study the effects of systematic bias on measured impedance functions, Figures 6-9 through 6-12 present measured impedance functions with 5% bias added to all voltages read during testing. It was determined that an error band of artificial error deemed larger than reasonably expected would indicate potential measurement error if it encompassed a large percentage predicted values on a plot. Voltages from the load cell were increased by 5% and decreased by 5% to calculate the +5% and -5% impedance values respectively. Similarly, the velocity transducer voltages are decreased by 5% and increased by 5% to calculate +5% and -5% impedance values respectively. Adjusting all voltages by 5% more than accounts for equipment manufacturer's stated error. Also, adjusting load cell and transducer values in opposite directions produces the largest discrepancy between unadjusted and adjusted values.

Observing each error plot, it seems clear that predicted impedance function values rarely fall within the error band of the measured values. In instances that predicted curves cross into the error band it appears attributable to the measured values possessing a trend that crosses the curves at few frequencies then proceeds on its steep change. A few error bands may contain

predicted curves for a frequency range of up to 15 Hz, but this appears to be coincidental with a majority of the predicted curve lying significantly outside the error bands. After accounting for potential error that was determined to be large, it seems unlikely that measurement error from testing or calculation is sufficient to explain the differences between measured and predicted impedance functions.

### **6.3.2 Prediction Parameters**

The second potential source for the differences between measured and predicted values may be found in the cone model soil profile parameters. Errors due to input parameters were likely minimized through thorough characterization of the site. Many parameters have been measured well and, in cases where assumptions were necessary, input values possessed limited influence on predictions. A parametric assessment was made to determine the influence that input values had on cone models. Modeling parameters were varied and predictions made via CONAN as part of a sensitivity analysis. These predictions were compared to cone models produced with unadjusted values and the significance of each parameter was assessed.

The comparison demonstrated a narrow change in impedance functions corresponding to relatively large variations in most parameters. In fact, changes in Poisson's ratio, material damping, and soil density produced minimal differences when compared to unadjusted predictions. Typical differences were significantly less dramatic than those seen in the measurement error bands of Section 6.3.1. The largest influence seemed to be that of the shear modulus. The calculation of shear modulus utilizes soil density and shear wave velocity. Though density is easily measured or assumed with a fair degree of accuracy, characterization of the shear wave velocity required complex geophysical tests. For the calculation of shear modulus, surface wave analysis and crosshole surveys were conducted. The results of each survey allowed for the calculation of a set of impedance function predictions. Crosshole over

predicted impedance functions significantly whereas MASW produced more accurate results. Based upon these findings, cone model impedance function predictions employing MASW were deemed more suitable than those of crosshole testing and thus, represented predicted values when compared to measured values. Inconsistencies between predicted and measured impedance functions do not appear to result from material parameters inserted into the cone model.

### **6.3.3 Model Assumptions**

The third potential source for differences may be found in cone modeling assumptions. Multiple factors may account for inconsistencies, among the most obvious seem to be the assumptions of a wave increasing its size via a one dimensional cone and one wave type being propagated. In reality, waves do not spread in a cone, but instead in all directions. The cone may only account for a limited dissipation of energy due to geometric influences not accounting for lateral dissipation. Also, many wave types emanate from the foundation. For example, vertical and rocking modes account for only P-wave behavior when calculating the wave front of the cone. Displacement in these directions may primarily cause P-waves by pushing into the supporting soil but, the side of the footing also displaces in shear with respect to the soil which is neglect by the cone models. Similarly, though shear waves may be the primary waves experienced in predicting horizontal motion, compression waves are created between the vertical soil-footing interface as well as horizontal shear waves that go un-accounted for. In fact these phenomena may increase significantly with an increase in the depth width ratio. To truly capture the dynamic behavior of the system it seems that Rayleigh, shear, and compression waves need to be included in any model. Soil homogeneity may be an inaccurate assumption. Cone models assume a layer's material properties are consistent throughout when, in fact, that is rarely if ever the case. There exists stress strain variability induced solely by the depth a material occupies

meaning the composition of a material may be consistent but its depth in the layer may influence its behavior. Lateral variation is not accounted for when using cone models. Layer assumptions may influence cone model accuracy. CONAN assumes the only variation in the model exists at perfectly flat infinite layer interfaces. This assumption is rarely accurate in practice.

Characteristics such as voids, trenches, adjacent structures etc. potentially influence cone model accuracy. It appears likely that fundamental shortcomings in cone model assumptions may explain the differences between measured and cone predicted impedance functions.

Cone models appear to lack the ability to predict impedance functions with a high degree of accuracy in complex three dimensional problems. Vertical cone model predictions tend to characterize the impedance functions of the two available footings fairly well by presenting curves that match measured values in magnitude, shape, and slope. To a lesser extent, horizontal and rocking impedance function predictions seem to possess a relationship with measured values by demonstrating similar magnitudes, slopes, and shapes. Coupling terms demonstrate some similarities to measured values though seem dependent on a higher depth-width ratio. Inconsistencies do not seem to be caused by measurement error or parametric assessments; rather, they appear to be the result of cone model assumptions that do not accurately reflect conditions and behaviors typically experienced in the field. Based upon the apparent shortcomings of cone models, it seems an approach capable of addressing these more complicated wave propagation problems is necessary to more accurately predict impedance functions.

Table 6-1. Free Field Soil Properties for Footing 5 and Footing 6.

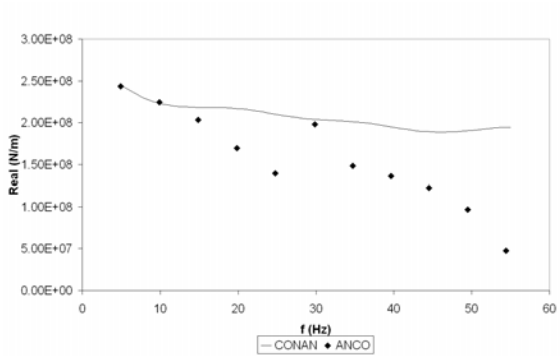
Layer No.	Layer Interface Depth (m)	MASW Shear Wave Velocity (ft/s)	Shear Modulus (Pa)	Poisson's Ratio	Density (kg/m <sup>3</sup> )	Damping (%)
1	1.52	438	2.775E+07	0.333	1558	0.03
2	1.80	712	7.332E+07	0.333	1558	0.03
3	4.91	712	7.506E+07	0.333	1595	0.03
4	8.38	712	9.167E+07	0.333	1948	0.03
5	10.52	999	1.805E+08	0.333	1948	0.03
6	13.72	999	1.747E+08	0.333	1886	0.03
7	Half Space	1344	3.162E+08	0.333	1886	0.03

Table 6-2. CONAN Input File for Footing 5 Vertical Model.

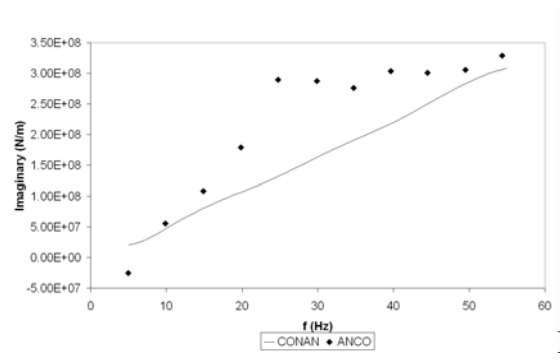
Layer Type	Foundation Radius (m)	Corrected Shear Modulus (Pa)	Poisson's Ratio	Density (kg/m <sup>3</sup> )	Damping (%)	Thickness (m)
F	0.559					
L	0.559	2.77E+07	0.333	1558	0.03	0.237
L	0.559	2.77E+07	0.333	1558	0.03	0.237
L	0.559	2.77E+07	0.333	1558	0.03	0.237
L	0	4.32E+07	0.333	1558	0.03	0.813
L	0	8.10E+07	0.333	1558	0.03	0.274
L	0	7.58E+07	0.333	1595	0.03	3.109
L	0	9.18E+07	0.333	1948	0.03	3.475
L	0	1.81E+08	0.333	1948	0.03	2.134
L	0	1.75E+08	0.450	1886	0.03	3.2
H	0	3.16E+08	0.450	1886	0.03	

Table 6-3. CONAN Input File for Footing 6 Horizontal and Rotational Model.

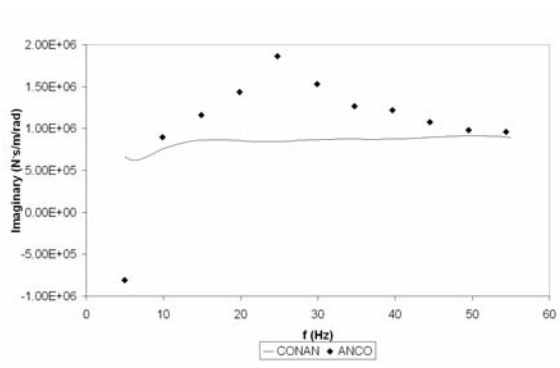
Layer Type	Foundation Radius (m)	Corrected Shear Modulus (Pa)	Poisson's Ratio	Density (kg/m <sup>3</sup> )	Damping (%)	Thickness (m)
F	1.74					
L	1.74	2.77E+07	0.333	1558	0.03	0.304804
L	1.74	2.77E+07	0.333	1558	0.03	0.304804
L	1.74	2.77E+07	0.333	1558	0.03	0.304804
L	0	3.26E+07	0.333	1558	0.03	0.609589
L	0	8.24E+07	0.333	1558	0.03	0.274
L	0	7.73E+07	0.333	1595	0.03	3.109
L	0	9.21E+07	0.333	1948	0.03	3.475
L	0	1.81E+08	0.333	1948	0.03	2.134
L	0	1.75E+08	0.45	1886	0.03	3.2
H	0	3.16E+08	0.45	1886	0.03	



A



B



C

Figure 6-1. ANCO vertical comparison for Footing 5. A) Vertical Impedance, Real Component. B) Vertical Impedance, Imaginary Component. C) Vertical Dashpot Coefficient.

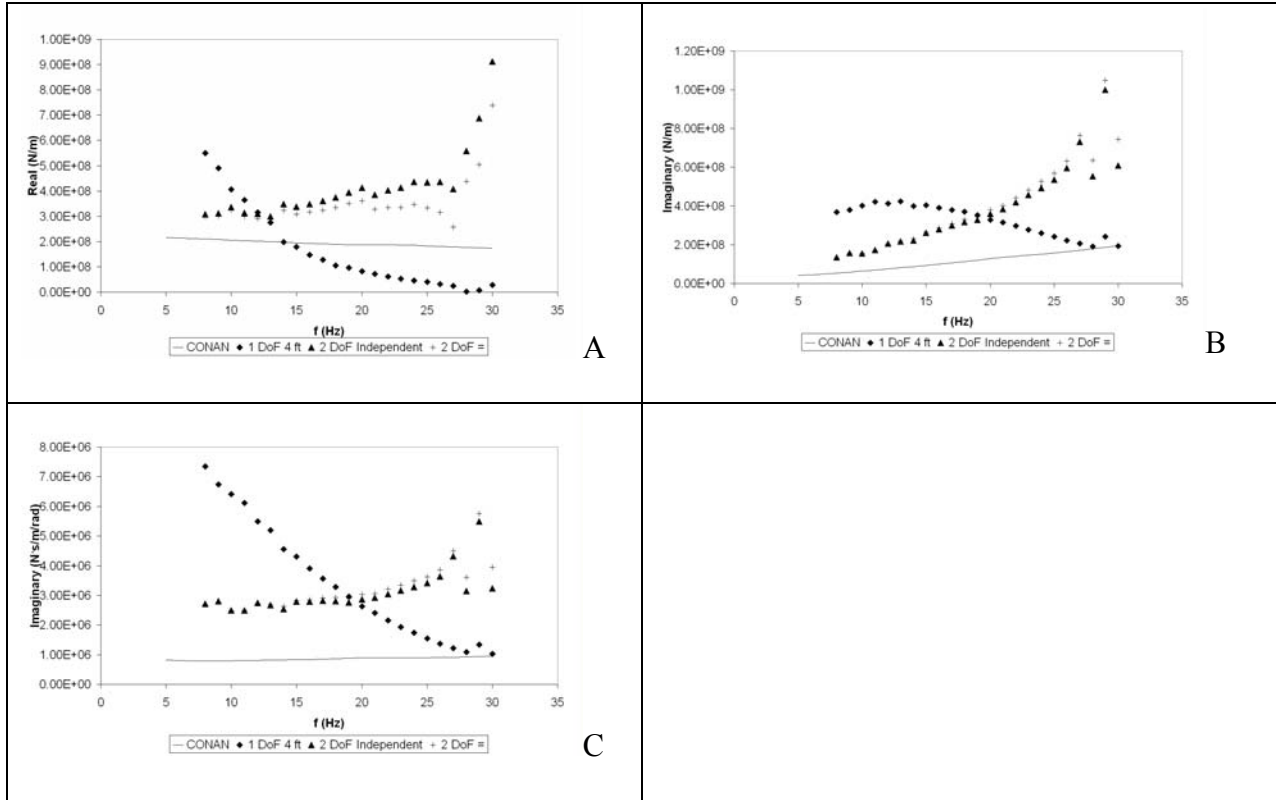


Figure 6-2. Electro-Seis horizontal comparison for the one-degree-of-freedom at 4 ft, independent coupling two-degree-of-freedom at 2 ft and 4 ft, the equal coupling two-degree-of-freedom analyses of Footing 5 at elevations 2 ft and 4 ft. A) Horizontal Impedance, Real Component. B) Horizontal Impedance, Imaginary Component. C) Horizontal Dashpot Coefficient.

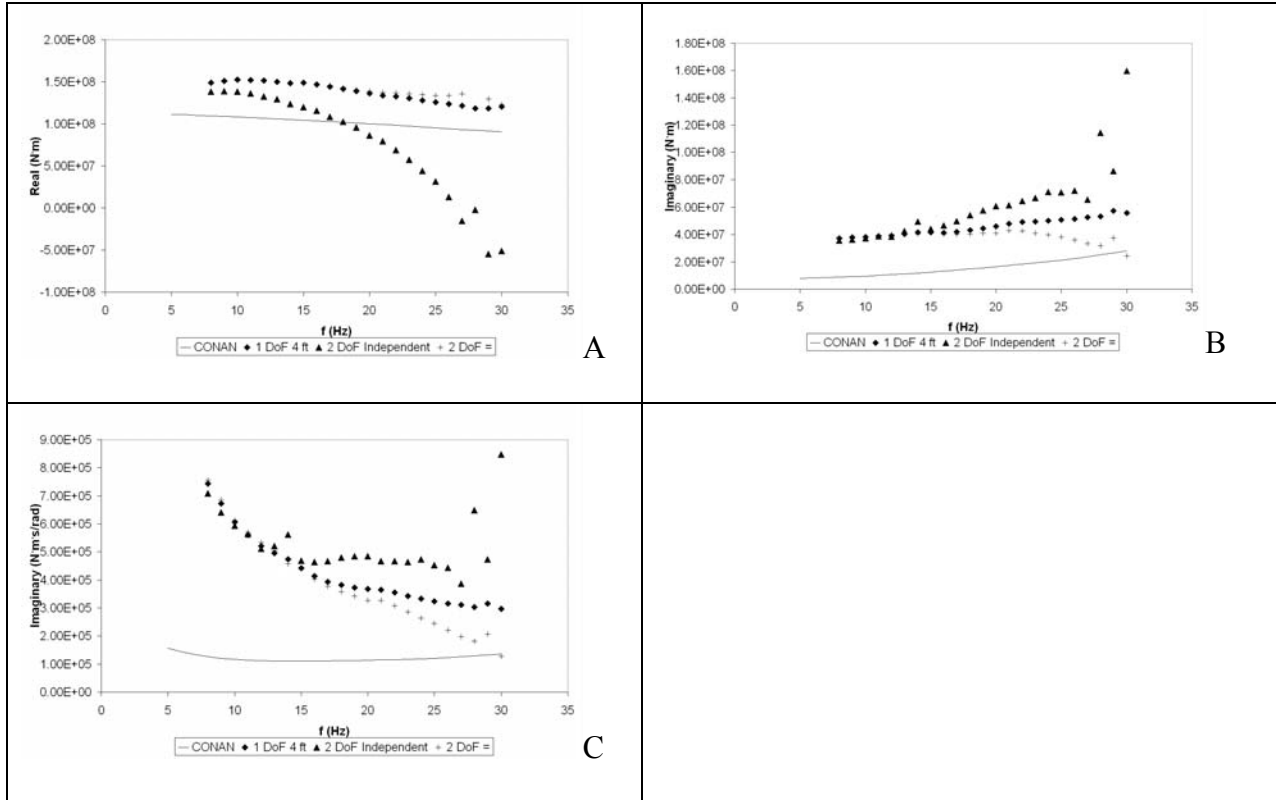


Figure 6-3. Electro-Seis horizontal comparison for the one-degree-of-freedom at 4 ft, independent coupling two-degree-of-freedom at 2 ft and 4 ft, the equal coupling two-degree-of-freedom analyses of Footing 5 at elevations 2 ft and 4 ft. A) Rocking Impedance, Real Component. B) Rocking Impedance, Imaginary Component. C) Rocking Dashpot Coefficient.

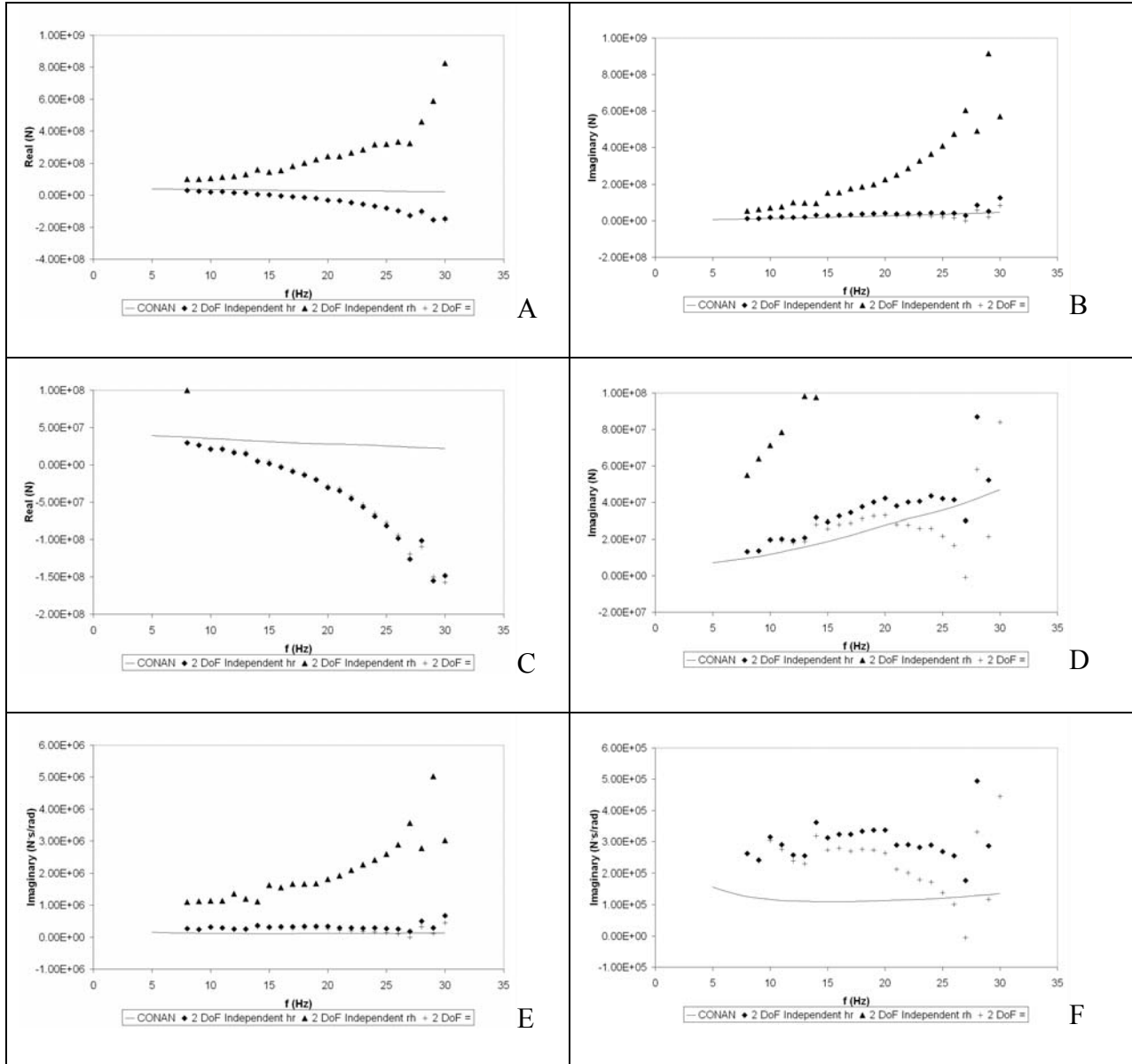
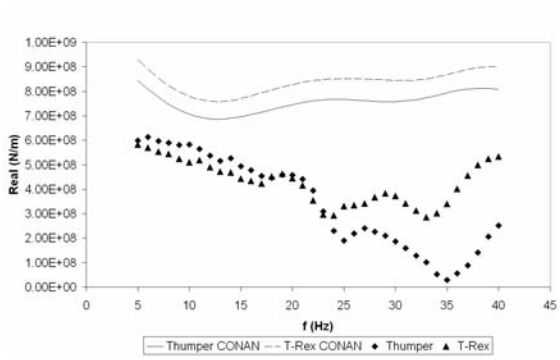
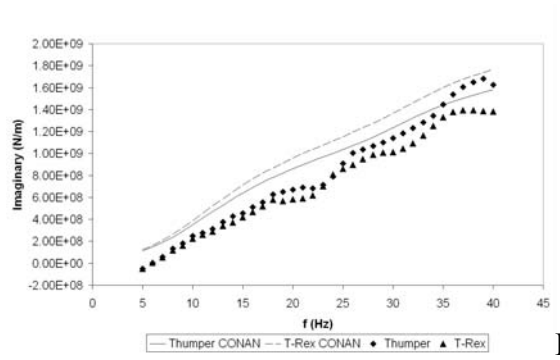


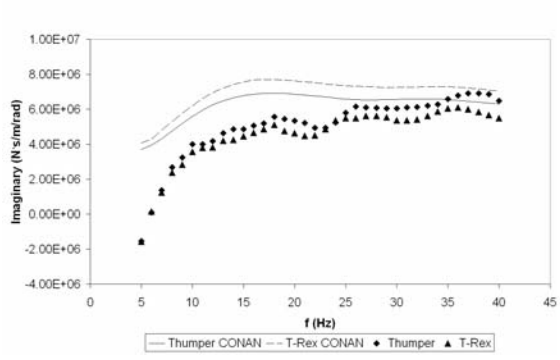
Figure 6-4. Electro-Seis horizontal comparison for the one-degree-of-freedom at 4 ft, independent coupling two-degree-of-freedom at 2 ft and 4 ft, the equal coupling two-degree-of-freedom analyses of Footing 5 at elevations 2 ft and 4 ft. A) Coupling Impedance, Real Component. B) Coupling Impedance, Imaginary Component. C) Coupling Impedance, Real Component Adjusted. D) Coupling Impedance, Imaginary Component Adjusted. E) Coupling Dashpot Coefficient. F) Coupling Dashpot Coefficient Adjusted.



A



B



C

Figure 6-5. Thumper and T-Rex vertical comparison for Footing 6. A) Vertical Impedance, Real Component. B) Vertical Impedance, Imaginary Component. C) Vertical Dashpot Coefficient.

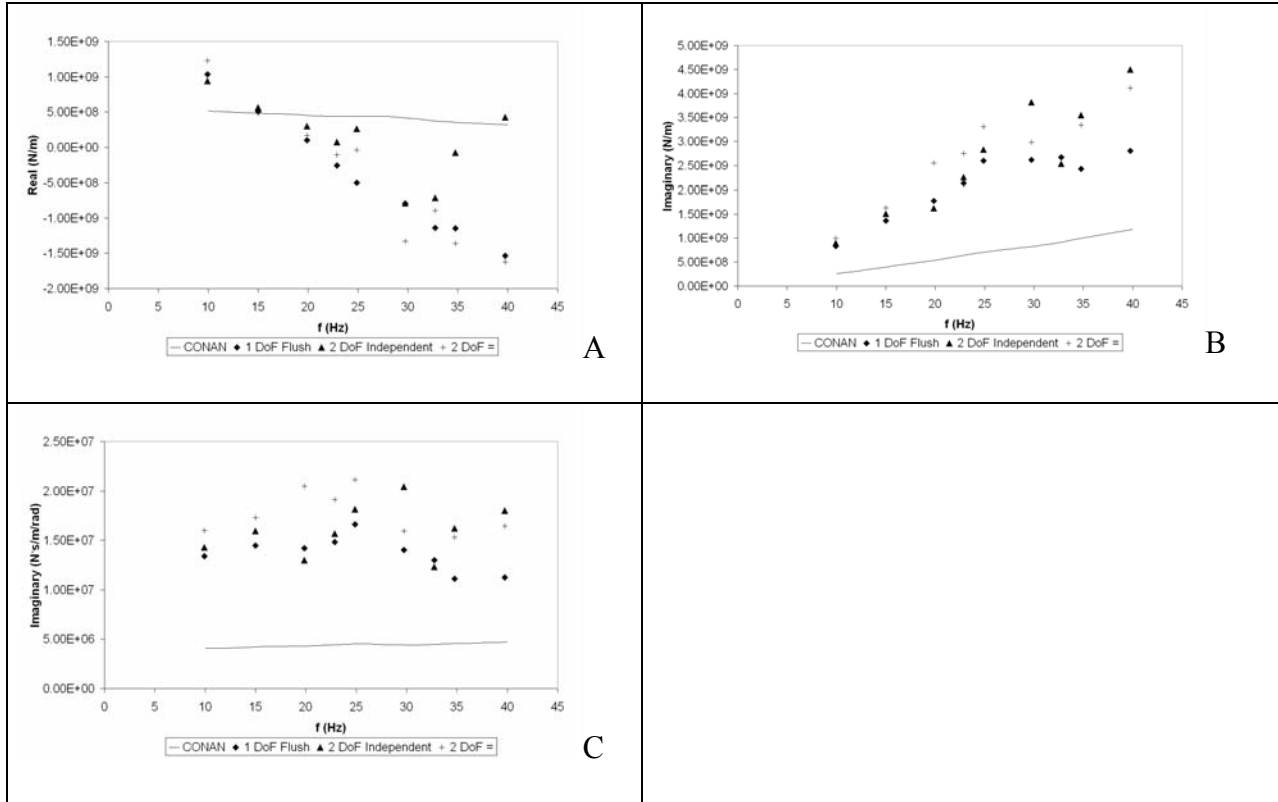


Figure 6-6. ANCO horizontal comparison for the one-degree-of-freedom flush mount, independent coupling two-degree-of-freedom, the equal coupling two-degree-of-freedom analyses of Footing 6. A) Horizontal Impedance, Real Component. B) Horizontal Impedance, Imaginary Component. C) Horizontal Dashpot Coefficient.

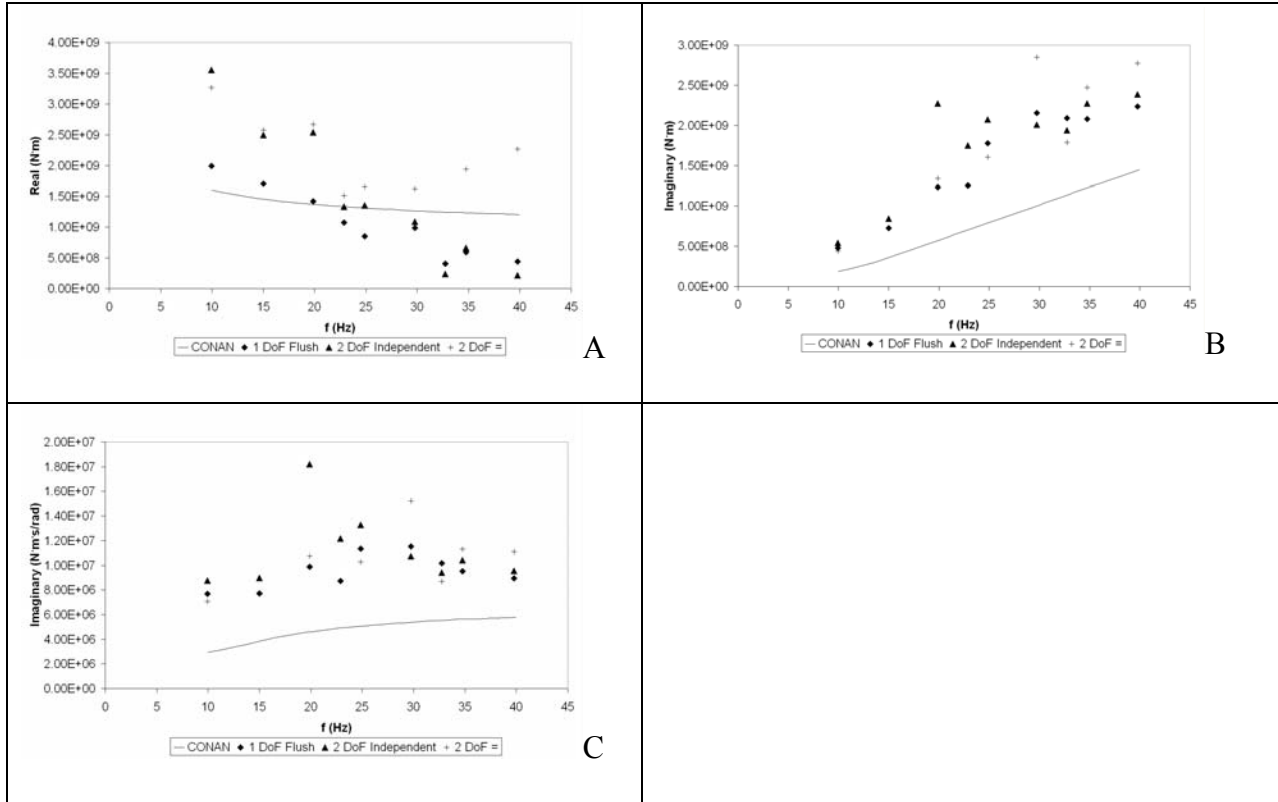


Figure 6-7. ANCO horizontal comparison for the one-degree-of-freedom flush mount, independent coupling two-degree-of-freedom, the equal coupling two-degree-of-freedom analyses of Footing 6. A) Rocking Impedance, Real Component. B) Rocking Impedance, Imaginary Component. C) Rocking Dashpot Coefficient.

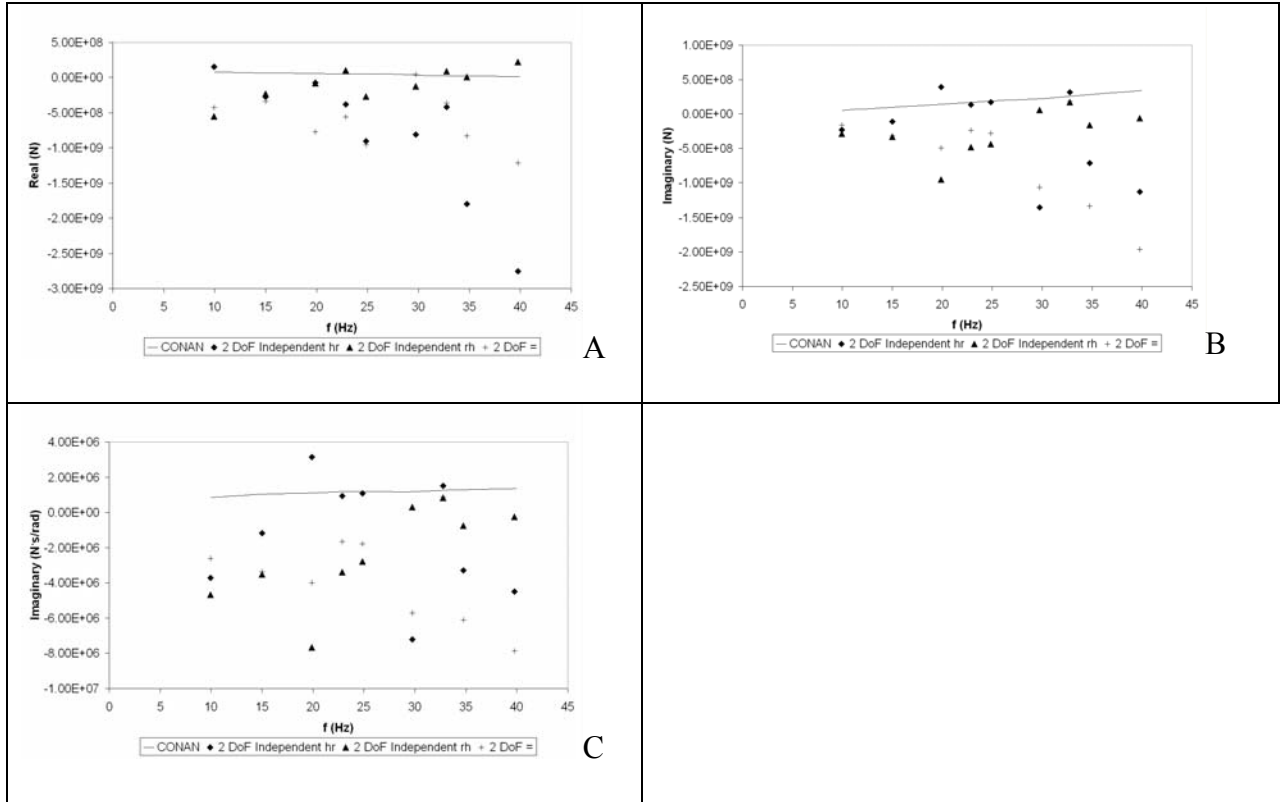


Figure 6-8. ANCO horizontal comparison for the one-degree-of-freedom flush mount, independent coupling two-degree-of-freedom, the equal coupling two-degree-of-freedom analyses of Footing 6. A) Coupling Impedance, Real Component. B) Coupling Impedance, Imaginary Component. C) Coupling Dashpot Coefficient.

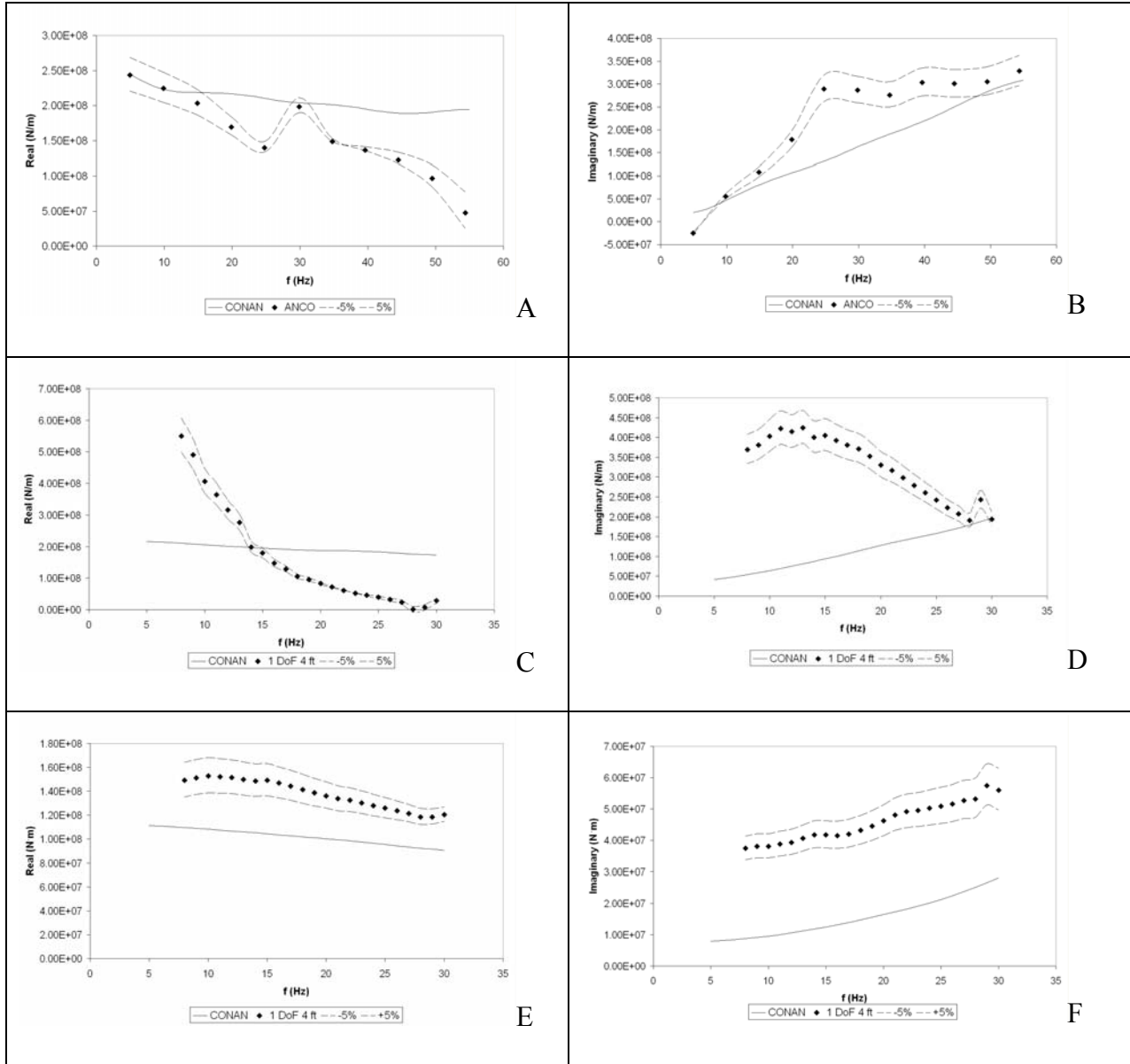


Figure 6-9. Footing 5 Vertical and 1-DoF Error Band. A) Vertical Impedance, Real Component. B) Vertical Impedance, Imaginary Component. C) Horizontal Impedance 1-DoF, Real Component. D) Horizontal Impedance, 1-DoF, Imaginary Component. E) Rocking Impedance, 1-DoF, Real Component. F) Rocking Impedance, 1-DoF, Imaginary Component.

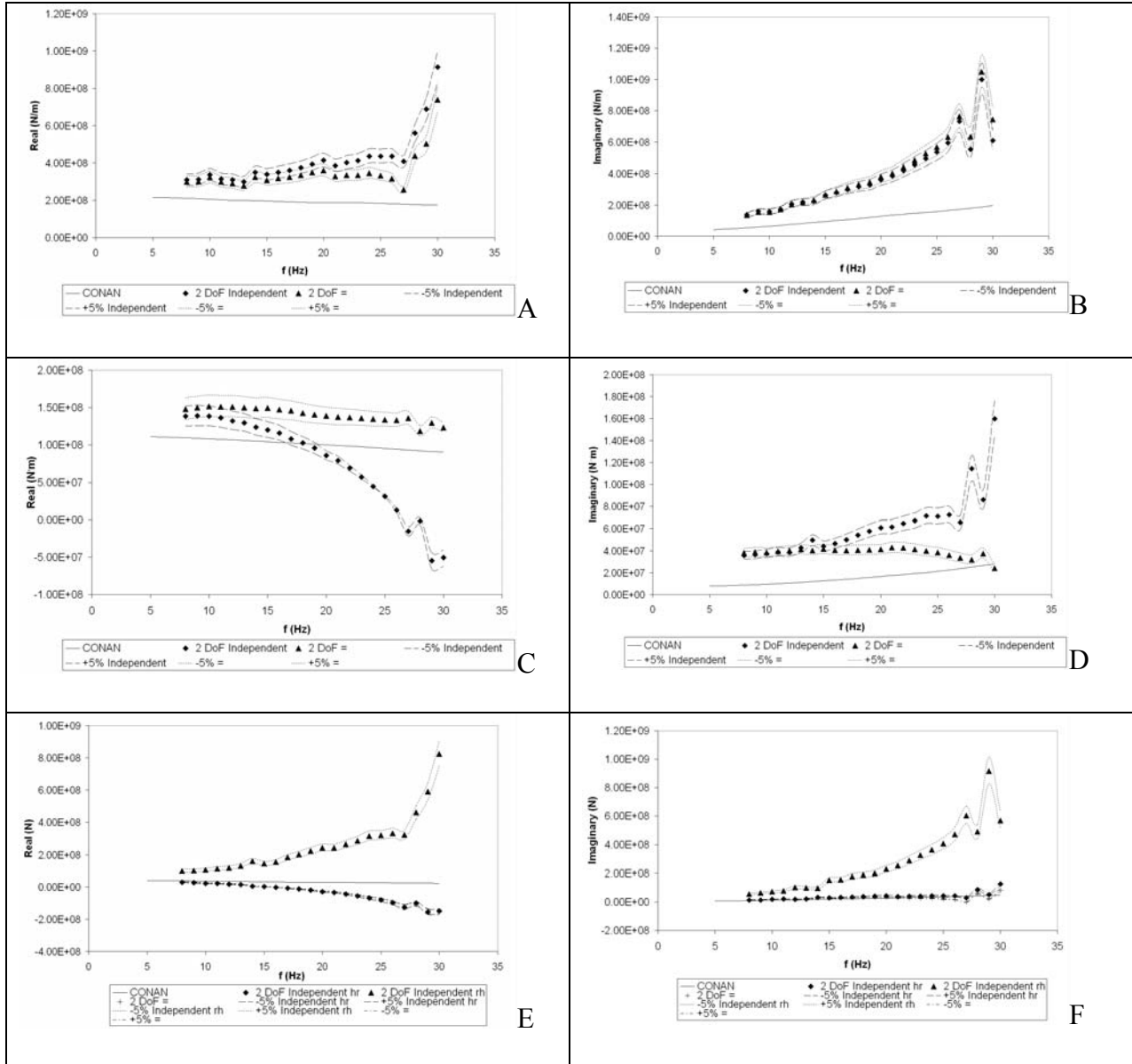


Figure 6-10. Footing 5 2-DoF Error Band. A) Horizontal Impedance, Real Component. B) Horizontal Impedance, Imaginary Component. C) Rocking Impedance, Real Component. D) Rocking Impedance, Imaginary Component. E) Coupled Impedance, Real Component. F) Coupled Impedance, Imaginary Component.

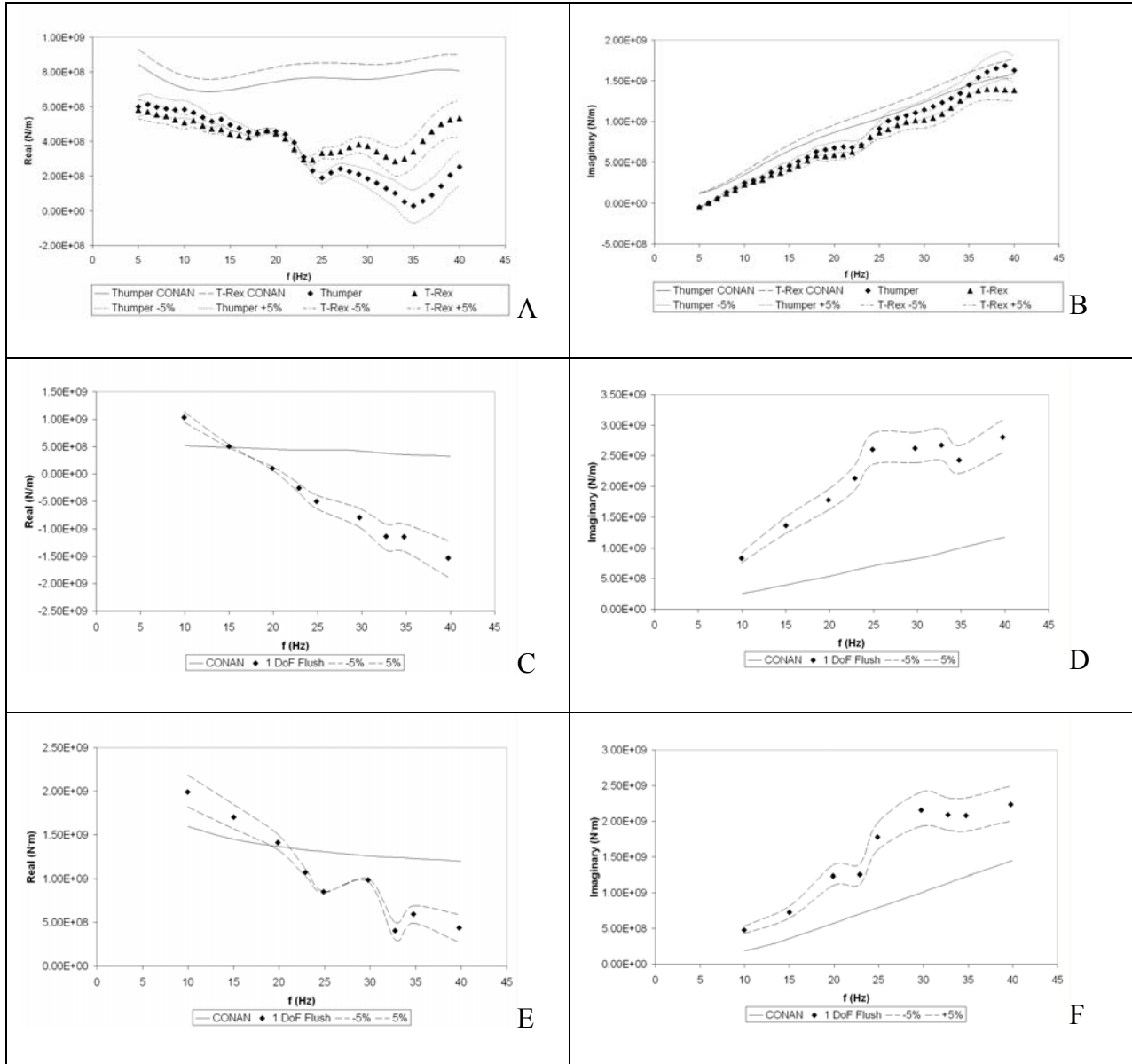


Figure 6-11. Footing 6 Vertical and 1-DoF Error Band. A) Vertical Impedance, Real Component. B) Vertical Impedance, Imaginary Component. C) Horizontal Impedance 1-DoF, Real Component. D) Horizontal Impedance, 1-DoF, Imaginary Component. E) Rocking Impedance, 1-DoF, Real Component. F) Rocking Impedance, 1-DoF, Imaginary Component.

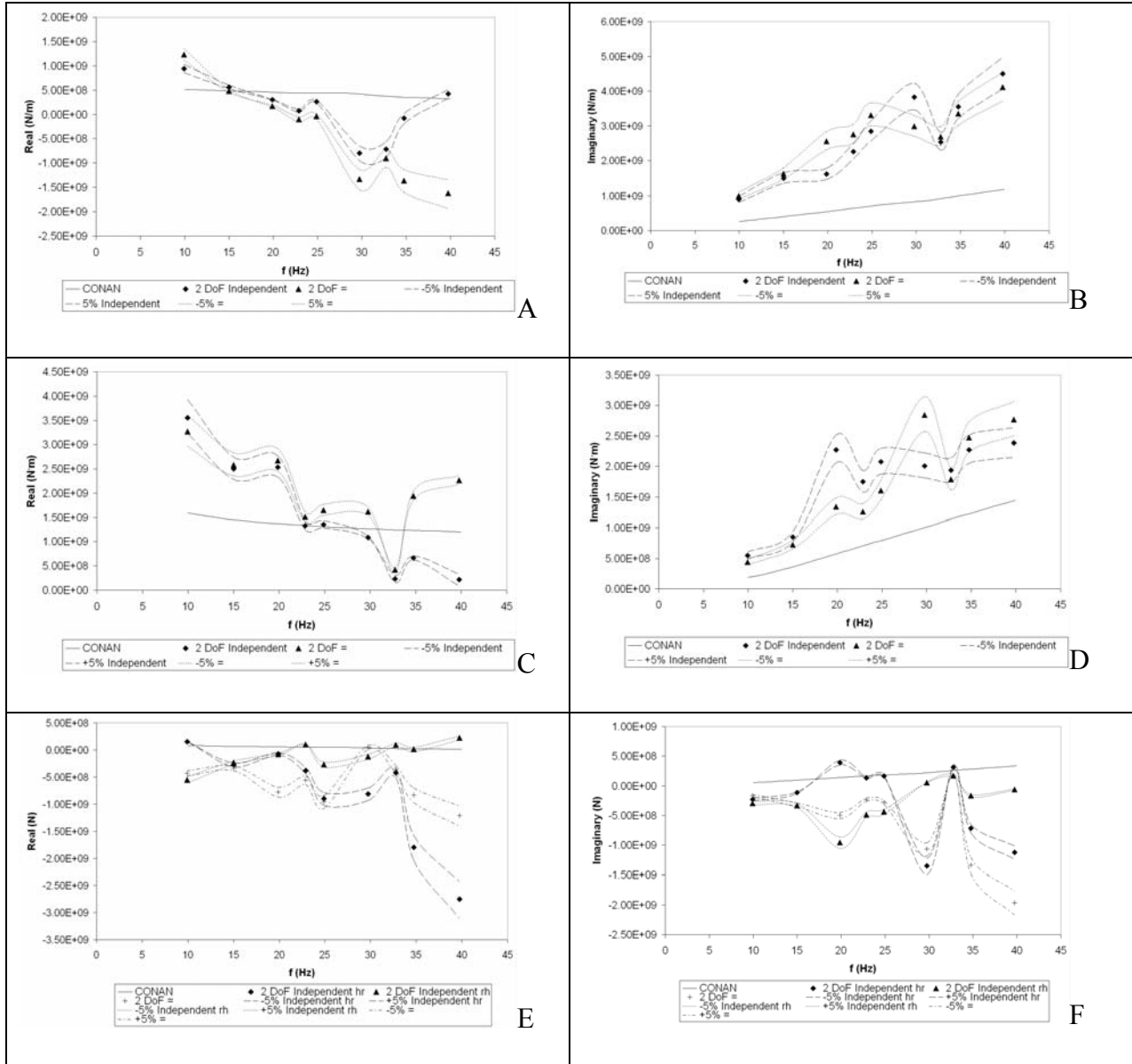


Figure 6-12. Footing 6 2-DoF Error Band. A) Horizontal Impedance, Real Component. B) Horizontal Impedance, Imaginary Component. C) Rocking Impedance, Real Component. D) Rocking Impedance, Imaginary Component. E) Coupled Impedance, Real Component. F) Coupled Impedance, Imaginary Component.

## CHAPTER 7 CLOSURE

### 7.1 Summary of Findings

A comparison between cone models to measured values of impedance functions was conducted to determine the effectiveness of predictions for shallow foundations when applied to conditions found in the field. Two typical concrete foundations were tested. The site was located on the Riverside Campus of Texas A&M and chosen for the extensive geotechnical testing previously conducted and an acceptable foundation already existing. One footing was constructed to meet the requirements of testing. Cone models for multiple modes and each foundation were calculated through CONAN utilizing previous geotechnical investigation data, physical properties of the respective foundation, and geophysical surveys performed for this study. Each foundation was dynamically loaded during vertical and horizontal testing via multiple shakers and various equipment arrangements. Dynamic foundation displacement responses were measured with respect to loading. Displacements were analyzed to calculate measured impedance functions in accordance with available literature. One single-degree-of-freedom and two two-degree-of-freedom approaches produced impedance functions in multiple modes for each foundation. Results for both predicted and measured impedance functions were presented together. The findings are presented here:

- When compared to more rigorous numerical methods and limited field data previously available, cone models seem to be capable of predicting impedance functions accurately. Though data from numerical techniques and measured impedance functions lack some characteristic typically encountered in industry, cone model evaluations demonstrate a positive relationship with each on a promising scale. This relationship was strong enough to initiate field testing.
- Full scale field experiments were designed to measure and record displacements of footings in all modes of interest and under multiple loading arrangements. Load and displacement data was successfully analyzed to produce measured impedance functions via a reverse-calculation program. A reverse-calculation program was developed which executed three techniques that produce three sets of measured impedance functions from

the same data set. With few exceptions, these impedance functions agree fairly well with each other.

- The comparison between cone model predicted and measured impedance functions reveal important similarities and differences. Both agree somewhat with respect to real and imaginary magnitudes. Expected behavior is generally recognized in predicted and measured values, in both footings, and in all modes. Footing 5 exhibits good agreement between predicted and measured values when observing trends with respect to frequency while Footing 6 demonstrates consistency in magnitude between predicted and measured values. When comparing modes, predicted vertical impedance functions appear to compare well to measured values. To a lesser extent horizontal and vertical predictions compare fairly well with some exceptions. Perhaps the most important differences between predicted and measured impedance functions are the consistent under prediction of damping and the increased drop-off of measured real values observed in Footing 6.
- Attempts to uncover possible reasons for differences between predicted and measured impedance functions reduced the likelihood that they were due to error in measurements. An analysis demonstrated that predicted values typically fell well outside a conservative error band around measured impedance functions. An assessment of cone model parameters decreased the possibility that input parameters were responsible for inconsistencies between predicted and measured values. It was demonstrated that a modest change in most input parameters influences impedance function values minimally. Shear modulus seemed to possess the greatest influence over impedance functions but was also well characterized indicating that differences were not a result of inaccurate input data. Cone model prediction assumptions could not be disqualified as a source of difference between predicted and measured values. Potential aspects that may account for inconsistencies of cone models were discussed.

## **7.2 Conclusions**

Reliable techniques appear to have been developed to dynamically excite full scale in situ shallow foundations. Two foundations were tested via multiple shakers, arrangements, and in multiple modes. The responses of the footings seem to have been measured accurately. Multiple reverse-calculation techniques were executed and produced seemingly reliable measured impedance functions.

Predicted impedance functions were produced based on an array of soil tests. Preliminary predictions exhibited a significant level of agreement with the limited measurements previously available. These predictions also demonstrate considerable agreement with more rigorous prediction methods thereby indicating good potential for in situ prediction.

Cone models appear capable of providing an approximation of in situ impedance functions. The accuracy of the prediction seems related to but not limited to the mode of excitation and geometric properties of the footing. The most significant differences between predicted and measured impedance functions are the under prediction of damping and a lack of a considerable drop in stiffness with an increase in frequency. These inconsistencies appear to be the result of inadequacies in cone modeling assumptions.

### **7.3 Recommendations**

After a review of the findings and conclusions, the following recommendations are presented:

- Further identify reasons for inconsistencies. Upon identifying these reasons, select new 2-dimensional or 3-dimensional soil/structure interaction models that better represent in situ conditions.
- Testing to this point is still somewhat limited. There are very few measured impedance function results available. More experimentation at the same site, and then at several sites, would allow additional insight into aspects of shallow foundations that may influence any prediction method of interest.

## LIST OF REFERENCES

- Apsel, R. J. and Luco, J. E. (1987), "Impedance Functions for Foundations Embedded in a Layered Medium: An Integral Equation Approach," *Earthquake Engineering and Structural Dynamics*, Vol. 15, pp. 213-231.
- Briaud, J., Gibbons, R. M., (1994), "Data and Predictions Request for the Spread Footing Prediction Event," *Predicted and Measured Behavior of Five Spread Footings On Sand: Proceedings of a Prediction Symposium, Geotechnical Special Publication No. 41*, June, pp. 11-85.
- Crouse, C. B., Hushmand, B., Luco, J. E., and Wong, H. L. (1990), "Foundation Impedance Functions: Theory versus Experiment," *Journal of Geotechnical Engineering*, Vol. 116, No. 3, March, pp. 432-449.
- De Barros, F. C. P. and Luco, J. E. (1995), "Identification of Foundation Impedance Functions and Soil Properties from Vibration Tests of the Hualien Containment Model," *Soil Dynamics and Earthquake Engineering*, Vol. 14, pp. 229-248.
- Fry, Y. (1963), "*Development and Evaluation of Soil Bearing Capacity Foundations of Structures. Field Vibratory Tests Data*", U.S. Army Waterways Experiment Station, Corp of Engineers, Vicksburg, Mississippi, 18 pp.
- Gazetas, G. (1991), "Foundation Vibrations," Chapter 15 in *Foundation Engineering Handbook*, 2nd ed., Edited by H.-Y. Fang, Van Nostrand Reinhold, New York, pp. 553-593.
- Kausel, E., (1981), "*An Explicit Solution for the Green Functions for Dynamic Loads in Layered Media*", Research Report R81-13, MIT.
- Kausel, E. (1974), "*Forced Vibration of Circular Foundations on Layered Media*", Research Report R74-11, MIT.
- Luco, J. E. (1976), "Vibrations of a Rigid Disc on a Viscoelastic Medium", *Nuclear Engineering and Design*, 36, pp. 325-340.
- Luco, J. E. and Mita, A. (1987), "Response of a Circular Foundation on a Uniform Half-Space to Elastic Waves," *Earthquake Engineering and Structural Dynamics*, Vol. 15, pp. 105-118.
- Luco, J. E., Trifunac, M. D., and Wong, H. L. (1988), "Isolation of Soil-Structure Interaction Effects by Full-Scale Forced Vibration Tests," *Earthquake Engineering and Structural Dynamics*, Vol. 16, pp. 1-21.
- Luco, J. E. and Wong, H. L. (1990), "Forced Vibration of Lotung Containment Model: Theory and Observations," *Journal of Engineering Mechanics*, Vol. 116, No. 4, April, pp. 845-861.

- Lysmer, J., Tabatabaie, R. M., Tajirian, F., Vahndani, S., and Ostadan, F. (1981), "A System for Analysis of Soil-Structure Interaction". Research Report GT81-02, University of California, Berkeley.
- Lysmer, J., Udaka, T., Tsai, C.-F., and Seed, H. B. (1975), "FLUSH-A Computer Program for Approximate 3-D Analysis of Soil-Structure Interaction Problems", Report No. EERC 75-30, University of California, Berkeley.
- Mita, A. and Luco, J. E. (1987), "Dynamic Response of Embedded Foundations: A Hybrid Approach," Computational Methods in Applied Mechanics and Engineering, Vol. 63, pp. 233-259.
- Mita, A. and Luco, J. E. (1989), "Impedance Functions and Input Motions for Embedded Square Foundations," *Journal of Geotechnical Engineering*, Vol. 115, No. 4, April, pp. 491-503.
- Nii, Y. (1987), "Experimental Half-Space Dynamic Stiffness," *Journal of Geotechnical Engineering*, Vol. 113, No. 11, November, pp. 1359-1373.
- Prakash, S. P. and Puri, V. K. (1988), "Foundations for Machines: Analysis and Design", John Wiley & Sons, Inc., New York, 656 pp.
- Richart, F. E., Jr., Hall, J. R., and Woods, R. D. (1970), "Vibration of Soils and Foundations", Prentice-Hall International, Inc., New Jersey, N.J.
- Tassoulas, J. L., (1981), "Elements for Numerical Analysis of Wave Motion in Layered Media". Research Report R81-2, MIT.
- Tran, K. T. and Hiltunen, D. R.J. (2008), "An Appraisal of Surface Wave Methods for Soil Characterization", Submission for 2009 Annual Meeting of Transportation Research Board., Washington, D.C.
- Waas, G.. (1972), "Analysis Method for Footing Vibrations through Layered Media," Ph.D. Thesis, University of California, Berkeley.
- Wolf, J. P. and Deeks, A. J. (2004), "Foundation Vibration Analysis: A Strength-of-Materials Approach, Elsevier", 218 pp.
- Wong, H. L. and Luco, J. E. (1976), "Dynamic Response of Rigid Foundations of Arbitrary Shape", Earthquake Engineering and Structural Dynamics, Vol. 4, pp. 579-587.
- Wong, H. L., Trifunac, M. D., and Luco, J. E. (1988), "A Comparison of Soil-Structure Interaction Calculations with Results of Full-Scale Forced Vibration Tests", *Soil Dynamics and Earthquake Engineering*, Vol. 7, No. 1, pp. 22-31.
- Wong, H. L. and Luco, J. E. (1978), "Tables of Impedance Functions and Input Motions for Rectangular Foundations", Report CE-78-15, Department of Civil Engineering, University of Southern California, Los Angeles, December, 92 pp.

Wong, H. L. and Luco, J. E. (1985), "Tables of Impedance Functions for Square Foundations on Layered Media", *Soil Dynamics and Earthquake Engineering*, Vol. 4, No. 2, pp. 64-81.

## BIOGRAPHICAL SKETCH

Patrick William Dunn was born in State College Pennsylvania and raised in Ledyard Connecticut. After high school he attended the University of Connecticut and supplemented his education in geotechnical engineering by working for CTL Thompson in Denver Colorado during his last two summers. After receiving his Bachelor of Science he worked for Great Lakes Dredge and Dock Company until August of 2002 when he began his studies at the Pennsylvania State University. He received his Master of Science in December of 2005 in civil engineering and accepted a fellowship at the University of Florida to study civil engineering.